Research on Intelligent Suppression for Torsional Vibration of Electric Vehicle Drivetrain

by Shengxiong Sun

Thesis submitted in fulfilment of the requirements for the degree of

Doctor of Philosophy

under the supervision of Prof. Nong Zhang

University of Technology Sydney
Faculty of Engineering and Information Technology

January 2020

CERTIFICATE OF ORIGINAL AUTHORSHIP

I certify that the work in this thesis has not previously been submitted for a degree nor has it been submitted as part of requirements for a degree except as fully acknowledged within the text.

I also certify that the thesis has been written by me. Any help that I have received in my research work and the preparation of the thesis itself has been acknowledged. In addition, I certify that all information sources and literature used are indicated in the thesis.

Production Note:
Signature of Student: Signature removed prior to publication.

*Date:*December 2019

ACKNOWLEDGEMENTS

TABLE OF CONTENTS

LIST OF FIGURES

LIST OF TABLES

GLOSSARY OF TERMS

ABBREVIATIONS USED IN THESIS

Chapter 1

AMT- Automated Manual Transmission

ASTW-Adaptive Super Twisting

AT- Automatic Transmission

CVT-Continuously Variable Transmission

DCT-Discrete Cosine Transform

EKF- Extended Kalman Filter

GA-Genetic Algorithm

HIL- Hardware in Loop

KF- Kalman Filter

LQG- Linear Quadratic Gaussian

LQR- Linear Quadratic Regulator

MIMO- Multi-input Multi-output

MPC- Model predictive control

NVH- Noise, vibration, and harshness

PD-Proportional Derivative

PID- Proportional-Integral-Derivative

PMSM- Permanent Magnet Synchronous Motor

QGA- Quantum Genetic Algorithm

RCP- Rapid Control Prototype

RLS- Recursive Least Squares

RMS- Root Mean Square

SISO- Single-Input-Single-Output

SM-Sliding Mode

SMC-Sliding Mode Control

SMO-Sliding Mode Observer

STW-Super Twisting Sliding Mode Observer

SVPWM- Space Vector Pulse Width Modulation

UKF- Unscented Kalman Filter

UT- Unscented Transformation

Chapter 3

PF- Particle Filter

SIS- Sequential Importance Sampling

Chapter 4

AASTW- Accelerated Adaptive Super-Twisting Sliding Mode Observer

AcSTW-Accelerated Super-Twisting Sliding Mode Observer

AdSTW-Adaptive Super-Twisting Sliding Mode Observer

CAN- Controller Area Network

MCU- Motor Control Unit

VCU- Vehicle Control Unit

Chapter 5

QGA- Quantum Genetic Algorithm

ABSTRACT

Compared with the conventional fuel-consumption vehicle, electric vehicle does much better in controllability, regarding more accurate controlling of torque or rotation speed and more rapid response. The characteristic of rapid torque response will bring step motor torque output approximately when the drive tip in/out, because there exist torsional elastic damping parts such as tires and drive shaft in the drivetrain, moreover, there exists no flywheel to save the energy and buffer jerking, and then longitudinal vibration of vehicle that more sensitive to human will be introduced. In this thesis, by taking advantage of the excellent controllability of electric vehicle, active damping control of torsional vibration in vehicle drivetrain is researched, motor torque control in active damping for drivetrain torsional vibration is realized based on parameters intelligent estimation and motion state observation for the drivetrain. Improvement of electric vehicle drivability is realized focusing on driver's tipping in/out and unloading motor torque before shifting. The main content of the thesis is as follows.

Based on the drivetrain of electric drive logistics vehicle with two speeds automated manual transmission, multibody dynamic model of electric drivetrain is established, by Fourier transforming the multi-body dynamic model, frequency response function matrix of the system is obtained and frequency response analysis of the electric driving system can be carried on, and then natural frequencies, mode shapes and resonance characteristics of the drivetrain system can be revealed.

In order to solve this problem nonlinear particle filter-based intelligent parameter estimation method is proposed in this thesis. As a critical parameter in dynamic control of powertrain, vehicle mass varies continuously in a wide range and large magnitude during operation, it is one of the most significant variables in control law constituting, but vehicle mass is difficult to be measured automatically in real-time. The particle filter is recursive filter based on Monte Carlo algorithm, using the processes of importance sampling and resampling and according to motor torque output and motion states of drivetrain, parameter estimation of vehicle mass can be realized. Besides, this vehicle

mass intelligent estimation method is robust and statistical characteristics of disturbances and uncertainties in the powertrain system is unnecessary to be known.

In this thesis accelerated adaptive second order super-twisting sliding mode observer (SMO) is proposed, it can remarkably attenuate "chattering", the inherent drawback of sliding mode (SM) variable structure algorithm, and estimation error convergence is accelerated to a large extent by introducing of the "system damping". Motion states are also necessary in the control law designing for the drivetrain system, aiming to get the state variables of the drivetrain that are not measured directly, Based on the proposed novel sliding mode observer, torque accumulated in the drive shaft is observed to provide information for selection of appropriate shifting time, so that torsional vibration and jerking in drivetrain caused by sudden releasing of torque accumulated in the drive shaft after shifting is avoided, meanwhile, it also provides state information for the active control algorithm in the following content.

Based on the parameter estimation and state observation of the drivetrain, quantum genetics optimization and Linear Quadratic Gaussian joint algorithm is proposed to design the optimal control law to actively damp torsional vibration in drivetrain. According to the multi-feedbacks of the current motion states of drivetrain, optimal motor torque output command is calculated to compensate motion oscillations of drivetrain. The quantum genetic optimization unit utilizes qubits to replace binary encoding and quantum transformation is realized from quantum rotating gates so that the parameter in Linear Quadratic Gaussian to be optimized is searched faster to minimize the fitness function. By optimization of the parameter in Linear Quadratic Gaussian controller, more authentic and objective optimization of the controller performance is realized than the controller with subjective parameter selection from designer. Meanwhile, it will not increase the complexity and computational power consumption of the control law.

Rapid prototyping experiment, test rig experiment and real vehicle experiment are carried on focusing on parameter estimation, state observation and torsional vibration damping control to test the performances of the proposed algorithms in this thesis.

CHAPTER 1: INTRODUCTION

1.1 Overview of the Project

Permanent magnet synchronous motor (PMSM) has many advantages, such as smaller size, lighter weight, higher efficiency, and can provide large torque at low speed. Many automobile manufacturers all over the world select PMSM to drive Electric Vehicles (EV). Using motor instead of traditional internal combustion engine brings better control performance regarding shorter response time and more accurate target tracking in torque or speed command. Although domestic and international researchers have carried out extensive researches on motor active control method to improve the power performance of the electric driving system, research on commercial electric vehicles equipped with Automated Manual Transmission (AMT) is not enough. Because of the requirements of Chinese domestic condition, research on this type of vehicle is mainly completed by domestic researchers. There is still much space of improvement in terms of software, structure and configuration designing.
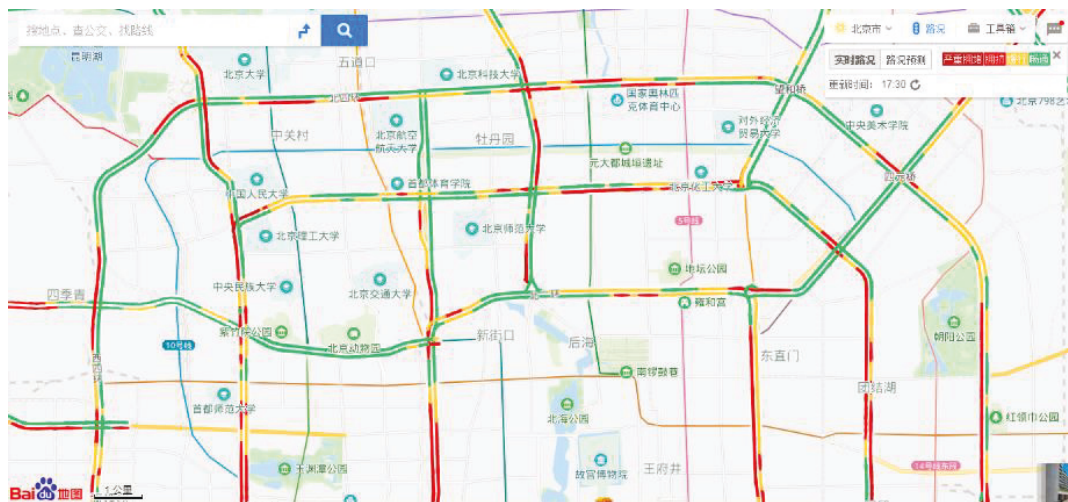
Figure 1.1 Condition of Part of Beijing Traffic at A Certain Time

(a) As for the part of system configuration, the structure of centralized drive electric drive system is still direct rigid connection between motor and transmission. For urban operation conditions, there are usually hundreds of meters of traffic jams caused by signal lights or large traffic flow as shown in Figure 1.1. Because of quick response

of the PMSM and there is no flywheel or clutch to buffer and saving energy, on the other hand, low-frequency excitation from periodic rotary low running speed of the motor may probably get close to resonance frequency of the drivetrain, such resonance is inherent and inevitable, so it is necessary to equip a damper to attenuate the torsional vibration as a passive method.

(b) As for the control algorithm, in the references about control algorithms of electric vehicle powertrains all over the world, most of them need to know information on load or other parameters in the powertrains, which is the base of state observation and top-level control algorithms. However, most researchers usually choose fixed parameters to participate in the calculation. These parameters may be measured or derived from experience, which will affect the accuracy of state observation and control execution.

Taking the vehicle mass as an example, the vehicle mass is almost the largest physical parameter in magnitude in the drivetrain system, and also one of the most important and indispensable parameters for calculating the load of the drivetrain system, designing energy management strategy and optimizing the shifting scheme. Vehicle mass is usually used to calculate the load or resistance of the drivetrain system (resistance change caused by the change of slope and rolling resistance in urban operation can usually be equivalent to increasing or decreasing of the mass on the horizontal road surface), therefore, it is unreasonable to set the vehicle mass constant and it is significant to estimate the vehicle mass on-line in real time [1,2]. At present, Kalman Filter (KF) method and Recursive Least Squares (RLS) method are still the main methods to estimate vehicle quality. However, Kalman filtering algorithm needs to know the statistical characteristics of noise, and recursive least square is sensitive to outliers, and calculation is unstable. Therefore, it is necessary to find better parameter estimation methods to avoid these defections.

At present, there are many studies in the literature about controlling the torque unloading of motor dynamically instead of detaching the clutch to interrupt power

input to the transmission for shifting. The purpose of this operation is to reduce the transmitted torque between the meshed gears to zero so that the engaged synchronizer sleeve can be successfully removed from the current gear. However, during vehicle drivetrain system working, due to the co-operation of the positive torque from motor and the reverse resistance torque from the load, elastic potential energy will be accumulated in the elastic components of the drivetrain system. Therefore, the torque transmitted between the gears in the transmission may not be zero actually after power unloading from the motor, and it will suddenly be released, and bring additional torsional vibration or impact to the drivetrain system [3]. Therefore, it is necessary to introduce a nonlinear state observer to solve this problem.

The state observer is required to occupy less computational resources, simple computing formula, more accurate target tracking performance and fast response. In order to solve such problems better, it is necessary to optimize the widely used observation theory to take advantages and avoid disadvantages according to the requirements of EV powertrain, not only to realize the electric vehicle. The estimation of the drive shaft torque also needs to improve the control performance of the driving motor. Although it is difficult to eliminate the observation error in the initial stage with less computational effort, the convergence of the accelerated observer error will also play a positive role in the improvement of the problem.

Besides, as for the upper-layer active control of EV drivability, the parameters of the controller are still selected subjectively or experimentally by designer, and the obtained optimal control law is not necessarily "optimal" actually, so it is better to introduce optimizing process in parameters selection or introduce objective parameter selection method to improve the algorithm performance.

This research relies on the project "study on optimization of powertrain system of full electric logistics vehicle" co-operated by Beijing Electric Vehicle Co., LTD and Beijing collaborative innovation center for electric vehicles and is supported financially by National Natural Science Foundation of China "Research on Novel Configuration and

Multidimensional Optimal Control Theory for Distributed Electrical Vehicle" (grant number: 51575044) and National Key R&D Program of China "Key Technologies and Applications of High-Performance Electric Bus Powertrains" (grant number: 2017YFB0103801). The main content of this thesis is proposing a novel active damping control algorithm with intelligent optimization unit for torsional oscillations in electric vehicle drivetrain based on model of motor-transmission with 2 speeds integrated electric logistics vehicle. During the process of execution, nonlinear parameter estimation based on particle filter and observation error accelerated-convergent adaptive second order super twisting sliding mode observer are proposed, so that the necessary information for drivetrain torsional oscillation active damping is provided.

1.2 Research Objectives and Contributions to Knowledge

The specific objectives and contributions are given as follows:

(1) An intelligent parameter estimation method for vehicle mass based on non-linear Particle Filter (PF) is proposed. The most remarkable advantage of this algorithm is that it is not necessary to know the statistical characteristics of measurement noise or uncertainties from the powertrain system, and also compatible to non-linear model with complex and stochastic working conditions.

(2) An error-accelerate-convergent adaptive second-order super twisting sliding mode observer algorithm is proposed, and the mathematical proof for convergence and stability is given. This algorithm can effectively reduce "chattering", the inherent problem of sliding mode variable structure algorithm, and can remarkably increase the convergence speed of observation errors, so that the observer has better tracking performance and accuracy.

(3) Based on the proposed observer above, torque observer for the drive shaft is designed, which avoids torsional vibration or impact to the drivetrain caused by the sudden release of excessive elastic potential energy accumulated in the drive shaft when shifting. Moreover, it also provides state information of drivetrain for the torsional

vibration active controller.

(4) A joint optimal control algorithm based on linear quadratic gauss and quantum genetic optimization is proposed for torsional vibration of EV drivetrain. By introducing quantum computation into the optimization process, the speed of parameter optimization is much improved. The linear-quadratic Gauss controller uses the multi-feedback information of the drivetrain motion state to calculate the optimal torque control law for the motor, which actively damps torsional oscillations in the drivetrain during motor unloading and driver's tipping in/out.

1.3 Presentation and Structure of the Thesis

The main content in the thesis are listed as follows:

Chapter 1:   Background and main contributions of the thesis are introduced.

Chapter 2:   Based on the motor-transmission of 2 speeds integrated electric logistics vehicle powertrain, mathematical model for algorithms research is established, and torsional vibration response characteristics of this model are analyzed, so that necessity of equipping torsional damper is discussed further. This drivetrain model provides the basis for parameter estimation, state observation and active damping control algorithm in the later chapters.

Chapter 3:   Based on the discrete vehicle longitudinal dynamic equation after forward Euler approximation, nonlinear particle filter is introduced to estimate the vehicle mass intelligently, and it gains a competitive advantage that statistical characteristics of noise and uncertainties in the system are not necessary to be known or supposed in advance.

Chapter 4:   According to the motion state of the powertrain, algorithm using multiple feedback from motion state of drivetrain to active damp torsional oscillation in EV drivetrain is proposed. By introducing the Quantum Genetic Algorithm (QGA) to simulate the rule of survival of the fittest in biological evolution to search for the optimal parameters in the active damping controller, searching speed is much improved because

quantum characteristics of the superposition, entanglement and interference can enable a chromosome to express the superposition of multiple states and evolve parallelly using quantum logic gate.

Chapter 5:　Experiments are carried out to test the proposed theories. For the vehicle mass parameter estimation based on nonlinear particle filter is tested by real vehicle (bus), for the torque in drive shaft observation based on novel sliding mode observer is tested on a test rig with real vehicle, for the active damping control of torsional oscillation in drivetrain with quantum optimization is tested by Rapid Control Prototype built on Micro AutoBox and dSPACE Simulator.
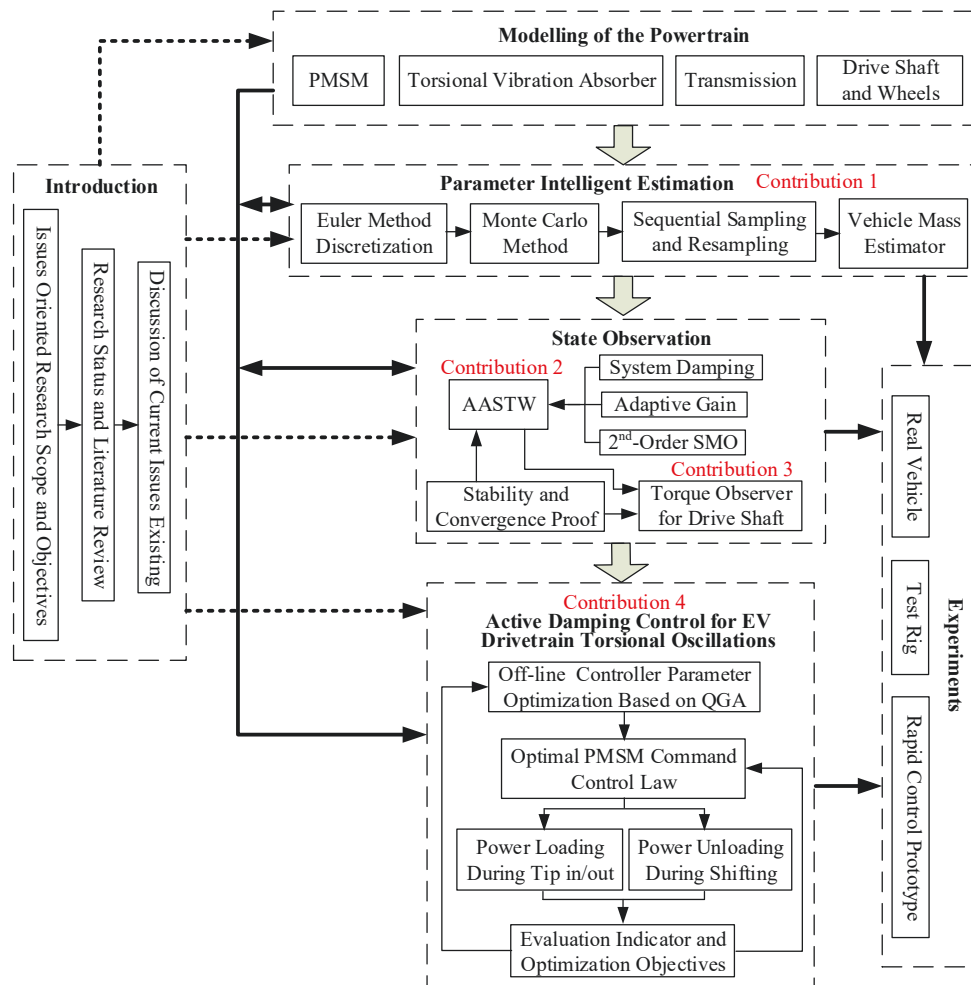
Figure 1.2 Organization of the Thesis

Relevance and structure of all parts of the thesis are organized as in Figure 1.2.

1.4 Background and Literature Review

1.4.1 Background of Research

Climate changing has already been a worldwide problem for a long time and it attracts attention widely. Governments have realized the transition from traditional consumption and fossil-fuels-dependent to the green and sustainable renewable energy is one of the effective ways to alleviate the problem. This kind of energy transformation is particularly necessary for transportation industry. Due to air pollution, government control, social concerns and rapid development of technology, non-liquid fuels including electric energy and natural gas will become increasingly important in the next decade. Moreover, air pollution, traffic jams and noise pollution caused by gasoline or diesel-powered private cars have been plagued for many years. According to the agreement made at the United Nations Climate Conference (COP21) in Paris in 2015, many countries have announced the goal of phasing out internal combustion engines. The European Commission has established new carbon dioxide emission standards in November 2017 as the industry standard for clean automotive [4]. During the past decade, development and promotion of various types of electric vehicles grew up rapidly and are witnessed widely. A report from CNN revealed that many companies including India, France, Britain and Norway are trying to replace gasoline and diesel cars with cleaner productions. In Germany, Angela Dorothy Merkel also hinted that in the near future, more modern cars will be introduced throughout the country. In addition, at least eight other countries have also set a sales target for electric vehicles: the UK announced that they will ban the sale of gasoline and diesel vehicles in 2040 to improve the country's air quality and achieve zero emissions on the road by 2050; the French government also announced that they will end the sale of gasoline and diesel vehicles by 2040 to combat global warming, when automotive producers will only be allowed to sell electric or other clean energy-driven vehicles, including hybrid-drive vehicles; the Indian government announced that by 2030, all the automotive sold in the country will be electrically driven, and act as an example among the world's polluted countries by policy formulation; and the Norwegian

government's transportation plan aims to achieve a zero-emission for all passenger vehicles by 2025 [5]. Relevant news from the South China Morning Post [6] reported that 174 of the 1022 models exhibited at the 2008 Beijing International Automobile Exhibition are new energy vehicles, of which 124 are produced by Chinese companies. Last year, there were 777,000 electric vehicles sold in China with increase of 53% over 2016, as shown in Table 1.1 obviously that China is the world's largest market with no doubt. Since most of the electric vehicles sold in China are produced by domestic manufacturers, cost of manufacturing, transportation and sales can be reduced, together with the advantageous regulation and subsidy policies from government will make electric vehicles more competitive.

Table 1.1 New Energy Vehicle Sales

	China	the US	Global
2015	331100	116000	540000
2016	507000	160000	773600
2017	777000	199000	1223600
2018 (early)	1000000	400000	1800000
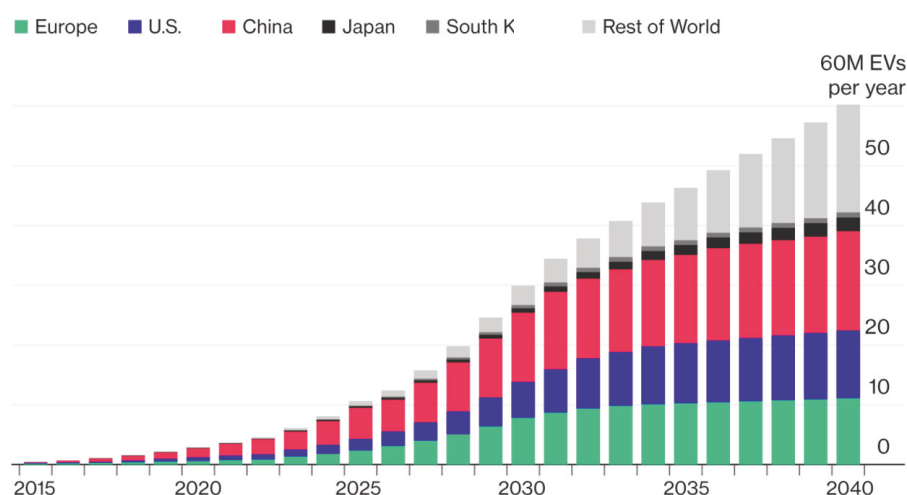
Figure 1.3 Electric Vehicle Sales Forecast in Major Countries of the World

China is also the country with the largest popularity of electric vehicles in the world, and is expected to account for half of the world's EV sales in the next seven years. In 2017,

six cities in China achieved one-fifth of the sales of electric vehicles due to the strict policy of purchasing and fuel vehicles limitation. It is estimated that by 2025, the sales of electric vehicles worldwide will increase tenfold to 11 million. According to Bloomberg's 2018 Electric Vehicle Outlook Report, electric vehicles in China will reach 19% of passenger vehicle sales, 14% in Europe and 11% in the US. It is obvious to observe from Figure 1.3 that China is leading a green transportation revolution represented by the development of EV in the world [7,8].

The conversion to electric driving system is one of the core contents of EV research and development. The transition from fuel-electric hybrid driven type in medium term to fully electric driven or fuel cell type in a long run is a widely recognized route [9]. At present, electric vehicles sold on market is using motor-single speed transmission or direct driving system as the mainstream powertrain configuration. In fact, this configuration does overcome many defects of the transmission with conventional internal combustion engine, such as no torque output at 0 rpm and narrow speed tuning range, especially during high power output. However, the direct driving or single speed scheme does not make the overall performance and economy of the vehicle outstanding. This configuration also imposes very high requirements on the torque output characteristics and power density of the motor, it not only greatly increases the producing cost but also increase weight and volume of the motor; moreover, vehicle dynamic performances such as axle load distribution are influenced a lot due to the large motor.

Figure 1.4 Typical Centralized Driven Electric Vehicle Powertrain Layout

Single motor direct driving, motor-transmission integrated configuration and dual motor coupling powertrain are typical forms of centralized drive schemes [10]. As can be seen

from Figure 1.4, the centralized driven electric vehicle is closer to the traditional internal combustion engine vehicle transmission system and has more advantages: the bulky and heavy internal combustion engine is replaced by a smaller and more controllable motor; the conventional flywheel and clutch are also eliminated because the PMSM does not have the defects of torque output ripple and no torque output when starting. Centralized driving system performs advantages of simple structure, large space saving, low cost, and good technology portability, which are beneficial to rapid growth of the electric vehicle industry. Since PMSM can provide enough traction torque at start-up and can provide a wide range of speed tuning while supplying sufficient torque, such that single speed driving scheme can make electric vehicles perform well in most conditions. However, one of the main problems is that this kind of configuration can hardly make the EV work in high efficiency area of PMSM efficiency map as shown in Figure 1.5. Therefore, application of single speed transmission scheme will reduce efficiency of PMSM, the increased energy consumption will influence the cruising mileage which people care the most about.
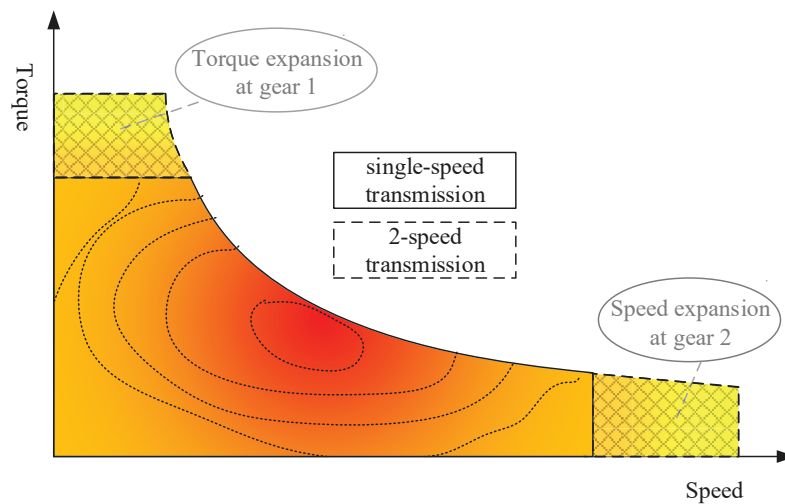
Figure 1.5 Sketch of PMSM Efficiency

It is well known that most electric vehicle is equipped with single speed transmission currently which put forward more restrict requirements of driving motor performance [11]. Although domain manufacture of PMSM has improved a lot but still far from enough [12]. Therefore, this powertrain configuration of EV with fixed speed transmission is not

suitable for EV manufacture in China or other countries at this stage.

The powertrain is one of the key systems of electric vehicle and determines the dynamic performance. The fixed gear transmission scheme can meet the requirements under the condition that dynamics and economics are not required too much. But when they are required further, the fixed gear transmission scheme has to impose higher requirements of PMSM power and battery capacity, which not only increase the cost but also influence the battery life [13]. In order to improve EV dynamics and economics without introducing a higher-power motor, and to improve the adaptability of electric vehicles to loads or road conditions, installing a multi-speed transmission is a common method [14-17]. Therefore, the two-speed transmission driving scheme guarantees both power and economy advantages: (1) as can be seen in Figure 1.5, during the initial EV start-up and accelerating for overtaking, the peak value of the output torque of the PMSM has been expanded at the first gear, so smaller and lower power motor is required capered with driving scheme of fixed gear ratio or direct driving powertrain; (2) similarly, the maximum speed of the electric vehicle is also improved by the extension of maximum motor speed at the second gear; (3) optimal shifting scheme can be designed according to operation conditions so that the driving motor can work in high efficiency area of the map and economics and cruising mileage [18,19].

Figure 1.6 Electric Logistics Vehicle Prototype with Integrated Powertrain

As the national development strategy of new energy vehicles gets much clearer, the electric vehicle industry develops rapidly and the electric vehicle has entered the promotion age from trail period. In June 2015, a full electric logistics vehicle shown in

Figure 1.6 is developed in the cooperation project of Collaborative Innovation Center for Electric Vehicles, Beijing Institute of Technology and Beijing Electric Vehicle Co., LTD. This electric logistics vehicle is equipped with a PMSM-two-speed transmission integrated driving system without a clutch. Interrupting and recovering power to the transmission for shifting is realized by motor control.

Several typical automatic transmission systems as in Table 1.2 have their own characteristics: compared with the automatic transmission (AT), continuously variable transmission (CVT), dual clutch automatic transmission (DCT), etc., technique of the automated manual transmission is mature with the advantages of low cost, high efficiency, small size, easy installation etc. and is the most suitable for configuring requirements of urban logistics vehicles. Excessive gears will not only increase the complexity of the transmission manufacturing and control, but also increase transmission volume and mass, and the extra gear selection will also prolong power interruption duration of shifting and destroy the vehicle dynamics.

Table 1.2 Performance Comparisons of Typical Automatic Transmissions

Transmissions	Pros	Cons	Applications
AT	smooth and adaptable	high energy consumption and complex structure	car
AMT	Low energy consumption, simple structure and low cost	poor drivability, power interruption	general urban traffic
CVT	high efficiency and good drivability	poor bearing capacity, high cost and poor reliability	small car
DCT	fast shifting and low energy consumption	high cost and complicated structure	hybrid vehicle

The object of research in this thesis is based on the electric logistics vehicle of joint development with Beijing EV, of which powertrain comprises PMSM-2-speed transmission integrated system, final drive, drive shaft, wheels, etc. Since the motor responds very quickly to the driver's pedaling command and is not equipped with fly

wheel for energy storage or buffering like conventional engine, torque step input to the transmission is formed when the driver suddenly releases the pedal command or the PMSM unloads the torque before the transmission shifts. Due to the existence of elastic damping parts such as drive shafts and tires in the driveline, it constitutes a typical damped harmonic oscillator which will produce torsional vibration when torque step input happens, and it will further produce vehicle longitudinal vibrations that more sensitive to human body.

This thesis aims to research for improving the drivability of electric vehicle equipped with two-speed AMT by applying motor active damping control. Based on mathematical modeling of the vehicle powertrain, the proposed intelligent estimation, observer and control algorithms are applied to improve EV drivability.

1.4.2 Literature and Information Review

1.4.2.1 Research on Smooth Driving Technique of Electric Vehicle

In the 1930s, automobile manufacturers began to attempt to de-clutch, such as replacing traditional clutches with hydraulic coupling or centrifugal clutch and shift frequency during start/stop and acceleration was also reduced, and such de-clutch driving configuration was also applied to more complex systems. With development of technology and automatic control, such semi-automatic transmission has also been phased out so that more complex shifting requirements are met. However, for the small and low-power cars this semi-automatic transmission with a dry clutch are still retained because mechanical connection provides higher transmission efficiency than hydraulic coupling. Other early semi-automatic transmissions are mainly used in diesel locomotives and some road vehicles [20,21].

Modern AMT transmissions have achieved all automatic shifting functions. Drivers do not need to operate clutches and shifting forks. Series of actions such as throttle control, clutch manipulating, gear selection and shifting are executed by corresponding actuators under control, the controller can output the optimal economic or dynamic command

according to PMSM efficiency characteristics. In 2015, Eaton Corporation developed a control method for operating an automated manual transmission system for driving system consisting of an engine, a multi-speed automated manual transmission and a clutch between them. The control method depends on the throttle changing rate, when the throttle opening rate is larger than a certain threshold, the clutch is engaged at the first rate; when the throttle opening rate is less than a certain threshold, the clutch is engaged at a second engagement rate which is proportional to the throttle opening [22].

In 2010 ZF Friedrichshafen AG patented a vehicle transmission control method which serves powertrain comprising an internal combustion engine with a drive shaft, a driving motor connected to the drive shaft, a multi-speed AMT, and a friction clutch between engine driveshaft and transmission input shaft. When shifting command comes the minimum or temporary closing friction coupling can be achieved by combining with engine control. In order to speed up the shifting operation and reduce torque peak during shifting, the motor is temporarily used as a generator or compensation motor [23].
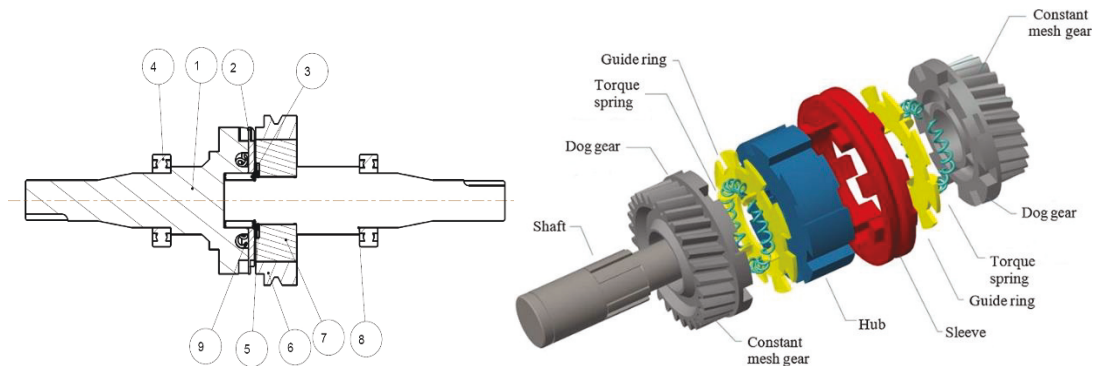
Figure 1.7 Novel Synchronizer "Harpoon-Shift"

In order to overcome the inherent defects of AMT transmission and improve the shift quality, W. Mo and P. Walker et al. of University of Technology Sydney, Australia proposed a novel synchronizer configuration called "Harpoon-Shift" as shown in Figure 1.7. This synchronizer overcomes the defects of the conventional synchronizer of friction cone clutch, it improves the smoothness and efficiency of the transmission, and simplifies the shifting strategy of multi-speed transmissions of electric vehicles [24]. The gear

engagement mechanism they proposed only includes a torsional spring and a dog clutch to reduce the rotational speed difference in gears engagement and absorb the transient shock during shifting, so that selection of teeth and engagement can be realized finally. Computer simulation results show that the rotational inertia and rotational speed difference of the mechanism influence the transient response of the Harpoon shift largely, and the rotational speed brings little torsional vibration in the system. Applying Harpoon shift to the transmission system together with appropriate control strategy, it can improve the shift quality of the transmission. In the test pneumatic actuator can move 20mm in 0.2s under 600KPa (47N force), which is equivalent to average 5W power consumption in gear engagement, that is acceptable.

Table 1.3 Vibrations (Noise) Classification of Electric Vehicle Powertrain

Vibrations (Noise)	Frequency (Hz)	Excitation Source	Influence
Shuffle	2~10	Load change and acceleration	Drive shaft stiffness, motor torque, etc.
Surge	0~100	Suspension Vibration Caused by Catastrophic Load	Powertrain suspension system characteristics
Lugging Vibration	0~100	Motor reversing drag	Suspension system, vehicle body
Clonk	300~500	Torque step change	Gear clearance, inertia, stiffness, etc.
Booming	0~200	Motor torque ripple	Drive shaft, suspension, suspension, body
Gear Rattle	1000~8000	Motor torque ripple	Gear clearance, motor torque ripple
Gear Whine	3000~4000	Gear transmission error	Gear stiffness, gear shape
Motor Whine	500~2000	Electromagnetic noise caused by structural errors	Control accuracy, assembly error, etc.

For full electric vehicle, the Noise, Vibration, and Harshness (NVH) of transmission system is different from that of conventional fuel vehicle. Vehicle with conventional

engine idles frequently with low running speed, it often approaches the first-order resonance frequency of the vehicle body. In contrast, the PMSM does not need to be idle to maintain the working state, the rotating motion of the rotor excites the drivetrain in a sweeping state from low to high frequency during acceleration. Although the sweeping process will come across the body's natural resonant frequency, it will pass instantaneously, so there is vehicle body resonance excited by motor idle speed. The main vibrational issues are listed as in the Table 1.3 [25-28]. Because of the good control and response performance of the motor, it is more feasible to apply active damping control algorithms for torsional vibrations in drivetrain by tuning motor torque than the conventional engine [29].

1.4.2.2 Research on Control Schemes for EV Powertrains

The Ford has applied a Proportional Derivative (PD) motor torque controller to achieve active damping control of the torsional vibration of the transmission system. Due to the limitations of the background and the development of the control theory, there is still room for improvement. Although the PID controller has a good versatility and parameter adjustment is very simple, it does not perform well in all control aims, and it is not optimal in performance. The basic difficulty of PID control is that it is a feedback control system with constant parameters and no direct knowledge of the target system, so the overall performance is passive and compromised. When the PID controller is singly used, the gains of the PID feedback loop must be reduced to avoid excessive overshoot or oscillation. When the system is nonlinear, it will encounter difficulties and a trade-off in response time must be made. The controller will not vary due to the time-varying system, so the response will delay a lot when the system comes across a large disturbance. In the PD controller designed by Ford, due to the lack of integral (I) part, although it avoids too much response time and large overshoot, it brings a considerable steady-state error, which is harmful to dynamic performance of electric vehicle [30,31].

In 2010, Fu Hong and Tian Guangyu et al. of Tsinghua University studied the control method of torsional vibration of motor-transmission integrated powertrain system. Unlike

the previous Ford PD control method, they analyzed the vibration characteristics of the electric vehicle powertrain equipped with motor-transmission integrated system and proposed a motor control scheme based on linear quadratic regulator (LQR) with an observer to realize the active damping control so that the drivetrain torsional vibrations are suppressed by motor control [32]. They also use the motor output speed, drive shaft torsional angle and wheel speed as system state variables. Since the drive shaft torsional angle is a parameter that difficult to be measured directly, they introduced the Luenberger dimensionality reduced-order observer which uses motor torque and motor speed as input, observed drive shaft torsional angle and wheel speed are obtained based on appropriate pole placement. Simulation results show that Luenberger reduced order observer can effectively estimate the necessary state variables, and the linear quadratic regulator can effectively attenuate the vibration of the drivetrain.

Similarly, in the aspect of optimizing the driving performance of electric vehicles by controlling motor torque, Shi Junhui et al. from Beijing University of Technology aimed to improve the comfort of battery urban electric bus in 2016, they optimized the torque control scheme for drivetrain and reached the target of restraining vibration and shock [33]. Their research target is a battery urban electric bus with coaxial series dual motor driving system, and the mathematical model of the powertrain is established as well, which provides a simulation base for the optimization of torque control. By analyzing the influence of torque step change on vibration shock of the transmission system, optimization issue is solved based on the Model Predictive Control (MPC) and the optimal torque control law is obtained. Comparisons from simulation results show that the model predictive control can effectively reduce the vibration and impact of the drivetrain under the same dynamic performance of the urban electric bus. Moreover, they also built a test rig for the dual-motor driving system to verify the effectiveness of the proposed strategy and vehicle prototype test was carried out too. The experimental results show that the proposed torque control optimization strategy based on the model predictive control algorithm can suppress the vibration and shock to the drivetrain effectively.

As for the shift quality improvement, in order to shorten the power interruption time

during shifting, for the clutchless motor and AMT integrated drive system, P. Walker of the University of Technology Sydney, Australia proposed shift control scheme as in Figure 1.8 by motor speed tuning, motor tuning in closed-loop and replacing the friction clutch function of the block-ring with cooperation from the synchronizer actuator [34].
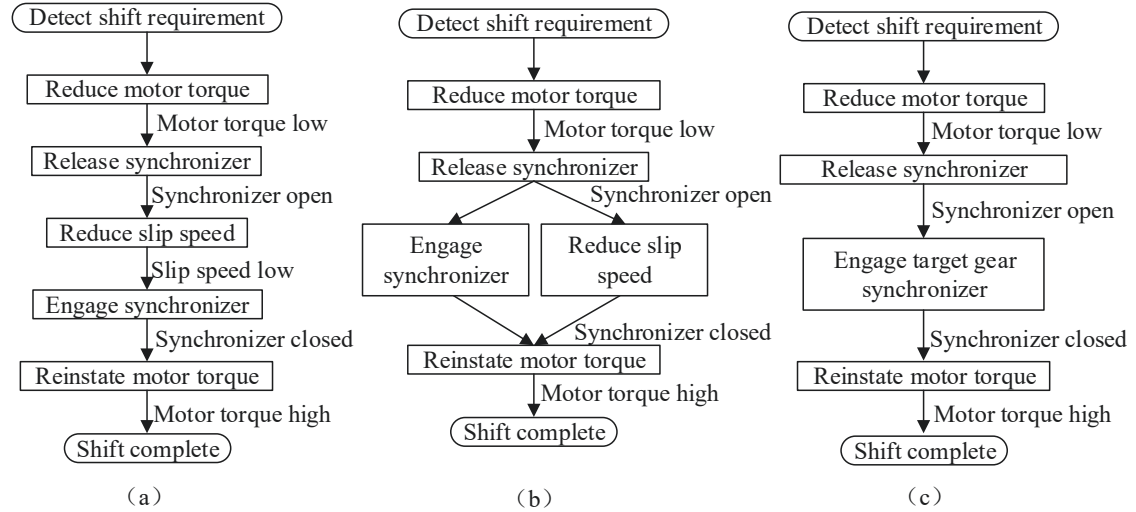
Figure 1.8 Alternative Shifting Strategies

In order to achieve this goal, multi-body dynamics mathematical modeling of an EV powertrain with a clutchless AMT, DC motor, and synchronizer was established. The shift quality is evaluated from longitudinal impact, vibration and shift time of the vehicle, based on these three parameters series of researches were carried out, which focus on shifting up and shifting down under control for motor and synchronizer integrated system. Conclusions can be drawn as follows: (1) the most important factor affecting vehicle longitudinal impact and transient vibration in shifting is unloading and recovery of motor torque during the preparation stage of motor speed synchronization; (2) minimization of shift time can be achieved by reducing the various stages of shift control, but at a cost of increased longitudinal vibration and shock; (3) by applying electric drive control, speed regulation stage of gear shifting can be achieved successfully. However, for typical gear shifting process, this stage only accounts for 30% of the total shift time. (4) by applying a high-quality motor control scheme shifting can be completed without using the conical friction clutch in the synchronizer. However, due to the probability of shift failure during the shifting process, it is still necessary to keep the synchronizer.

Furthermore, Frank J. Falcone et al. from Argonne National Laboratory in the United States have studied the effect of the speed difference sleeve and target gear on active synchronization process. In the study, the speed difference is set between 0.5 rpm and 60 rpm. The research results show that speed between the target gear and the engagement sleeve can be synchronized quickly by motor speed tuning. When the speed difference is 0.5 rpm, the synchronization time takes about 1s, and when the speed difference is 60 rpm, the synchronization time takes about 0.1s. Therefore, applying the active synchronization control strategy with motor speed tuning can replace synchronization of mechanical friction [35].
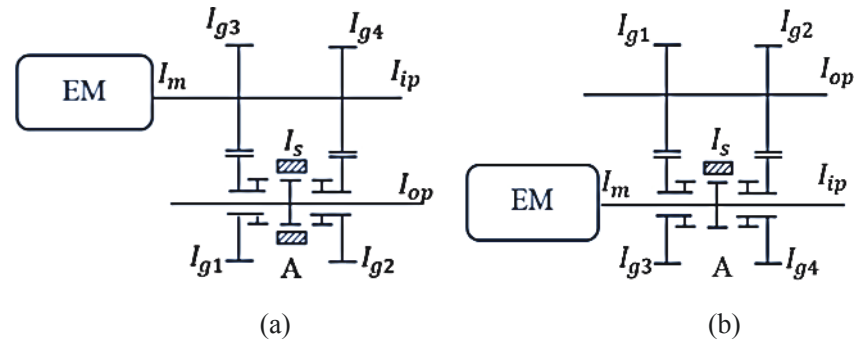
Figure 1.9 (a) Case I, (b) Case II

A. Penta and R. Gaidhani of Indian Tata Automobile Company have studied the active synchronous speed tuning for clutch-free full electric drive and hybrid vehicle with two-speed transmission and optimized the position of synchronizer to improve the shift quality. Through the shift simulation experiments in two cases as shown in Figure 1.9, conclusions can be drawn as follows: In case I, the active synchronization time is 75ms, the synchronizer engagement time is 139ms, and the total time consumes 214ms. In case II, the active synchronization time is 62ms and the synchronizer engagement time is 110ms, the total time consumes 172ms; downshift time is 30% less than upshift time when the synchronizer is mounted on the transmission input shaft, 20% less than that when the synchronizer is mounted on the output shaft [36].

In recent years, many researchers have deeply studied this active synchronization technology based on motor speed regulation. They either proposed more advanced speed

regulation mode or carried out relevant experimental verification [37-40]. In 2013, M. Reinholds and S. Andreasson of Lunde University, Sweden used PID to control the motor speed to synchronize sleeve speed and gear ring speed. Shifting experiments from 3rd gear to 5th gear was carried out on LabView. When the speed was higher than 1000rpm, the shift time was improved by 67.4% [41]. In 2015, C.Y.Tseng et al. of National Pingtung University of Science and Technology in Taiwan proposed a robust control strategy based on double-layer neural network for AMT synchronizer of clutchless electric vehicle. Their research points out that the shifting operation of clutch-free AMT requires not only a motor that mode can be switched quickly with high accuracy in speed control but also the shifting actuator with precise position adjustment and good robustness to shifting load change. The key technology to achieve fast and accurate shifting control is the shifting actuator of which moving can be controlled robustly. Therefore, they established a test bench for active gears synchronization using speed tuning control based on the two-layer neural network robust control algorithm and performed a shift test. The experimental results are listed in Table 1.4 [42].

Table 1.4 Time Consumption of Shifting Process

Operations	Shift Up (s)				Shift Down (s)			
	1→2	2→3	3→4	4→5	5→4	4→3	3→2	2→1
Open	0.31	0.31	0.3	0.3	0.3	0.31	0.3	0.31
Selection	0.01	0.26	0.01	0.26	0.24	0.01	0.26	0.01
Synchronization	0.96	0.82	0.78	0.72	0.44	0.56	0.68	0.7
Engagement	0.42	0.4	0.4	0.39	0.38	0.41	0.41	0.42
Total Time	1.69	1.53	1.48	1.41	1.12	1.28	1.39	1.43

During the forward movement of shifting in AMT transmission, the sleeve is driven by the axial force to push the bronze lock ring to realize speed synchronization with the cone clutch of the target gear by mechanical friction, therefore, the sleeve and the target gear can be pushed to engage. During this process, it consumes a while and impact and sliding work are generated, which brings about adverse effects such as power interruption, shift shock and synchronizer abrasion. As mentioned above, the power interruption duration

and impact are a pair of contradictory indicators, so it is meaningful to find the comprehensive optimal or weighted optimal decision for power interruption time and shift quality [43-45]. Zhao X. and Chen H. et al. of Beijing University of Technology have designed a series controller based on fuzzy control algorithm, of which control target is the impact and sliding power, so that the sliding power can be reduced under the same shift quality, and life of synchronizer is prolonged as well [46]. Lin S. et al. of Nanjing University of Science and Technology has taken the impact and sliding work of synchronization stage as the optimization objective, and established the comprehensive objective functional, by introducing the optimal control algorithm based on the minimum principle, comprehensive optimization of shift quality is achieved. The experimental results shown in Table 1.5 and Table 1.6 are obtained through test rig experiments. Table 1.5 shows the evaluations of shift quality before and after optimization. Table 1.6 compares the shift quality of three groups of speed difference, and conclusions can be drawn that synchronization time, shift sliding power and maximum impact increase with the of speed difference [47].

Table 1.5 Comparisons of Shift Quality

Group	Shift Time (ms)	Synchronization Time (ms)	Sliding Work (W/J)	Maximum Impact (rad/s^3)
Optimized	138.1	88.6	87.1	194.8
Unoptimized	125.5	83.1	84.6	386.5

Table 1.6 Comparisons of Shift Quality in Different Conditions

Speed Difference	Shift Time (ms)	Synchronization Time (ms)	Sliding Work (W/J)	Maximum Impact (rad/s^3)
500r/min	128.1	80.2	75.8	149.4
600r/min	139.5	87.7	87.1	188.3
700r/min	147.6	97.8	109.5	226.8

1.4.2.3 Research on Advanced Control Algorithms for EV Powertrains

The control system of electric vehicle is one of the most important parts of electric vehicle. It plays a decisive role in the power, economy, comfort and safety of electric vehicle. The electronic control system occupies an increasing proportion in vehicle development and production. Not only the hardware design but also the software based on various advanced control algorithms as brain and soul of vehicle are developed as well, it is a key technique and decisive factor that affects vehicle performance [48-53].

In engineering practice, PID controller is still widely used. According to the error from system feedback, the control signal is regulated or compensated by proportional, integral and differential operations [54-57]. PID control algorithm has many advantages, such as model-independent, simple application, convenient parameter regulation and good stability. However, with the improvement of control accuracy, it is always necessary to establish time-varying and non-linear dynamic models of vehicle systems more precisely and practically, from which parameters are less and less neglected. However, as control plants of simple Single-Input Single-Output (SISO) systems are more and more replaced by Multiple-Input Multiple-Output (MIMO) systems, performance of PID controller is not satisfactory for these requirements [58-60].

Model-based control algorithms are becoming more widely used with the advancement of embedded systems [61,62], by using this method a common framework for communication through the "V-shaped flow development process" can be effectively established [63]. By applying various advanced control algorithms, performance of the designed controller can be easily simulated on Matlab/Simulink and then the underlying execution programs such as C code or C++ code can be generated as well, download the codes of the control algorithms to the Rapid Control Prototype (RCP) and then comprise a Hardware-In-the-Loop (HIL) experimental system. Therefore, online simulational experiments can be realized to provide convenience for developing control system based on advanced control strategies [64,65]. Therefore, the more controllable electric vehicle provides a platform for the development and application of various advanced control

algorithms. This thesis analyzes and compares the common algorithms of parameter estimation, state observation and active motor damping control for electric drive vehicle drivetrain, and then based on the existing problems novel algorithms are proposed which aim to improve the drivability of electric vehicles.

(I) Estimation of Parameters and States for Vehicles

The parameter estimation of control theory serves the parameters that cannot be measured by sensors directly or conveniently, it uses the measurable signals and corresponding model-based algorithms. In 1794, the German mathematician Gauss first realized the parameter estimation for calculating the orbit of celestial bodies by least squares method. With the rapid development of electronic computers, there came about many traditional classical parameter estimation methods, such as least squares method, maximum likelihood method, etc. However, these methods are mainly used for offline estimation, vehicle active control systems usually require online estimation or real-time estimation, which are used for fault diagnosis or real-time control requirements. Therefore, researchers have proposed various real-time estimation algorithms mainly including Kalman Filter (KF) and its extension algorithm, Recursive Least Square (RLS), Luenberger Observer, Sliding Mode Observer (SMO), Dynamic Simplex Method, Multi-Model Switching Method, etc. [66-68], in this part of the thesis some typical and commonly used algorithms are selected for discussion.

(i) Recursive Least Squares

Recursive least square is an adaptive filtering algorithm, which uses the known initial parameters to recursively search the factors that minimize the weighted linear least square cost function relating to the information input, and update the filter parameters according to the new information input. In 2016, Ding Feng of Jiangnan University has studied the recursive least squares parameter estimation of a nonlinear system based on model decomposition. The research shows that this method consumes less computational power than that of over-parameterized model and can effectively estimate the parameters of

nonlinear systems [69]. A. VAHIDI et al. of Ann Arbor University of Michigan, USA, have proposed a least square method with a forgetting factor to estimate the vehicle mass and road slope. By simulation conclusions can be drawn that estimation error of vehicle mass in within 5%, it can also track the time-varying road slope with noise accurately. For the problems such as the lack of continuous incentives or the difficulties in parameters tracking during shifting process, explain and suggestion are given to avoid these issues [70].

So far, the estimation algorithms based on least squares or recursive least squares are still popular for vehicle mass estimation, such as the work of Changfu Zong et al. from Jilin University in China, who have researched the recursive least squares algorithm with two unknown parameters is used to estimate both vehicle mass and system error considering color noise . Performance in tests turned out that the percentage of mass error was 16% in road test, the percentage of mass error is 7.2% with system error considered, the precision of mass estimation improves by 8.8% [71]. The advantages of recursive least squares are obvious such that the convergence rate is insensitive to the eigenvalue dispersion of the covariance matrix of array signals, and it converges quickly. But disadvantages of the recursive least squares should not be neglected such that high computational complexity, biased parameter estimation due to noise or outliers will be generated [72,73], and even unstable performance may come about [74]. Furthermore, O. P. MALIK et al. of the University of Calgary in Canada have also pointed out some problems in the practical application of recursive least square for system identification: although the recursive least square performs well in simulation, it is not satisfactory in practical application because of the differences in simulation and practice. Some systems can be expressed by an exact real value θ_0 and a measurable certain order mathematical model, but in most industrial operations θ_0 is only be valuable in analysis, because the practical systems are always non-constant, nonlinear and time-varying [75]. It is worth to mention that, in order to get faster transient and better steady-state performance than recursive least square for vehicle parameters (mass) estimation, Prof. Jing Na from

University of Bristol proposed an adaptive estimation law based on finite-time parameter estimation, which was also proved to be robust to bounded disturbances [76].

(ii) Kalman Filters and Extension

Classical Kalman filter is based on Bayesian estimation theory and with self-learning. For linear state equation with Gauss distribution noise, the analytic solutions of posterior distribution can be obtained according to recursive linear filtering formula. Therefore, decisions can be made according to the measured data and the filter parameters can be regulated to make it adaptive, thus an approximated optimal state estimation can be obtained [77]. Kalman filtering theory uses state equation to describe the system in time domain. The recursive form of Kalman filtering algorithm can reduce the data storage, Kalman filter can not only be applied to the stationary stochastic processes but also multidimensional and non-stationary stochastic processes [78]. However, the classical Kalman filters are only suitable for linear systems, so many suboptimal approximation methods are proposed for the suboptimal approximation of nonlinear filtering problems, Gauss approximation methods are mainly used, including: (1) Taylor series expansion for linearization of the nonlinear part of the nonlinear functions, such as Extended Kalman Filter (EKF); (2) using sampling methods to approximate nonlinear probability distributions, such as Unscented Kalman Filtering (UKF) that applies Unscented Transformation (UT) to nonlinear transfer of mean and covariance [79]. F. Gustafsson of Linkoping University, Sweden pointed out that the difference between extended Kalman filter and unscented Kalman filter is that one is based on discrete Riccati equation and the other is based on conditional expectation formula without explicit Riccati equation. Firstly, the function of the sample points (sigma points) can be applied to the Extended Kalman filter, but not to the explicit linear model. Second, the second-order Taylor expansion-based extended Kalman filter (EKF2) is very close to the unscented Kalman filter. They also used $z = g(x)$ where x is nonlinear mapping of Gaussian distribution, by comparing the second-order extended Kalman filter with the unscented Kalman filter, conclusions can be drawn that even the unscented transformation of quadratic function

cannot get the correct second moment. This can be illustrated by the counterexample of $g(x) = x^T x$ which exists analytic solutions. But for standard sensor models, unscented transformation can perform well [80].

(iii) Sliding Mode Observation Algorithms

Since the Sliding Mode (SM) algorithm has been put forward and applied to practice for decades, Sliding Mode Control (SMC) has been considered as a very effective means to control a variety of nonlinear systems with good robustness to disturbance [81,82], sliding mode controller is still one of the most satisfactory choices in engineering practice so far [83-85]. Based on the variable structure control theory, researchers have proposed various types of Sliding Mode Observers (SMO) to robustly observe the state or parameters for nonlinear systems, and they are widely introduced in sensorless control, fault diagnosis and other occasions to meet the requirements of reducing costs and adaptability to harsh working conditions better [86-90]. However, one of the main drawbacks of the sliding mode algorithm is the "chattering" issue, which is caused by the discontinuous switching function (sign function) in the algorithm. This is an inherent defect and impossible to be totally eliminated, but measures can be taken to reduce.

At present, there are three typical methods to reduce the chattering [91]:
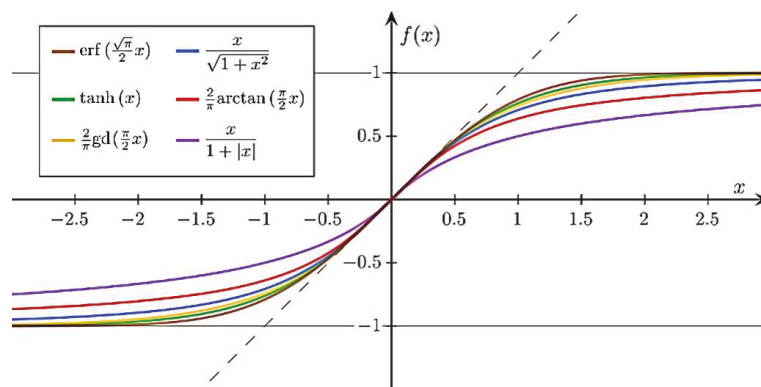
Figure 1.10 Various Approximate Functions of the Sign Function

(a) Approximate the discontinuous sign function with the continuous functions such as "saturation function", "S function", "anti-tangent function" as shown in Figure 1.10

[92], these are the simplest and most widely used methods to reduce chattering but are not ideal switching modes. When the observation error converges close to zero, it will introduce bias and affect the convergence rate.

(b) Introduce higher order sliding mode observers [93,94]. It has been applied to practice successfully such as PEM fuel cell system [95,96] and estimation of tire friction [97] etc. However, the generalization of r th-order ($r \geq 3$) sliding mode observer is limited by high relative degree issues, consecutive derivatives of the variable ($s, \dot{s}, \ddot{s}, \cdots s^{(n-1)}$) must be known. It is worth noting that, as one of the most powerful second-order sliding mode observers, super-twisting (STW) only needs information on the sliding variable s [98-100]. It can generate a continuous function to drive the sliding variables and derivatives of sliding variables to 0 in a finite time and it shows a good robust performance without knowing the boundary of disturbance exactly [101]. Based on the twisting controller, Levant et al. proposed a modified twisting controller for uncertain dynamic systems with relative degree 2, the convergence rate is prescribed in advance and the twisting control algorithm can be accelerated [102].

(c) Introduce an adaptive gain [91,103,104]. The variable gain will vary with distance between the trajectory and sliding mode switching manifold, if deviation is larger than a certain range, the adaptive gain will be increasing to force the trajectory back to sliding mode switching manifold and if deviation is small, the adaptive gain will reduce to prevent the system from overshoot. This can attenuate chattering and compensate perturbations of which boundaries are time-variant more accurately [105]. The adaptive super-twisting (ASTW) algorithm has been applied in sensorless control for permanent magnet synchronous motor with good performance [106].

(II) Active Damping Control Algorithms for Drivetrains

Active damping is an algorithm which is used to reduce oscillations in the motion control systems and usually requires known signals of acceleration or force of the system. The

concept of active damping was applied to satellite attitude control as early as the 1960s [107]. With the progress of the cost and performance of electronic equipment, the application of active damping is becoming more and more common in vehicle control systems [108].

When the vehicle accelerates, the elastic parts of the drivetrain will cause torsional vibration, which will bring about vehicle body longitudinal vibration further. This vibration commonly acts as shuffle or low-frequency vibration of about 1-5Hz [109] which may even be close to the first-order resonant frequency of the entire drivetrain. Therefore, many active damping control algorithms have been proposed sequentially, the core principle is to use motor (engine in traditional vehicle) as an actuator to provide reverse compensation for oscillation. Among them, some are applied commonly such as the Model Predictive Control (MPC), the Linear Quadratic Gaussian (LQG) as an optimal control, the pole configuration and other algorithms that constitute a speed closed-loop feedback for the powertrain [110-112].

(i) Model Predictive Control Algorithms

Model predictive control is an advanced process control algorithm, which was used in fields of chemical industry, power system and power electronics in the 1980s. In recent years, it has also been valued and used in vehicle control systems. Model predictive controller depends on the dynamic mathematical model of the system and can deal with constraints well [113]. The main advantage of model predictive control is that it can optimize the current moment online and consider the future moments through repeated optimization and take corresponding control actions, so it is also moving horizon optimal control [114]. As an optimal control algorithm, the model predictive control also has the basic characteristics of optimal control. No matter what form of model predictive is, it has the following three basic characteristics: model predictive, rolling optimization and feedback correction [115].

The advantages of the model predictive control algorithm include: (1) the convenient

modeling, of which process description can be obtained through experiments, it is unnecessary to understand the internal process of the system as a "black box model"; (2) discrete convolution model with non-minimization description is adopted, which has a large information redundancy and improves the robustness of the system; (3) by adopting the rolling optimization scheme and through the repeated online optimization calculation, the uncertainty caused by model error and disturbance can be compensated, so that dynamic control performance is improved; (4) MPC can be extended to systems with constraints, large delay and non-minimum phase, etc. to obtain better control performance [116].

Professor Xi Y. from Shanghai Jiaotong University has pointed out some shortcomings of the model predictive control algorithm such as: (1) currently model predictive control is mainly applied to slow dynamic processes and requires computing power in high-performance because of the multiple online optimization calculations, so the promotion and application are limited a lot; (2) as to the application object, the model needs to be linear or quasi-linear; (3) as to the application skills, it mainly depends on the designer's experience [117].

(ii) Optimal Control

The optimal control is used to solve the optimal control law to optimize the performance index of the system. Optimal control is a series of differential equations describing the trajectory of control states that minimize the cost function. From a mathematical point of view, the target of optimal control theory is to solve a class of extremum problems with constraints, which belongs to the theoretical category of variational. However, the classical variational theory can only solve a class of optimal control problems that belong to the open set, however, most of the problems in engineering practice belong to the closed set and the classical variational theory is powerless in these problems solving [118]. In the mid-to-late 1950s, the Soviet cybernetic expert Pontryagin and the American scholar Berman almost simultaneously proposed two methods for solving the optimal control problem — Pontryagin Maximum Principle and Bellman Dynamic Programming Method,

which become the effective and commonly used methods in modern variational principles [119].

In engineering practice, especially the vehicle operations which will face various working conditions and expose to harsh working environment with disturbance in large scale. Therefore, it is quite necessary to introduce the closed-loop control, of which control laws can be expressed as functions of time and state. Generally, it is difficult to solve this kind of problem, but for a kind of linear dynamic system with quadratic index, it has been completely solved. It is not only mature in theory and simple in the control law mathematically, but also easy to realize in engineering practice, so it is widely used in engineering [120].

One obvious weakness of the Linear Quadratic Regulator (LQR) is that all states need to be measured in feedback. In most cases, not all states are always measurable, so these unmeasurable states must be obtained by observers, such as the classical Kalman filter. In practical application of vehicle system, random measurement noise exists in sensor or state observer. Considering random noise of the input, the linear quadratic optimal control forms a Linear Quadratic Gauss (LQG) algorithm, which can solve the problem of optimal controller designing with disturbance in data collection or unmeasurable state variables.

LQG designing is divided into the following two independent processes: (1) the optimal control law designing, which regards the system as a deterministic system without considering random disturbance and measurement noise. At the same time, it is assumed that the feedback includes all necessary states of the system. (2) optimal state estimating, the actual feedback signal is not the actually measured state of the system, but the result of state observation [121]. So far, the optimal control is still considered to be one of the most effective means of vibration active control, but on the premise that the weight parameters are selected appropriately for obtaining the optimal control law so that performance index can be minimized [122-124]. The weight matrices Q and R directly affect the optimal control results. However, the choice of them is usually based on

subjective preference or attempt of the designer. Such "optimal" result is probably not the objective "optimal" actually and may even cause side effects, so researchers are actively looking for the ways to properly select the weight matrices for better control performance [125-127]. In 2017, Professor Lin C. et al. from Beijing Institute of Technology have proposed a linear quadratic regulator combined with a Genetic Algorithm (GA) controller to control the oscillations of the electric vehicle powertrain actively. It takes the sum of the Root Mean Square (RMS) of motor speed, torsional angle of drive shaft and wheel speed as the cost function, the genetic algorithm is used to search the optimal weight offline, so as to reduce the torsional oscillations of drivetrain and optimize shift quality [128].

1.5 Publications

Journals:

[1] **Shengxiong Sun***, Nong Zhang, Paul Walker, Cheng Lin. Intelligent Estimation for Electric Vehicle Mass with Unknown Uncertainties Based on Particle Filter. IET Intelligent Transport Systems, accepted, DOI: 10.1049/iet-its.2019.0453.

[2] Cheng Lin, **Shengxiong Sun***, Paul Walker, Nong Zhang. Accelerated adaptive second order super-twisting sliding mode observer. IEEE Access, 2019, 7(1): 25232-25238.

[3] Cheng Lin, **Shengxiong Sun***, Jiang Yi, Paul Walker, Nong Zhang. Accelerated adaptive super twisting sliding mode observer-based drive shaft torque estimation for electric vehicle with AMT. IET Intelligent Transport Systems, 2019, 13(1): 160-167.

[4] Cheng Lin, **Shengxiong Sun***, Paul Walker, Nong Zhang. Off-Line Optimization Based Active Control of Torsional Oscillation for Electric Vehicle Drivetrain. Applied Sciences, 2017, 7(12): 1261.

[5] Cheng Lin, **Shengxiong Sun***, Wenfei Jiang, Modelling and active damping of powertrain oscillations for RWD electric vehicle. International Journal of Powertrains, 2017, 6(4): 371-382.

[6] Cheng Lin, Zhifeng Xv*, Hong Zhang, **Shengxiong Sun**. Research on Driving Torque Control Strategy for Distributed Drive Electric Vehicle. Journal of Beijing Institute of Technology, 2016, 36(7): 668-672.

Conference:

[1] Cheng Lin, **Shengxiong Sun***, Wenfei Jiang. Active Anti-jerking Control of Shifting for Electric Vehicle Driveline. Energy Procedia, 2016, 104: 348-353.

CHAPTER 2: MODELLING AND ANALYSIS OF THE ELECTRIC VEHICLE POWERTRAIN

2.1 Introduction

The research object in this thesis is based on the powertrain of electric logistics vehicle as shown in Figure 2.1 (a) which belongs to the rear centralized driving configuration including the power battery, permanent magnet synchronous motor, and two speed AMT transmission, drive shaft, final drive, drive shafts and wheels. In order to reduce the low frequency excitation response of the drivetrain (including vehicle body) to the motor input when the pedal is frequently tipped in/out during traffic jam or low speed driving, configuration shown in Figure 2.1 (b) that equipped with a torsional damper based on Figure 2.1 (a) is researched.

(a)   (b)
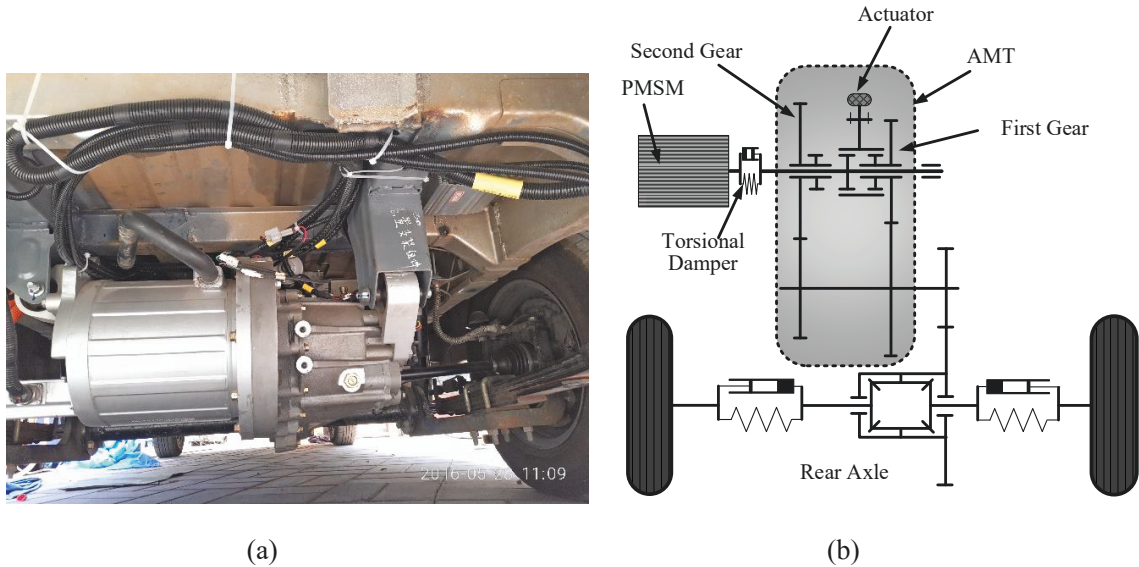
(a) Powertrain of the Electric Logistics Vehicle   (b) Corresponding Powertrain Equipped with Torsional Damper

Figure 2.1 Configuration of the EV Powertrain in This Thesis

Compared with the traditional fuel vehicle powertrains, the flywheel is no more necessary to buffer the alternating torque from the engine crankshaft and drive the pistons to pass the dead point, so it consumes less energy. The clutch mechanism is removed to make the

system more integrated and compact. Moreover, the shift control system can be simplified and time of power interruption is shortened [129]. In this chapter, mathematical model of all parts of EV powertrain is established and analyzed by MATLAB/Simulink which include dynamic characteristics, natural frequencies and mode shapes, etc. Chapter 2 provides a base and object for vehicle parameters estimation, states observation and active damping control in the following chapters.

2.2 Modelling of the EV Powertrain

The driving power generated by the PMSM is transmitted to wheels through all parts of the powertrain. The model includes multiple moments of inertia and elastic damping joints, it is necessary to model each part to obtain the motion states from PMSM to wheels and then reveal the motion relationship of the whole EV powertrain.

2.2.1 Principles of Establishing Dynamic Equations for EV Powertrain

In this thesis, the principle of momentum theorem and angular momentum theorem of the Newton Vector Mechanics and Lagrange analytical mechanics principle are applied to establish the differential equations of EV powertrain motion states [130].

(I) Newton Vector Mechanics System

(i) Momentum theorem of particle system: the time derivative of the momentum vector $\boldsymbol{p}$ of the particle is equal to all external forces $\sum F_i$ acting on the particle system, which expresses as follows:

$$\frac{\mathrm{d}\boldsymbol{p}}{\mathrm{d}t} = \sum \boldsymbol{F}_i \tag{2.1}$$

In form of momentum theorem of particle system:

$$m\ddot{\boldsymbol{r}}_c = \sum \boldsymbol{F}_i \tag{2.2}$$

Where m is total mass of the particle system, $\ddot{\boldsymbol{r}}_c$ is the centroid acceleration of particle

system.

(ii) Angular momentum theorem of particle system: the time derivative of the angular momentum L_0 to a fixed point O is equal to the moment M_0 of all external forces about O, which can be expressed as

$$\frac{\mathrm{d}L_0}{\mathrm{d}t} = M_0 \tag{2.3}$$

For a single rigid body, angular momentum L is equal to the product of the moment of inertia I and the angular speed ω, which can be expressed as

$$L = I\omega \tag{2.4}$$

By application of the projection of the angular momentum theorem, i.e. the corresponding Euler equation of the rigid body is

$$I\dot{\omega} + \tilde{\omega}L\omega = L_0 \tag{2.5}$$

Where ω is the angular velocity projection matrix, $\omega = (\omega_x, \omega_y, \omega_z)^{\mathrm{T}}$, $\tilde{\omega}$ is the antisymmetric matrix $\tilde{\omega} = \begin{pmatrix} 0 & -\omega_z & \omega_y \\ \omega_z & 0 & -\omega_x \\ -\omega_y & \omega_x & 0 \end{pmatrix}$.

(II) Analytical Mechanics Principle

Analytical mechanics is applicable to the constrained particle systems and is a method for solving mechanical problems using mathematical analysis.

(i) General equation of dynamics: i.e. D'Alembert-Lagrange principle, the establishment of the equation is based on the principle of virtual displacement expressed as follows:

$$\sum_{i=1}^{n} \delta r_i \cdot \left(-m\ddot{r}_i + F_i^a \right) = 0 \tag{2.6}$$

Where $-m\ddot{r}_i$ is the inertial force acting on the particle i, F_i^a is the active force acting on the particle i, δr is the virtual displacement of the particle i.

(ii) Lagrange equation: the principle of Lagrange method is to express the total kinetic

energy of a system with variables of the system, then it is substituted into the Lagrange equation and take the partial derivative, therefore, an equation expressing motion states of the system can be obtained. The Basic form of the Lagrange equation is expressed as

$$\frac{\mathrm{d}}{\mathrm{d}t}\left(\frac{\partial E_T}{\partial \dot{q}_i}\right) - \frac{\partial E_T}{\partial q_i} = F_{Qi} \;,\left(i = 1, 2, \cdots n\right) \tag{2.7}$$

Where F_{Qi} is the generalized active force corresponding to generalized coordinates, E_T is the kinetic energy function of the system, q_i is the generalized coordinates of the particle i, n is order of the equation. In the modelling of vehicle system dynamics F_{Qi} can be regarded as generalized external force, then the corresponding Lagrange equation can be expressed as

$$\frac{\mathrm{d}}{\mathrm{d}t}\left(\frac{\partial E_T}{\partial \dot{q}_i}\right) - \frac{\partial E_T}{\partial q_i} + \frac{\partial E_V}{\partial q_i} + \frac{\partial E_D}{\partial \dot{q}_i} = F_{Qi} \;,\left(i = 1, 2, \cdots n\right) \tag{2.8}$$

Where E_T is the total kinetic energy of the system, E_V is the total potential energy of the system, E_D is the total dissipative energy of the system.

Furthermore, there are virtual work principle and Gauss principle. The principle of virtual work is another general equation of dynamics derived by Jordan in 1908, of which general dynamic equation is

$$\sum_{i=1}^{n} \delta \dot{r}_i \cdot \left(-m\ddot{r}_i + F_i^a\right) = 0 \tag{2.9}$$

Where $\delta \dot{r}$ is variable of virtual speed of particle i. In 1829, Gauss derived another form of general equation of dynamics, which is called Gaussian principle and expressed as

$$\sum_{i=1}^{n} \delta \ddot{r}_i \cdot \left(-m\ddot{r}_i + F_i^a\right) = 0 \tag{2.10}$$

Where $\delta \ddot{r}_i$ is the variation of Gauss acceleration.

2.2.2 Modelling of the Permanent Magnet Synchronous Motor

Permanent magnet synchronous motor is the mainstream driving configuration scheme of electric drive vehicles currently, of which structure is shown in Figure 2.2.
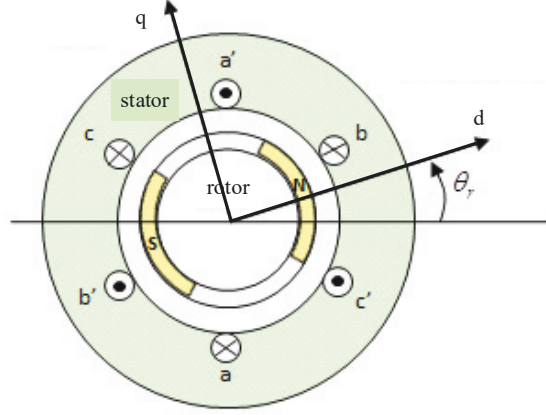
Figure 2.2 Permanent Magnet Synchronous Motor Physical Model

On the stator of the permanent magnet synchronous motor, three-phase symmetrical windings with an electrical angle of 120° in space are installed. The three-phase voltage equation of permanent magnet synchronous motor in a natural coordinate system is:

$$u_s = Ri_s + L\frac{di_s}{dt} + \frac{d\psi_s}{dt} = Ri_s + \frac{d\psi}{dt} \tag{2.11}$$

The corresponding flux equation in three-phase coordinates A, B and C is

$$\psi = Li_s + \psi_s \tag{2.12}$$

Where $u_s = \begin{bmatrix} u_A & u_B & u_C \end{bmatrix}^T, i_s = \begin{bmatrix} i_A & i_B & i_C \end{bmatrix}^T, \psi = \begin{bmatrix} \psi_A & \psi_B & \psi_C \end{bmatrix}^T, R = \begin{bmatrix} R_s & 0 & 0 \\ 0 & R_s & 0 \\ 0 & 0 & R_s \end{bmatrix}$,

$L = \begin{bmatrix} L_A & M_{AB} & M_{AC} \\ M_{BA} & L_B & M_{BC} \\ M_{CA} & M_{CB} & L_C \end{bmatrix}$, $\psi_s = \psi_f \begin{bmatrix} \sin(\omega t + \theta) \\ \sin\left(\omega t + \theta + \frac{2\pi}{3}\right) \\ \sin\left(\omega t + \theta + \frac{4\pi}{3}\right) \end{bmatrix}$, i_A, i_B, i_C is currents of three-

phase winding, respectively; u_A, u_B, u_C is voltage of three-phase winding, respectively;

ψ_A, ψ_B, ψ_C is flux linkage of three-phase winding, respectively; L_A, L_B, L_C is self-inductance coefficient of three-phase winding, respectively; R_s is resistance of motor

stator winding; $M_{XY} = M_{YX}$ is mutual inductance of stator winding; ψ_f is excitation flux linkage of rotor permanent magnet pole; θ is the electrical angle of the rotor. According to the principle of motor energy conversion, electromagnetic torque T_e equals to mechanical angular displacement θ_m partial derivative of the potential energy of the magnetic field, therefore,

$$T_e = \frac{1}{2} p_n \frac{\partial}{\partial \theta_m} \left(i_s^{\mathrm{T}} \cdot \psi_s \right) \tag{2.13}$$

The corresponding mechanical motion equation of the motor is:

$$J_m \frac{\mathrm{d}\omega_m}{\mathrm{d}t} = T_e - T_L - T_{fric} \tag{2.14}$$

Where p_n is pair amount of magnetic pole of permanent magnet synchronous motor, ω_m is mechanical angular speed of the rotor, J_m is moment of inertia of the rotor, T_{fric} is friction torque, T_L is load torque.

However, from the equation (2.12) it can be seen that under the natural coordinate A, B, C, mathematical model of the PMSM is a nonlinear time-varying function of motor position, which brings much trouble in analysis and control. In order to simplify the mathematical model under natural coordinate, static coordinate transformation (Clarke transformation) and synchronous rotation coordinate transformation (Park transformation) are usually employed. Figure 2.3 illustrates the relationship between ABC natural coordinate, α-β stationary coordinate and d-q synchronous rotation coordinate.
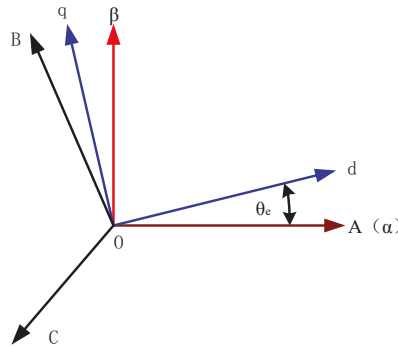
Figure 2.3 Relationship of the Three Coordinates

Convert the natural coordinate to the stationary coordinate, i.e. the Clarke transformation, and according to the coordinate transformation relationship in Figure 2.3, the following relationship can be obtained:

$$\begin{bmatrix} f_\alpha & f_\beta & f_0 \end{bmatrix}^{\mathrm{T}} = \boldsymbol{T}_{3s/2s} \begin{bmatrix} f_A & f_B & f_C \end{bmatrix}^{\mathrm{T}} \tag{2.15}$$

Where f indicates the voltage, current and flux linkage, etc., $\boldsymbol{T}_{3s/2s}$ is the coordinate transformation matrix, expressed as

$$\boldsymbol{T}_{3s/2s} = \frac{2}{3} \begin{bmatrix} 1 & -\dfrac{1}{2} & -\dfrac{1}{2} \\ 0 & \dfrac{\sqrt{3}}{2} & -\dfrac{\sqrt{3}}{2} \\ \dfrac{\sqrt{2}}{2} & \dfrac{\sqrt{2}}{2} & \dfrac{\sqrt{2}}{2} \end{bmatrix} \tag{2.16}$$

Convert the stationary coordinate to the natural coordinate, i.e. inverse Clarke transformation, which is expressed as

$$\begin{bmatrix} f_A & f_B & f_C \end{bmatrix}^{\mathrm{T}} = \boldsymbol{T}_{2s/3s} \begin{bmatrix} f_\alpha & f_\beta & f_0 \end{bmatrix}^{\mathrm{T}} \tag{2.17}$$

Where $\boldsymbol{T}_{2s/3s}$ is the coordinate transformation matrix, expressed as

$$\boldsymbol{T}_{2s/3s} = \boldsymbol{T}_{3s/2s}^{-1} = \begin{bmatrix} 1 & 0 & \dfrac{\sqrt{2}}{2} \\ -\dfrac{1}{2} & \dfrac{\sqrt{3}}{2} & \dfrac{\sqrt{2}}{2} \\ -\dfrac{1}{2} & -\dfrac{\sqrt{3}}{2} & \dfrac{\sqrt{2}}{2} \end{bmatrix} \tag{2.18}$$

Convert the stationary coordinate to the synchronous rotating coordinate, i.e. Park transformation, and according to the coordinate transformation relationship in Figure 2.3, the following relationship can be obtained:

$$\begin{bmatrix} f_d & f_q \end{bmatrix}^{\mathrm{T}} = \boldsymbol{T}_{2s/2r} \begin{bmatrix} f_\alpha & f_\beta \end{bmatrix}^{\mathrm{T}} \tag{2.19}$$

Where $\boldsymbol{T}_{2s/2r}$ is the coordinate transformation matrix, expressed as

$$\boldsymbol{T}_{2s/2r} = \begin{bmatrix} \cos\theta_e & \sin\theta_e \\ -\sin\theta_e & \cos\theta_e \end{bmatrix} \tag{2.20}$$

Convert the synchronous rotation coordinate to the stationary coordinate system, i.e.

inverse Park transformation, which is expressed as

$$\begin{bmatrix} f_\alpha & f_\beta \end{bmatrix}^{\mathrm{T}} = \boldsymbol{T}_{2\mathrm{r}/2\mathrm{s}} \begin{bmatrix} f_d & f_q \end{bmatrix}^{\mathrm{T}} \tag{2.21}$$

Where $\boldsymbol{T}_{2\mathrm{r}/2\mathrm{s}}$ is the coordinate transformation matrix, expressed as

$$\boldsymbol{T}_{2\mathrm{r}/2\mathrm{s}} = \boldsymbol{T}_{2\mathrm{s}/2\mathrm{r}}^{-1} = \begin{bmatrix} \cos\theta_e & -\sin\theta_e \\ \sin\theta_e & \cos\theta_e \end{bmatrix} \tag{2.22}$$

Convert the natural coordinate to the synchronous rotation coordinate, i.e. inverse Park transformation, which is expressed as

$$\begin{bmatrix} f_d & f_q & f_0 \end{bmatrix}^{\mathrm{T}} = \boldsymbol{T}_{3\mathrm{s}/2\mathrm{r}} \begin{bmatrix} f_A & f_B & f_C \end{bmatrix}^{\mathrm{T}} \tag{2.23}$$

Where $\boldsymbol{T}_{3\mathrm{s}/2\mathrm{r}}$ is the coordinate transformation matrix, expressed as

$$\boldsymbol{T}_{3\mathrm{s}/2\mathrm{r}} = \boldsymbol{T}_{3\mathrm{s}/2\mathrm{s}} \cdot \boldsymbol{T}_{2\mathrm{s}/2\mathrm{r}} = \frac{2}{3} \begin{bmatrix} \cos\theta_e & \cos\left(\theta_e - \frac{2\pi}{3}\right) & \cos\left(\theta_e + \frac{2\pi}{3}\right) \\ -\sin\theta_e & -\sin\left(\theta_e - \frac{2\pi}{3}\right) & -\sin\left(\theta_e + \frac{2\pi}{3}\right) \\ \frac{1}{2} & \frac{1}{2} & \frac{1}{2} \end{bmatrix} \tag{2.24}$$

Convert the synchronous rotation coordinate to the natural coordinate, which is expressed as

$$\begin{bmatrix} f_A & f_B & f_C \end{bmatrix}^{\mathrm{T}} = \boldsymbol{T}_{2\mathrm{r}/3\mathrm{s}} \begin{bmatrix} f_d & f_q & f_0 \end{bmatrix}^{\mathrm{T}} \tag{2.25}$$

Where $\boldsymbol{T}_{2\mathrm{r}/3\mathrm{s}}$ is the coordinate transformation matrix, expressed as

$$\boldsymbol{T}_{2\mathrm{r}/3\mathrm{s}} = \boldsymbol{T}_{3\mathrm{s}/2\mathrm{r}}^{-1} = \begin{bmatrix} \cos\theta_e & -\sin\theta_e & \frac{1}{2} \\ \cos\left(\theta_e - \frac{2\pi}{3}\right) & -\sin\left(\theta_e - \frac{2\pi}{3}\right) & \frac{1}{2} \\ \cos\left(\theta_e + \frac{2\pi}{3}\right) & -\sin\left(\theta_e + \frac{2\pi}{3}\right) & \frac{1}{2} \end{bmatrix} \tag{2.26}$$

Under the synchronous rotation coordinate, equations of stator voltage and flux linkage are expressed as

$$\begin{cases} u_d = \dfrac{\mathrm{d}\psi_d}{\mathrm{d}t} + Ri_d - \omega_e\psi_q \\ u_q = \dfrac{\mathrm{d}\psi_q}{\mathrm{d}t} + Ri_q + \omega_e\psi_d \end{cases} \tag{2.27}$$

$$\begin{cases} \psi_d = L_d i_d + \psi_f \\ \psi_q = L_q i_q \end{cases} \tag{2.28}$$

Combine (2.27) and (2.28), stator voltage equations are derived as follows

$$\begin{cases} u_d = L_d \dfrac{di_d}{dt} + Ri_d - \omega_e L_q i_q \\ u_q = L_q \dfrac{di_q}{dt} + Ri_q + \omega_e \left(L_d i_d + \psi_f \right) \end{cases} \tag{2.29}$$

And then the equation of the electromagnetic torque is transformed as

$$T_e = \frac{3}{2} p_n i_q \left[i_d \left(L_d - L_q \right) + \psi_f \right] \tag{2.30}$$

In addition, there are still equations expressing the motion states of the PMSM as follows:

$$\begin{cases} \omega_e = n_p \omega_m \\ n_r = \dfrac{30}{\pi} \omega_m \\ \theta_e = \int \omega_e dt \end{cases} \tag{2.31}$$

Where ω_m (rad/s) is rotor mechanical angular velocity, n_r (r/min) is motor speed.

2.2.3 Modelling of the Torsional Damper

The torsional damper is one of the main elastic parts of the drivetrain, for the conventional vehicle with engine and a clutch, the clutch and drive shaft (include wheels) are main elastic components [111]. According to the derivation of dynamic equations of the conventional vehicle powertrain, input and output of all subsystems of the EV powertrain are illustrated as in Figure 2.4.
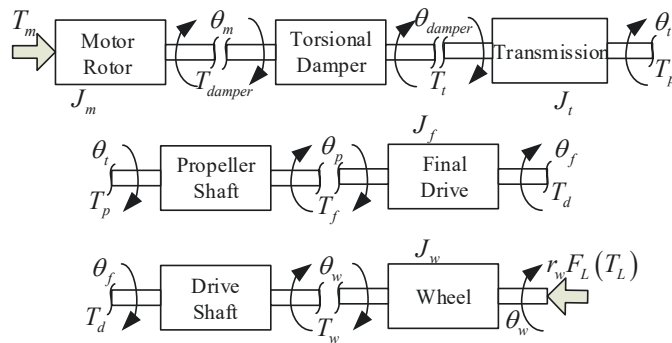
Figure 2.4 Input and Output of Subsystems of EV Powertrain

Considering the working condition of electric vehicle in urban is not quite complicated, stiffness and damping of the equipped damper are set to linear, and then the dynamic equation of the torsional damper is established as

$$T_{damper} = T_t = k_{damper}\left(\theta_m - \theta_{damper}\right) + d_{damper}\left(\dot{\theta}_m - \dot{\theta}_{damper}\right) \tag{2.32}$$

Where k_{damper} and d_{damper} stiffness and damping of the torsional damper, respectively. Therefore, substitute it into Equation (2.14) and then equation of motor rotational motion can be obtained

$$J_m\ddot{\theta}_m = T_e - T_{fric} - \left[k_{damper}\left(\theta_m - \theta_{damper}\right) + d_{damper}\left(\dot{\theta}_m - \dot{\theta}_{damper}\right)\right] \tag{2.33}$$

2.2.4 Modelling of Transmission

Angle relationship and dynamic equation of transmission input shaft and output shaft can be expressed as

$$\theta_{damper} = \theta_t i_t \tag{2.34}$$

$$J_t\ddot{\theta}_t = T_t i_t - d_t\dot{\theta}_t - T_p \tag{2.35}$$

Where i_t is the ratio of the meshed gears, d_t is torsional friction coefficient. Combine with the torsional damper model, Equation (2.35) can be transformed into:

$$J_t\ddot{\theta}_t = i_t\left[k_{damper}\left(\theta_m - \theta_t i_t\right) + d_{damper}\left(\dot{\theta}_m - \dot{\theta}_t i_t\right)\right] - d_t\dot{\theta}_t - T_p \tag{2.36}$$

And Equation (2.33) can be transformed into:

$$J_m\ddot{\theta}_m = T_e - T_{fric} - \left[k_{damper}\left(\theta_m - \theta_t i_t\right) + d_{damper}\left(\dot{\theta}_m - \dot{\theta}_t i_t\right)\right] \tag{2.37}$$

2.2.5 Modelling of Propeller Shaft

The propeller shaft connects transmission output shaft and final drive input shaft, it is regarded as rigid with neglecting friction, relationship in motion is obtained as follows:

$$T_p = T_f, \theta_t = \theta_p \tag{2.38}$$

2.2.6 Modelling of Final Drive

Similar to the transmission and considering friction damping d_f, dynamic equations of the final drive can be expressed as

$$\theta_p = \theta_f i_f \tag{2.39}$$

$$J_f \ddot{\theta}_f = T_f i_f - d_f \dot{\theta}_f - T_d \tag{2.40}$$

Where i_f is the transmission ratio, combine with the propeller model Equation (2.40) can be transformed as

$$J_f \ddot{\theta}_t = T_p i_f^2 - d_f \dot{\theta}_t - T_d i_f \tag{2.41}$$

Combine the above equation and Equation (2.36), dynamic equation of the drivetrain including transmission, propeller shaft and final drive is obtained as:

$$\left(J_t + \frac{J_f}{i_f^2} \right) \ddot{\theta}_t = i_t \left[k_{damper} \left(\theta_m - \theta_t i_t \right) + d_{damper} \left(\dot{\theta}_m - \dot{\theta}_t i_t \right) \right] - \left(d_t + \frac{d_f}{i_f^2} \right) - \frac{T_d}{i_f} \tag{2.42}$$

2.2.7 Modelling of Drive Shaft

The drive shaft is considered as a compliant mechanism, combine with the propeller shaft model and the final drive shaft model, dynamic equation of the drive shaft is obtained as:

$$T_w = T_d = k_d \left(\theta_f - \theta_w \right) + d_d \left(\dot{\theta}_f - \dot{\theta}_w \right) = k_d \left(\frac{\theta_t}{i_f} - \theta_w \right) + d_d \left(\frac{\dot{\theta}_t}{i_f} - \dot{\theta}_w \right) \tag{2.43}$$

Where the stiffness of the drive shaft is k_d, the damping is d_d.

2.2.8 Modelling of Wheel and Vehicle body

Figure 2.5 shows longitudinal forces of vehicle, equation of vehicle longitudinal motion based on Newton's second law is as follows

$$F_L = F_R + F_a + F_{wind} + F_i \tag{2.44}$$
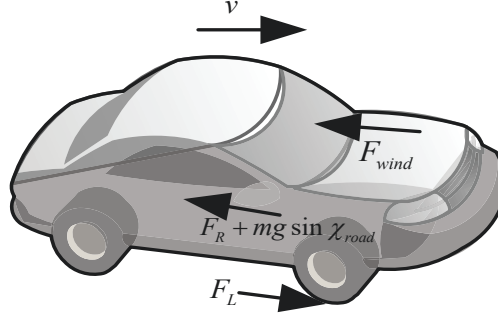
Figure 2.5 Sketch of Vehicle Longitudinal Forces

Where F_L is the adhesion, F_R is the rolling resistance, F_a is the acceleration resistance, F_{wind} is the air resistance, F_i is the slop resistance. Each of them is expressed as follows:

$$
\begin{aligned}
F_R &= m\left(c_{r1} + c_{r2}v\right) \\
F_a &= m\dot{v} \\
F_{wind} &= \frac{1}{2}c_{air}A_L\rho_a v^2 \\
F_i &= mg\sin\chi_{road}
\end{aligned}
\tag{2.45}
$$

Where $v = r_w\dot{\theta}_w$, r_w is wheel radius, c_{r1}, c_{r2} relate to the tire model and tire pressure, c_{air} is air resistance coefficient, A_L is windward area, ρ_a is air density, m is vehicle mass, χ_{road} is road slope. According to the longitudinal force characteristics of vehicle, and ignore the frictional resistance torque, the following dynamic equation can be transformed:

$$
\left(J_w + mr_w^2\right)\ddot{\theta}_w^2 = T_w - \frac{1}{2}c_{air}A_L\rho_a r_w^3\dot{\theta}_w^2 - r_w m\left(c_{r1} + c_{r2}r_w\dot{\theta}_w\right) - r_w mg\sin\chi_{road} \tag{2.46}
$$

Combine the Equation (2.46), Equation (2.43) and Equation (2.42), dynamic equation of the wheel can be obtained as

$$
\begin{aligned}
\left(J_w + mr_w^2\right)\ddot{\theta}_w^2 &= k_d\left(\frac{\theta_t}{i_f} - \theta_w\right) + d_d\left(\frac{\dot{\theta}_t}{i_f} - \dot{\theta}_w\right) - \left(d_w + mc_{r2}r_w^2\right)\dot{\theta}_w \\
&\quad - \frac{1}{2}c_{air}A_L\rho_a r_w^3\dot{\theta}_w^2 - r_w m\left(c_{r1} + g\sin\chi_{road}\right)
\end{aligned}
\tag{2.47}
$$

Since the moment of inertia of the torsional damper is much smaller than that of the rotor, the input/output shaft of the transmission, and the equivalent of the vehicle body, the

elastic torsional damper and elastic drive shaft can be regarded as a system of spring-damping in series, and then obtain a total equivalent stiffness and damping of the drive shaft [111,131], the equivalent stiffness and damping of the drive shaft is expressed as

$$k = \frac{k_{damper} i_t^2 i_f^2 k_d}{k_{damper} i_t^2 i_f^2 + k_d} \tag{2.48}$$

$$d = \frac{d_{damper} i_t^2 i_f^2 d_d}{d_{damper} i_t^2 i_f^2 + d_d} \tag{2.49}$$

For the drivetrain model for control algorithms in the following parts of this thesis, in order to reduce requirement of computing power, the drivetrain model is simplified with the above equivalent stiffness and damping. Therefore, the torsional damper model can be approximated to $\theta_m = \theta_{damper}$ in the equivalent model, and then the Equations (2.33), (2.42), and (2.47) can be transformed to the final drive shaft model [132,133] as:

$$\left(J_m + \frac{J_t}{i_t^2} + \frac{J_f}{i_t^2 i_f^2}\right)\ddot{\theta}_m = T_m - T_{fric} - \left(\frac{d_t}{i_t^2} + \frac{d_f}{i_t^2 i_f^2}\right)\dot{\theta}_m - \frac{k}{i_t i_f}\left(\frac{\theta_m}{i_t i_f} - \theta_w\right) - \frac{d}{i_t i_f}\left(\frac{\dot{\theta}_m}{i_t i_f} - \dot{\theta}_w\right) \tag{2.50}$$

$$\left(J_w + m r_w^2\right)\ddot{\theta}_w^2 = k\left(\frac{\theta_m}{i_t i_f} - \theta_w\right) + d\left(\frac{\dot{\theta}_m}{i_t i_f} - \dot{\theta}_w\right) - \left(d_w + m c_{r2} r_w^2\right)\dot{\theta}_w$$

$$- \frac{1}{2} c_{air} A_L \rho_a r_w^3 \dot{\theta}_w^2 - r_w m\left(c_{r1} + g \sin \chi_{road}\right) \tag{2.51}$$

2.3 Analysis of Drivetrain Torsional Vibration Characteristics

The electric drivetrain is a typical rotational multi-body dynamic model, which includes elastic and damping components and constitutes a second-order system. Because PMSM responds the operation command rapidly, it will output step torque to the drivetrain so that oscillations will come about in the drivetrain, and further it transforms longitudinal shuffle. Since human body is more sensitive to longitudinal (x) shuffle than vertical (z), it is expected to change the natural frequency to avoid resonance by tuning parameters of stiffness and damping, and also attenuate the formant.

Therefore, in this part attenuation of the torsional vibration after introducing the damper

is analyzed and discussed. In calculating of the natural frequency and mode shape of the drivetrain, the drivetrain can be regarded as the multi-body system as shown in Figure 2.6. Because of the existence of the transmission ratio, the bodies at speeds different from the motor speed should be converted into moment of inertia that at the identical speed to the motor. Parameters of the system are shown in Table 2.1.
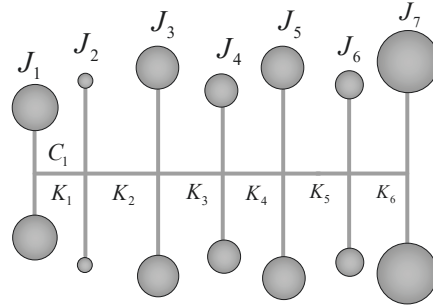
Figure 2.6 Torsional Vibration Mechanics Model of the Electric Drivetrain

Table 2.1 Parameters of the Torsional Vibration Mechanics Model

Moment of Inertia	Component	$0.01 kgm^2$	Stiffness	Component	kgm/rad
J_1	Motor Rotor	6	K_1	Motor to Damper	800
J_2	Torsional Damper	0.8	K_2	Input Shaft of Transmission	8500
J_3	Input Shaft of Transmission	2	K_3	Meshed Gears	4000
J_4	Meshed Gears	4	K_4	Propeller Shaft	9400
J_5	Output Shaft of Transmission	5	K_5	Differential, Drive Shaft	5900
J_6	Differential, Drive Shaft	0.12	K_6	Wheel to Vehicle Body	260
J_7	Wheels, Equivalent Vehicle Body	65	-	-	-

Where the moment of inertia J_7 that equivalent to vehicle translational mass m is derived from the conversion formula as follows

$$J_7 = \frac{mr_w^2}{i_t^2 i_f^2} \tag{2.52}$$

Similarly, torsional stiffness K of each component should also be converted into equivalent stiffness K' based on the principle of conservation of elastic potential energy, such that conversion formulas of K_5 and K_6 in Table 2.1 are as follows

$$K_5 = \frac{K_5'}{i_t^2 i_f^2}, \quad K_6 = \frac{K_6'}{i_t^2 i_f^2} \tag{2.53}$$

According to the torsional vibration mechanics model of the EV drivetrain, the dynamic equations are established as

$$\begin{cases} J_1\ddot{\theta}_1 + K_1(\theta_1 - \theta_2) + C_1(\dot{\theta}_1 - \dot{\theta}_2) = T_e \\ J_2\ddot{\theta}_2 - K_1(\theta_1 - \theta_2) + K_2(\theta_2 - \theta_3) - C_1(\dot{\theta}_1 - \dot{\theta}_2) + C_2(\dot{\theta}_2 - \dot{\theta}_3) = 0 \\ J_3\ddot{\theta}_3 - K_2(\theta_2 - \theta_3) + K_3(\theta_3 - \theta_4) - C_2(\dot{\theta}_2 - \dot{\theta}_3) + C_3(\dot{\theta}_3 - \dot{\theta}_4) = 0 \\ J_4\ddot{\theta}_4 - K_3(\theta_3 - \theta_4) + K_4(\theta_4 - \theta_5) - C_3(\dot{\theta}_3 - \dot{\theta}_4) + C_4(\dot{\theta}_4 - \dot{\theta}_5) = 0 \\ J_5\ddot{\theta}_5 - K_4(\theta_4 - \theta_5) + K_5(\theta_5 - \theta_6) - C_4(\dot{\theta}_4 - \dot{\theta}_5) + C_5(\dot{\theta}_5 - \dot{\theta}_6) = 0 \\ J_6\ddot{\theta}_6 - K_5(\theta_5 - \theta_6) + K_6(\theta_6 - \theta_7) - C_5(\dot{\theta}_5 - \dot{\theta}_6) + C_6(\dot{\theta}_6 - \dot{\theta}_7) = 0 \\ J_7\ddot{\theta}_7 - K_6(\theta_6 - \theta_7) - C_6(\dot{\theta}_6 - \dot{\theta}_7) = 0 \end{cases} \tag{2.54}$$

The above equations can be transformed into standard dynamic equation expressed in matrices, i.e.

$$\boldsymbol{J}\ddot{\boldsymbol{\theta}} + \boldsymbol{C}\dot{\boldsymbol{\theta}} + \boldsymbol{K}\boldsymbol{\theta} = \boldsymbol{T} \tag{2.55}$$

Where the moment of inertia matrix $\boldsymbol{J}$, damping matrix $\boldsymbol{C}$, stiffness matrix $\boldsymbol{K}$, angular displacement vector $\boldsymbol{\theta}$, excitation vector $\boldsymbol{T}$ are expressed in Appendix A.

If not consider external excitations and set the damping matrix $\boldsymbol{C}$ to 0, the following homogeneous equation of undamped free vibration can be obtained:

$$\boldsymbol{J}\ddot{\boldsymbol{\theta}} + \boldsymbol{K}\boldsymbol{\theta} = 0 \tag{2.56}$$

Of which general solution is $\boldsymbol{\theta} = \boldsymbol{\theta_m}\sin(\omega t + \phi)$, with amplitude θ_m, angular frequency ω, phase ϕ, $\boldsymbol{\theta_m} = \begin{bmatrix} \theta_1 & \theta_2 & \theta_3 & \theta_4 & \theta_5 & \theta_6 & \theta_7 \end{bmatrix}^T$. Substitute the general solution in the Equation (2.56), and therefore,

$$\left(K - \omega^2 J\right)\theta_m = 0 \tag{2.57}$$

And the characteristic equation corresponding to the above equation with non-zero is

$$\left|K - \omega^2 J\right| = 0 \tag{2.58}$$

The obtained eigenvalues ω are the inherent angular frequency of the torsional vibration system, and the characteristic vector is the vibration shape corresponding to the inherent angular frequency.

Take Laplace transform of the Equation (2.55), i.e.

$$\left[Js^2 + Cs + K\right]\Theta(s) = T(s) \tag{2.59}$$

And the corresponding transfer function matrix:

$$G(s) = \frac{\Theta(s)}{T(s)} = \left[Js^2 + Cs + K\right]^{-1} \tag{2.60}$$

Substitute $j\omega$ for s in the above transfer function, frequency response function matrix of the vibration system corresponding to the EV drivetrain is

$$H(j\omega) = \left[K - J\omega^2 + j\omega C\right]^{-1} \tag{2.61}$$

Where $H(j\omega) = \left[H_{11}(j\omega) \quad H_{21}(j\omega)\cdots H_{71}(j\omega)\right]^{\text{T}}$, represents frequency response functions of components in Table 2.1 to motor excitation.

Table B1 in Appendix B illustrates contrast of vibration shapes of the EV drivetrain with and without torsional damper. As there is no damper in the rigid connection one, freedom degree is 6, the body 2 corresponds to the body 3 in the system with damper, and so on. From the vibration shapes it can be seen that when motor output shaft and transmission input shaft is connected rigidly, resonance amplitude of the body corresponding to vehicle body is the largest, that means during vehicle runs in low speed, i.e. PMSM works near the first-order modal frequency, longitudinal shuffle of vehicle body will come about, that is what should be attenuated.

The model applied in this thesis is equipped a torsional damper as a simple and passive approach to improve drivability, it performs well in low frequency with no computing

power consumption. Furthermore, by selecting appropriate parameters of the damper, inherent resonance frequency can be changed to avoid frequency range more sensitive to human body in longitudinal direction [134]. Figure 2.7 illustrates frequency response characteristics $H(j\omega)$ of vehicle body to motor excitation, it reveals response of vehicle body to motor excitation under consecutive modal frequencies. It can be seen that formant of vehicle body is attenuated in large scale under low-frequency excitation after equipped a torsional damper. Therefore, it is reasonable to introduce a torsional damper based on the elastic logistics vehicle as the model to research in the following chapters.
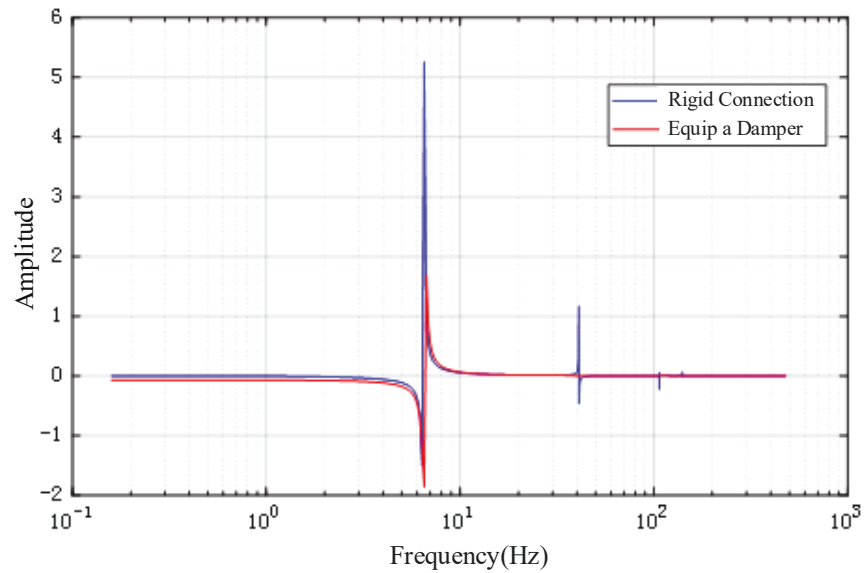
Figure 2.7 Frequency Response of Vehicle Body to Motor Excitation

2.4 Summary

In this chapter an electric vehicle powertrain model based on the electric logistics vehicle with 2-speed AMT is established mathematically, which provides the base of the proposed control algorithms. By analysis of vehicle body frequency response to motor excitation it is revealed that the first order resonance comes about under excitation from motor in low frequency and it is close to the range sensitive to human in longitudinal direction. The resonance can be attenuated by equipping a torsional damper as a passive method to improve drivability.

CHAPTER 3: INTELLIGENT PARAMETER ESTIMATION FOR VEHICLE MASS BASED ON PARTICLE FILTER

3.1 Introduction

Active damping control of torsional vibration for electric drive drivetrain usually requires parameters and motion states in real-time, but some of them are difficult or impossible to be measured. Therefore, observer is required to get the unknown parameters or states based on the known parameters and states, and the estimation of the parameters is also the base and premise of states observation and active damping control.

Vehicle mass is always indispensable in designing and developing of the vehicle system controller, however, vehicle varies with passengers and influences controller output and vibrational characteristics a lot because of the large magnitude.

Table 3.1 Scope of Several Filtering Algorithms Applications

State Equation Observation Equation	Linear, Gauss	Nonlinear, Gauss	Linear, Non-Gauss	Nonlinear, Non-Gauss
Linear, Gauss	KF	EKF/UKF/PF	PF	PF
Nonlinear, Gauss	EKF/UKF/PF	EKF/UKF/PF	PF	PF
Linear, Non-Gauss,	PF	PF	PF	PF
Nonlinear, Non-Gauss	PF	PF	PF	PF

In this chapter intelligent nonlinear Particle Filter (PF) parameter estimation for vehicle mass is proposed, which is an intelligent nonlinear, non-Gauss filter and totally break limitations of Kalman filtering framework as compared in Table 3.1, there are no requirements and restrictions on the process noise, measurement noise and uncertainty [135]. Particle filter is a kind of sequential Monte Carlo sampling-based Bayesian filtering, by predicting and updating sampling from the probability distribution of the system so that expectation of the parameters to be estimated is revealed approximately [136,137].

3.2 Bayesian Estimation Theory

To a kind of nonlinear system described with the following state equation and observation equation:

$$X_t = f(X_{t-1}, W_{t-1}) \tag{3.1}$$

$$Y_t = h(X_t, V_t) \tag{3.2}$$

Where f and h are nonlinear functions, W_t and V_t are process noise and observation noise, respectively, and they are independent of each other. According to Bayesian estimation theory, state estimation is deducing the state X_i, i.e. $p(X_t | Y_{1:t})$ at time t from the observed information $Y_{1:t} = \{y_1, y_2 \cdots y_t\}$. Assume that the initial value of the state variable probability density function $p(X_0)$ is known as a priori information, $X_{1:t}$ and $Y_{1:t-1}$ are independent of each other, Y_t at time t is independent of the previous value under the given $X_{1:t}$, then $p(X_t | Y_{1:t})$ can be derived by the following processes.

Predicting Equation:

$$\begin{aligned}
p(X_t | Y_{1:t-1}) &= \int p(X_t, X_{t-1} | Y_{t-1}) \mathrm{d}X_{t-1} \\
&= \int p(X_t | X_{t-1}) p(X_{t-1} | Y_{1:t-1}) \mathrm{d}X_{t-1}
\end{aligned} \tag{3.3}$$

Update equation:

$$\begin{aligned}
p(X_t | Y_{1:t}) = p(X_t | Y_t, Y_{1:t-1}) &= \frac{p(Y_t | X_t, Y_{1:t-1}) p(X_t | Y_{1:t-1})}{p(Y_t | Y_{1:t-1})} \\
&= \frac{p(Y_t | X_t) p(X_t | Y_{1:t-1})}{p(Y_t | Y_{1:t-1})}
\end{aligned} \tag{3.4}$$

Where $p(X_t | X_{t-1})$ is defined by motion equation, $p(Y_t | X_t)$ is defined by observation equation, $p(Y_t | Y_{1:t-1})$ is normalized constant which as expressed as

$$p(Y_t | Y_{1:t-1}) = \int p(Y_t | X_t) p(X_t | Y_{1:t-1}) \mathrm{d}X_t \tag{3.5}$$

And then optimal estimation and estimation variance can be derived under minimum mean square error, i.e.

$$\hat{X}_t = \int X_t p(X_t \mid Y_{1:t}) \mathrm{d}X_t \tag{3.6}$$

$$S_{XX^{\mathrm{T}}} = E\left[(X_t - \hat{X}_t)(X_t - \hat{X}_t)^{\mathrm{T}}\right] = \int (X_t - \hat{X}_t)(X_t - \hat{X}_t)^{\mathrm{T}} p(X_t \mid Y_{1:t}) \mathrm{d}X_t \tag{3.7}$$

3.3 Nonlinear Particle Filter Algorithm

3.3.1 Monte Carlo Integration

Integral calculation is required in solving the Equations (3.3) and (3.4), but integral calculation for high-dimensional vectors is quite difficult, under the Kalman framework the system must be restricted as linear, Gauss distributed noise so that analytical solutions can be obtained, otherwise only numerical methods can be used to obtain approximate solutions. However, to the nonlinear and non-Gauss systems, Monte Carlo method is very effective to solve the high dimensional integral problems. Suppose that N sample values $\left\{X_{0:t}^{(i)}\right\}_{i=1}^{N}$ are drawn independently from the posterior probability distribution $p(X_{0:t} \mid Y_{1:t})$ of the state, the posterior probability distribution of the state can be expressed as a summation form according to the Monte Carlo method, which is expressed as:

$$\hat{p}(X_{0:t} \mid Y_{1:t}) = \frac{1}{N} \sum_{i=1}^{N} \delta_{X_{0:t}}^{(i)} \mathrm{d}X_{0:t} \tag{3.8}$$

Where $\delta(\bullet)$ is the Dirac Delta function. For the expectation of the state sequence function $g(X_{0:t})$

$$E\left[g(X_{0:t})\right] = \int g(X_{0:t}) p(X_{0:t} \mid Y_{1:t}) \mathrm{d}X_{0:t} \tag{3.9}$$

can be approximated by the following summation form:

$$\overline{E\left[g(X_{0:t})\right]} = \frac{1}{N} \sum_{i=1}^{N} g\left(X_{0:t}^{(i)}\right) \tag{3.10}$$

At this time, these samples need to be assumed to be independent. According to the law of large numbers, $\overline{E\left[g(X_{0:t})\right]}$ converges to $E\left[g(X_{0:t})\right]$ if $N \to \infty$; and assume $\mathrm{var}\left[g(X_{0:t})\right] < \infty$, according to the central limit theorem, when $N \to \infty$, the following relationship is revealed:

$$\sqrt{N}E\left[g\left(X_{0:t}\right)\right] - E\left[g\left(X_{0:k}\right)\right] \rightarrow N\left[0, \text{var}\left(g\left(X_{0:k}\right)\right)\right] \quad (3.11)$$

In the particle filter algorithm, the Monte Carlo method is introduced to take a set of random sample particles, and by adjusting the weights of the set of sample particles to obtain the desired information for operation.

3.3.2 Bayesian Importance Sampling

As pointed out in 3.3.1, the posterior probability distribution can be approximated from a set of discrete samples, according to the law of large numbers, expectation $E\left[g\left(X_{0:k}\right)\right]$ can be approximated by $\overline{E\left[g\left(X_{0:k}\right)\right]}$ as long as the amount of sample particles N is large enough. However, $p\left(X_{0:t} \mid Y_{1:t}\right)$ is usually multivariate and non-standard, it is difficult to draw samples directly.

The commonly used solution of this problem is introducing a reference distribution which is a known reference probability distribution $q\left(X_{0:t} \mid Y_{1:t}\right)$ and easy to sample. Based on this probability distribution it can be obtained that

$$
\begin{aligned}
E\left[g\left(X_{0:t}\right)\right] &= \int g\left(X_{0:t}\right) \frac{p\left(X_{0:t} \mid Y_{1:t}\right)}{q\left(X_{0:t} \mid Y_{1:t}\right)} q\left(X_{0:t} \mid Y_{1:t}\right) \mathrm{d}X_{0:t} \\
&= \int g\left(X_{0:t}\right) \frac{p\left(Y_{1:t} \mid X_{0:t}\right) p\left(X_{0:t}\right)}{p\left(Y_{1:t}\right) q\left(X_{0:t} \mid Y_{1:t}\right)} q\left(X_{0:t} \mid Y_{1:t}\right) \mathrm{d}X_{0:t} \quad (3.12) \\
&= \int g\left(X_{0:t}\right) \frac{\omega_t\left(X_{0:t}\right)}{p\left(Y_{1:t}\right)} q\left(X_{0:t} \mid Y_{1:t}\right) \mathrm{d}X_{0:t}
\end{aligned}
$$

Where $\omega_t\left(X_{0:t}\right)$ is unnormalized importance weight expressed as

$$\omega_t\left(X_{0:t}\right) = \frac{p\left(Y_{1:t} \mid X_{0:t}\right) p\left(X_{0:t}\right)}{q\left(X_{0:t} \mid Y_{1:t}\right)} \quad (3.13)$$

Transform the Equation (3.12) into

$$
\begin{aligned}
E\left[g\left(X_{0:t}\right)\right] &= \frac{1}{p\left(Y_{1:t}\right)} \int g\left(X_{0:t}\right) \omega_t\left(X_{0:t}\right) q\left(X_{0:t} \mid y_{1:t}\right) \mathrm{d}X_{0:t} \\
&= \frac{\int g\left(X_{0:t}\right) \omega_t\left(X_{0:t}\right) q\left(X_{0:t} \mid y_{1:t}\right) \mathrm{d}X_{0:t}}{\int p\left(Y_{1:t} \mid X_{0:t}\right) p\left(X_{0:t}\right) \dfrac{q\left(X_{0:t} \mid Y_{1:t}\right)}{q\left(X_{0:t} \mid Y_{1:t}\right)} \mathrm{d}X_{0:t}} \\
&= \frac{\int g\left(X_{0:t}\right) \omega_t\left(X_{0:t}\right) q\left(X_{0:t} \mid y_{1:t}\right) \mathrm{d}X_{0:t}}{\int \omega_t\left(X_{0:t}\right) q\left(X_{0:t} \mid Y_{1:t}\right) \mathrm{d}X_{0:t}} \\
&= \frac{E_{q\left(\bullet \mid Y_{1:t}\right)}\left[\omega_t\left(X_{0:t}\right) g\left(X_{0:t}\right)\right]}{E_{q\left(\bullet \mid Y_{1:t}\right)}\left[\omega_t\left(X_{0:t}\right)\right]}
\end{aligned}
\tag{3.14}
$$

Where $E_{q\left(\bullet \mid Y_{1:t}\right)}$ indicates expectation under the known probability distribution $q\left(X_{0:t} \mid Y_{1:t}\right)$, from which samples $\left\{X_{0:t}^{(i)}\right\}_{i=1}^{N}$ are obtained, then the expectation can be expressed as

$$
\overline{E\left[g\left(X_{0:t}\right)\right]} = \frac{\dfrac{1}{N}\sum_{i=1}^{N} g\left(X_{0:t}^{(i)}\right) \omega_t\left(X_{0:t}^{(i)}\right)}{\dfrac{1}{N}\sum_{i=1}^{N} \omega_t\left(X_{0:t}^{(i)}\right)} = \sum_{i=1}^{N} g\left(X_{0:t}^{(i)}\right) \tilde{\omega}_t\left(X_{0:t}^{(i)}\right)
\tag{3.15}
$$

Where $X_{0:t}^{(i)}$ is the sample from the distribution $q\left(X_{0:t} \mid Y_{1:t}\right)$, $\tilde{\omega}_t^{i} = \tilde{\omega}_t\left(X_{0:t}^{(i)}\right)$ is the normalized importance weight which expressed as

$$
\tilde{\omega}_t^{(i)} = \frac{\omega_t^{(i)}}{\sum_{j=1}^{N} \omega_t^{(j)}}
\tag{3.16}
$$

3.3.3 Sequence Importance Sampling Based on Markov Process

Because Bayesian importance sampling requires the whole information of $Y_{1:t}$ for estimation of $p\left(X_{0:t} \mid Y_{1:t}\right)$, and the importance weight of state sequence should be recalculated after observation information is updated each time, so the number of calculation increases with time. By introducing the Sequence Importance Sampling (SIS) recursive importance weight can be constructed at time t+1 without changing previous state sequence. The introduced probability distribution can be transformed into:

$$
q\left(X_{0:t} \mid Y_{1:t}\right) = q\left(X_0\right) \prod_{j=1}^{t} q\left(X_j \mid Y_{0:j-1}, Y_{1:j}\right)
\tag{3.17}
$$

Assume that the system states conform to the Markov process, all observed samples are independent of each other, therefore,

$$p\left(X_{0:t}\right) = p\left(X_0\right)\prod_{j=1}^{t}p\left(X_j \mid X_{j-1}\right) \tag{3.18}$$

$$p\left(Y_{1:t} \mid X_{0:t}\right) = \prod_{j=1}^{t}p\left(Y_j \mid X_j\right) \tag{3.19}$$

Then the sample set $\left\{X_{0:t-1}^{(i)}\right\}_{i=1}^{N}$ from the probability distribution $q\left(X_{0:t-1} \mid Y_{1:t-1}\right)$ and the sample particle $X_t^{(i)}$ from $q\left(X_t \mid X_{0:t-1}, Y_{1:t}\right)$ can constitute a new sample set $\left\{X_{0:t}^{(i)}\right\}_{i=1}^{N}$. Substitute the Equations (3.19) (3.18) and (3.17) into the Equation (3.13), recursive weight formula is obtained:

$$
\begin{aligned}
\omega_t &= \frac{p\left(Y_{1:t} \mid X_{0:t}\right)p\left(X_{0:t}\right)}{q\left(Y_{1:t} \mid X_{0:t}\right)} \\
&= \frac{p\left(Y_{1:t} \mid X_{0:t}\right)p\left(X_{0:t}\right)}{q\left(X_t \mid X_{0:t-1}, Y_{1:t}\right)q\left(X_{0:t-1} \mid Y_{1:t-1}\right)} \\
&= \omega_{t-1}\frac{p\left(Y_{1:t} \mid X_{0:t}\right)}{p\left(Y_{1:t-1} \mid X_{0:t-1}\right)}\frac{p\left(X_{0:t}\right)}{p\left(X_{0:t-1}\right)}\frac{1}{q\left(X_t \mid X_{0:t-1}, Y_{1:t}\right)} \\
&= \omega_{t-1}\frac{p\left(Y_t \mid X_t\right)p\left(X_t \mid X_{t-1}\right)}{q\left(X_t \mid X_{0:t-1}, Y_{1:t}\right)}
\end{aligned}
\tag{3.20}
$$
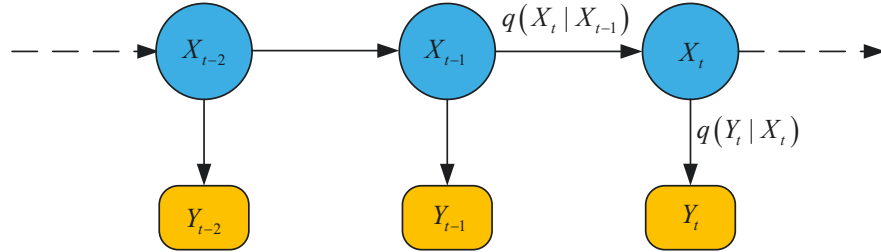
Figure 3.1 Model of the State Space

If the estimation of system states is optimal, $q\left(X_t \mid X_{0:t-1}, Y_{1:t}\right) = p\left(X_t \mid X_{t-1}, Y_t\right)$, because probability distribution q only depends on the X_{t-1} and Y_t in previous moment as illustrated in Figure 3.1. But the real distribution $p\left(X_t \mid X_{t-1}, Y_t\right)$ is usually impossible to be known, therefore, the suboptimal estimation $q\left(X_t \mid X_{0:t-1}, Y_{1:t}\right) = p\left(X_t \mid X_{t-1}\right)$ which can be

achieved easily is applied in common, then the Equation (3.20) can be transformed into

$$\omega_t = \omega_{t-1} p\left(Y_t \mid X_t\right) \qquad (3.21)$$

3.3.4 Particle Resampling

In order to avoid degeneracy problem caused by importance weight concentrating on a few particles after several generations, an effective approach is resampling, i.e. increase the number of particles with larger weights and eliminate particles with smaller weights as illustrated in Figure 3.2. Before the resampling, the set of sample particle and corresponding weight is $\left\{X_t^{(i)}, \omega_t^{(i)}\right\}_{i=1}^{N}$, and it becomes $\left\{X_t^{(i)}, \dfrac{1}{N}\right\}_{i=1}^{N}$ after resampling. Area of each circle in Figure 3.2 represents the weight of different particles. For a certain particle, weight is $\omega_t^{(i)}$ before resampling and it will be divided into many particles after resampling, the small ones are eliminated. Amount of the particles keeps constant in the whole process of resampling and all particles are set to the same weight 1/N after the process.
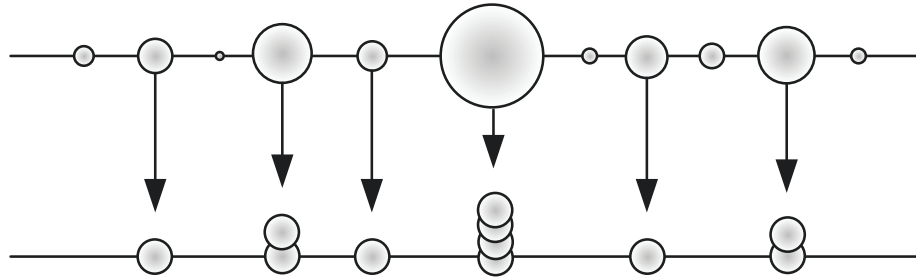
Figure 3.2 Principle of Resampling

The realization of resampling is similar to the "Roulette" as shown in Figure 3.3, use the generated random numbers to draw particles, the more weight the particle has, the more likely it will be drawn, after N rounds a new generation of particles with the amount of N is obtained, and then set weights of all the particles 1/N, this is so-called systematic resampling.
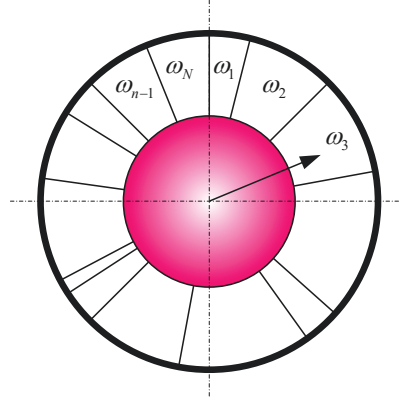
Figure 3.3 Roulette Principle of resampling

The specific of the systematic resampling process is as follows:

(1) Divide the interval (0,1] into N continuous complementary intervals, i.e.

$$(0,1] = (0, \frac{1}{N}] \cup (\frac{1}{N}, \frac{2}{N}] \cup \cdots (\frac{N-1}{N}, 1]$$

(2) Generate a set of random numbers, $u_i = \dfrac{(i-1)+\mu}{N}, \mu \sim U[0,1], i = 1, 2, \cdots N$, where

$U[a,b]$ represents uniform distribution over each interval [a, b].

(3) If the random number i u_i meets requirements of $\sum\limits_{j=1}^{m-1} \omega_t^{(j)} < u_i \sum\limits_{j=1}^{m} \omega_t^{(j)}, i = 1, 2, \cdots, N$,

then replicate the mth particle $X_t^{(m)}$, i.e. $\hat{X}_t^{(i)} = X_t^{(m)}$.

(4) Initialize the weight $\omega_t^{(j)} = 1/N$, then the new particle set $\left\{ \hat{X}_t^{(i)} \mid i = 1, 2, \cdots, N \right\}$ is

obtained.

The principle of particle filter sampling can be summarized as the following steps and illustrated as in Figure 3.4:

(1) Draw N random samples $\left\{ X_{t-1}^{(i)} \right\}_{i=1}^{N}$ from the reference probability distribution $q(X)$

and set weight of each particle to 1/N.

(2) Calculate importance weight of each sample $X_t^{(i)}$ and make $\omega_t^{(i)} \propto \dfrac{p(X_t)}{q(X_t)}$.

(3) Initialize the importance weight, i.e. $\tilde{\omega}_t\left(X_{0:t}^{(i)}\right) = \dfrac{\omega_t\left(X_{0:t}^{(i)}\right)}{\displaystyle\sum_{i=1}^{N}\omega_t\left(X_{0:t}^{(i)}\right)}$

(4) Resample the discrete set $\left\{X_{t-1}^{(i)}\right\}_{i=1}^{N}$ for N times, and make the probability of each particle $X_t^{(i)}$ being resampled to be proportional to its weight $\tilde{\omega}_t^{(i)}$.

Figure 3.4 Process of Particle Filter

3.3.5 General Algorithmic Flow of Particle Filter

General algorithmic flow of particle filter can be summarized as follows [138].

(1) Initialization, t=0

For i=1:N, Draw the initial $X_0^{(i)}$ from the prior probability distribution $P(X_0)$.

(2) For t=1:T

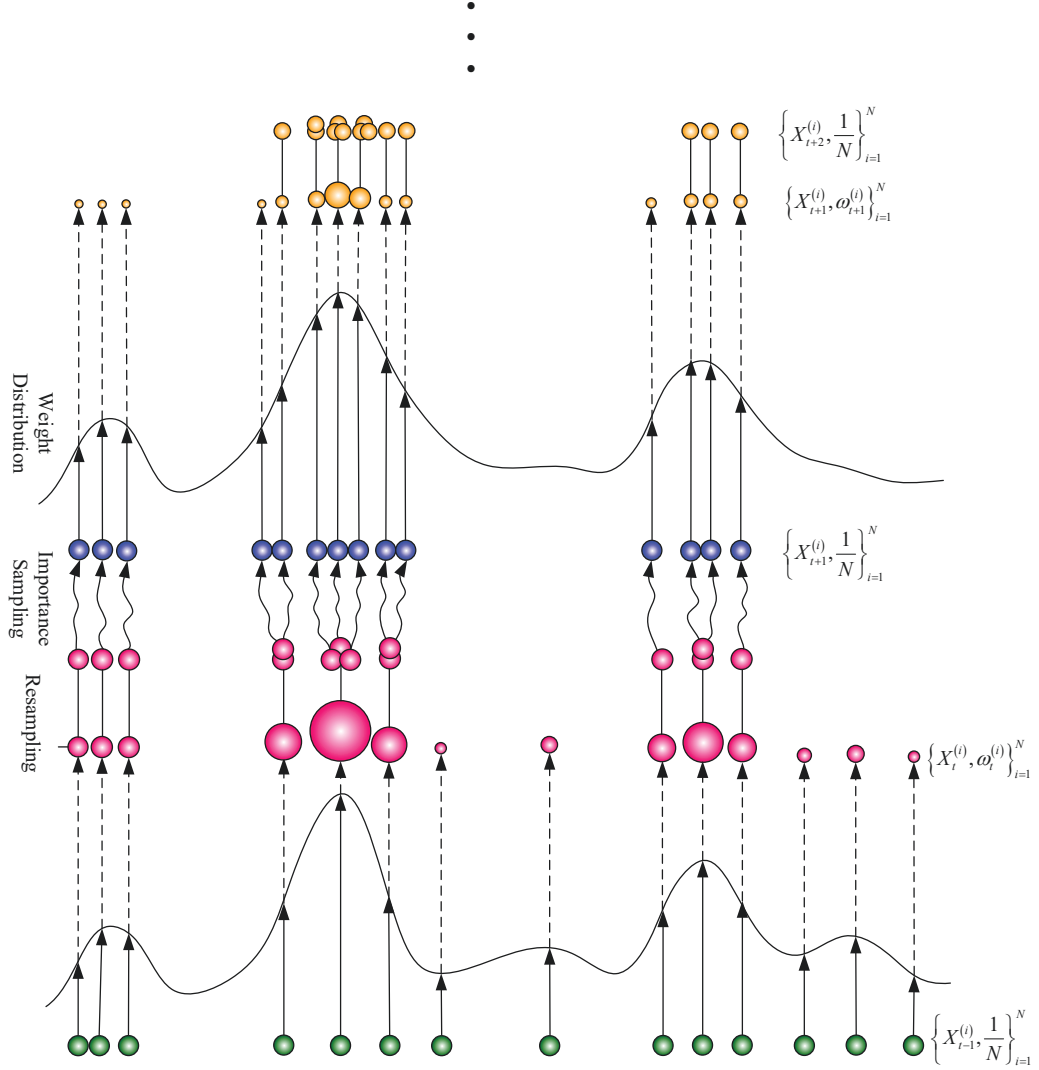   (i)   Importance Sampling:

        For i=1:N, draw $\hat{X}_t^{(i)} \sim q\left(X_t \mid X_{0:t-1}^{(i)}, Y_{1:t}\right)$, and set $\hat{X}_{0:t}^{(i)} = \left(X_{0:t}^{(i)}, \hat{X}_t^{(i)}\right)$.

        For i=1:N, recalculate weight for each particle:

$$\omega_t^{(i)} = \omega_{t-1}^{(i)} p\left(Y_t \mid X_{t-1}^{(i)}\right) = \omega_{t-1}^{(i)} \frac{p\left(Y_t \mid X_t^{(i)}\right) p\left(X_t^{(i)} \mid X_{t-1}^{(i)}\right)}{q\left(X_t^{(i)} \mid X_{t-1}^{(i)}, Y_{1:t}\right)}$$

        For i=1:N, normalize the weight:

$$\tilde{\omega}_t\left(X_{0:t}^{(i)}\right) = \frac{\omega_t\left(X_{0:t}^{(i)}\right)}{\sum\limits_{i=1}^{N} \omega_t\left(X_{0:t}^{(i)}\right)}$$

    (ii)   Resampling

        Generate N samples randomly from the distribution $p\left(X_{0:t}^{(i)} \mid Y_{1:t}\right)$ and calculate the weights, replicate or eliminate the particles $\hat{X}_{0:t}^{(i)}$ according to the normalized weights $\tilde{\omega}_t\left(X_{0:t}^{(i)}\right)$.

        For i=1:N, reset the weight and assign them uniformly $\omega_t^{(i)} = \tilde{\omega}_t^{(i)} = \frac{1}{N}$.

    (iii)   Output

        The output of particle filter algorithm is a set of sample points which can be approximately expressed as a posterior distribution as

$$p\left(X_{0:t} \mid Y_{1:t}\right) \approx \hat{p}\left(X_{0:t} \mid Y_{1:t}\right) = \frac{1}{N} \sum_{i=1}^{N} \delta_{\left(X_{0:t}^{(i)}\right)} dX_{0:t}$$

(3) End

3.4 Particle Filter- Based Nonlinear Vehicle Mass Estimation

3.4.1 Discretization of Nonlinear Continuous Systems

In this thesis Euler method is applied to realize discretization of nonlinear continuous systems. Euler method is widely used in engineering practice because of the simple form,

less calculation and easy implementation. Although accuracy of Euler method is quite high, it can be improved by shortening the step size. For the first order system:

$$\begin{cases} \dfrac{dx}{dt} = f(t,x) \\ x(t_0) = x_0 \end{cases} \tag{3.22}$$

Where the function $f(t,x)$ of x meets requirements of Lipschitz. From the initial moment t_0 on, in the time domain there exist $t_1=t_0+h$, $t_2=t_1+h$, $\cdots$, $t_{n+1}=t_n+h$, h is the step. Suppose that x is infinitely differentiable at t, then Taylor series for $x(t)$ near t_n can be expanded as

$$\begin{aligned} x(t_{n+1}) &= x(t_n) + h\dot{x}(t_n) + \frac{h^2}{2!}\ddot{x}(t_n) + \cdots + \frac{h^k}{k!}x^{(k)}(t_n) + \cdots \\ &= x(t_n) + hf(t_n, x(t_n)) + \frac{h^2}{2!}\ddot{x}(t_n) + \cdots \end{aligned} \tag{3.23}$$

Take the linear part of h, and use x_n to approximate $x(t_n)$, then formula of Euler approximation can be expressed as

$$x_{n+1} = x_n + hf(t_n, x_n) \tag{3.24}$$

Of which truncation error is $R_n = \dfrac{h^2}{2!}\ddot{x}(t_n) + \cdots + \dfrac{h^k}{k!}x^{(k)}(t_n) + \cdots$.
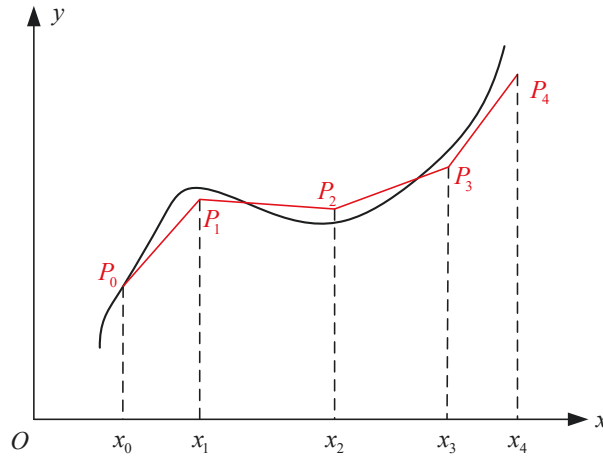

Figure 3.5 Principle of Euler Discretization

Geometric meaning of the Euler method is shown in Figure 3.5, from the point P₀ draw a straight line with slope $f(x_0, y_0)$ and intersects $x = x_1$ at the point $P_1(x_1, y_1)$, use the

ordinate y_1 of point P$_1$ to approximate $y(x_1)$; from the point P$_1$ draw a straight line with slope $f(x_1, y_1)$ and intersects $x = x_2$ at the point $P_2(x_2, y_2)$, and so on. Therefore, the polyline $P_0 P_1 P_2 P_3 P_4 \cdots$ is the discrete approximation of $y = y(x)$.

3.4.2 Estimation of Vehicle Mass

Assumption: Motor equipped in electric vehicle performs well, error of torque output and driver's command can be neglected.

Vehicle mass estimation is based on the discrete vehicle longitudinal dynamic equation after forward Euler approximation. Transform the longitudinal dynamic equation in Chapter 2 into the following form to make it more intuitive:

$$\frac{T_m i_g i_0 \eta}{r_w} = \frac{C_D A_L}{21.15} u_a^2 + mgf \cos \chi_{road} + mg \sin \chi_{road} + \frac{1}{3.6} m \frac{du_a}{dt} \tag{3.25}$$

Where f is the rolling resistance coefficient, for small vehicles it can be derived from the empirical formula in Equation (3.26); C_D is air drag coefficient, A_L is windward area, χ_{road} is road slope, $i_g i_0$ is total gear ratio, r_w is wheel radius, u_a (km/h) is vehicle speed, m is the vehicle mass to be estimated.

$$f = f_0 + f_1 \left(\frac{u_a}{100}\right) + f_2 \left(\frac{u_a}{100}\right)^4 \tag{3.26}$$

In order to estimate the parameter, it is usually regarded as a state of the system as well, but is non-time-variable, i.e. $\dot{m} = 0$. Therefore, the state vector can be selected as $x = \begin{bmatrix} x_1 & x_2 \end{bmatrix}^T = \begin{bmatrix} u_a & m \end{bmatrix}^T$, input signal is selected as $u = T_m$. Then the longitudinal dynamic equation of (3.25) can be transformed into the following equation:

$$\dot{x}_1 = 3.6 \left(-\frac{C_D A_L}{21.15} \frac{1}{x_2} x_1^2 + \frac{i_g i_0 \eta}{r_w} \frac{1}{x_2} u - gf \cos \chi_{road} - g \sin \chi_{road} \right) \tag{3.27}$$

It is a nonlinear continuous system, but parameter estimation depends on a discrete model describing the state progression from the current moment to the next moment, i.e. $x(k+1) = f(x(k), \omega(k), u(k))$, where $x(k)$ is state of the system at a moment, $\omega(k)$ is

process disturbance or uncertainty, $u(k)$ is the input information. According to the forward Euler approximation [139,140], the Equation (3.27) can be transformed into the following discrete state space model:

$$\begin{bmatrix} x_1(k+1) \\ x_2(k+1) \end{bmatrix} = \begin{bmatrix} x_1(k)+3.6T_s\left(-\dfrac{C_D A_L}{21.15}\dfrac{1}{x_2(k)}x_1^2(k)+\dfrac{i_g i_0 \eta}{r_w}\dfrac{1}{x_2(k)}u\right) \\ x_2(k) \end{bmatrix} + \begin{bmatrix} 3.6T_s\left(-gf\cos\chi_{road}-g\sin\chi_{road}\right) \\ 0 \end{bmatrix} \tag{3.28}$$

And the corresponding observation equation is

$$y(k+1)=x_1(k) \tag{3.29}$$

Where T_s is the sample time.

In this research, vehicle mass is estimated mainly aims to load calculation for powertrains, given electric vehicles are usually not driven in terrible road conditions, change of resistance of powertrain mainly comes from vehicle mass variation, variations from rolling resistance and road slope parts $gf\cos\chi_{road}+g\sin\chi_{road}$ can be regarded as uncertainties the process uncertainties $\omega(k)$, if the road slope changes in large scale it can still be converted into equivalent vehicle mass. Furthermore, consider the noise $v(k)$ from measurement state and observation models of the vehicle mass estimator can be obtained as follows:

$$\begin{bmatrix} x_1(k+1) \\ x_2(k+1) \end{bmatrix} = \begin{bmatrix} x_1(k)+3.6T_s\left(-\dfrac{C_D A_L}{21.15}\dfrac{1}{x_2(k)}x_1^2(k)+\dfrac{i_g i_0 \eta}{r_w}\dfrac{1}{x_2(k)}u\right) \\ x_2(k) \end{bmatrix} + \begin{bmatrix} \omega(k) \\ 0 \end{bmatrix} \tag{3.30}$$

$$y(k+1)=x_1(k)+v(k) \tag{3.31}$$

3.5 Simulation of the Vehicle Mass Estimator Performance

The vehicle mass estimator program is triggered at vehicle start-up and acceleration, based on the discrete state equation and corresponding observation equation of the

longitudinal vehicle dynamic equation, and the designed particle filter, model for simulation is established in Matlab as in Figure 3.6, which mainly includes motor output, drive resistance, vehicle longitudinal forces and particle filter. In the simulation some critical parameters are set as in Table 3.2, and operations with several loads are selected in the simulation.
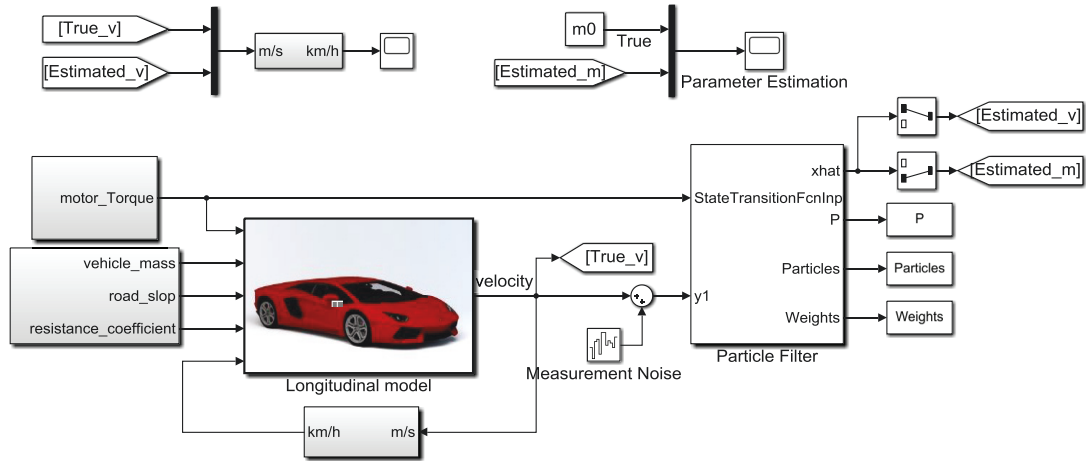
Figure 3.6 Simulation Model for Vehicle Mass Estimation

Table 3.2 Critical parameters in vehicle mass estimation

Vehicle Parameter	Value	Estimator Parameter	Value
Vehicle Mass (empty)	1500kg	Particles Amount	1000
Vehicle Mass (rated)	2500kg	Particles Mean	1500
Total Gear Ratio	20.12	Particles Variance	100000
Wheel Radius	0.309m	Sample Time	500ms

The simulation results demonstrate vehicle speed tracking, mass estimation and 1000 particles distribution with vehicle masses of 1500kg, 1900kg, 2500kg (including a driver). In this part, all groups of test are under the same operation that at start-up time and the motor is ordered to output 80Nm.

Figure 3.7 (a) is tracking performance of the observation signal $y(k)$, i.e. vehicle speed tracking, which serves posterior probability distribution for the particle filter. Figure 3.7 (b) shows performance of vehicle estimation, since the initial particles distribution covers

the real vehicle mass but with a large variance, overshoot appears in the initial stage but it can converge towards real vehicle mass directly and keeps steady soon as the estimation process going on, in Figure 3.8 it concretely reveals 1000 particles distribution and convergence over time.

(a)   (b)
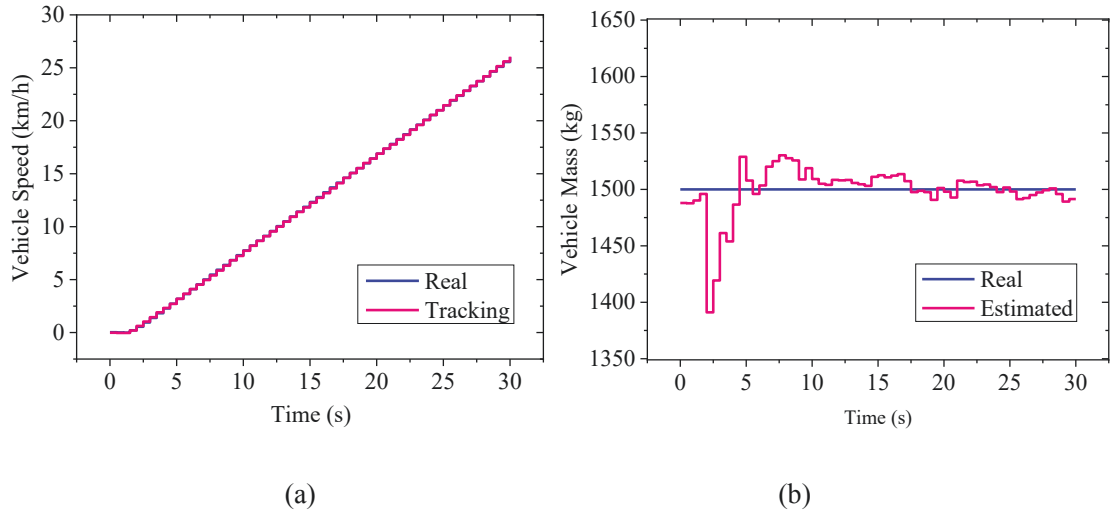
(a) Vehicle Speed Tracking   (b) Vehicle Mass Estimation

Figure 3.7 Vehicle Mass Estimation Performance When $m=1500$kg

Figure 3.8 Particles Distribution in Time Sequence When $m=1500$kg

Within the normal load range (such as $m=1900$kg, $m=2300$kg), the vehicle mass estimator

performs similarly as can be seen in the Figure 3.9~Figure 3.12, the initial particles distribution still covers the real vehicle mass but near to the upper edge of particle distribution, with acceleration of the vehicle, convergence of the estimated mass shows an obvious directivity which converges towards the real vehicle mass without overshoots, after several seconds all particles cluster near the real vehicle mass.

(a) (b)

(a) Vehicle Speed Tracking (b) Vehicle Mass Estimation

Figure 3.9 Vehicle Mass Estimation Performance When $m=1900$kg
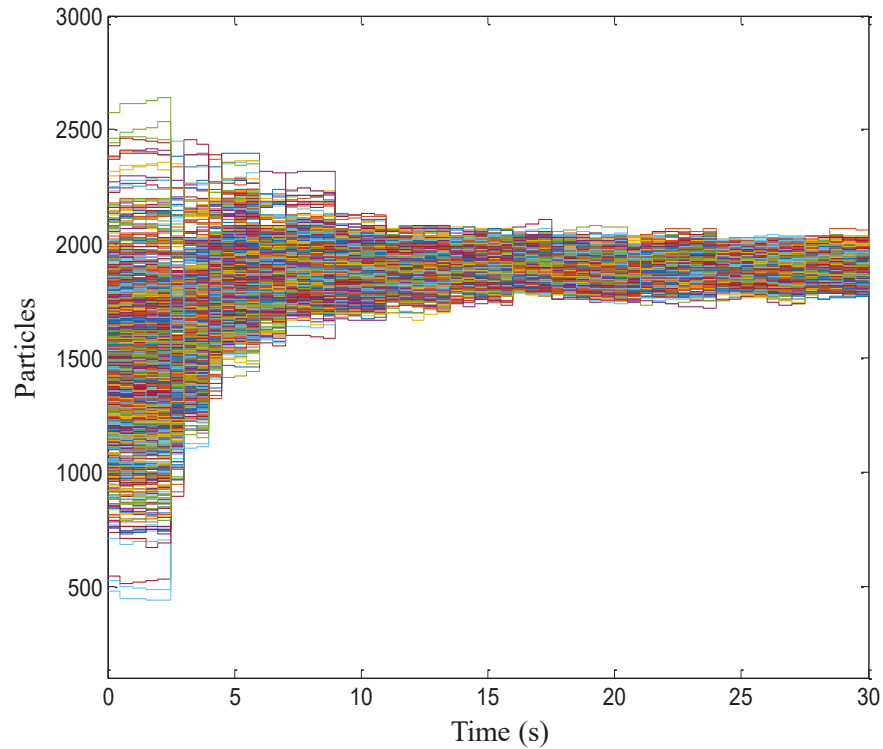
Figure 3.10 Particles Distribution in Time Sequence When $m=1900$kg

(a)

(b)
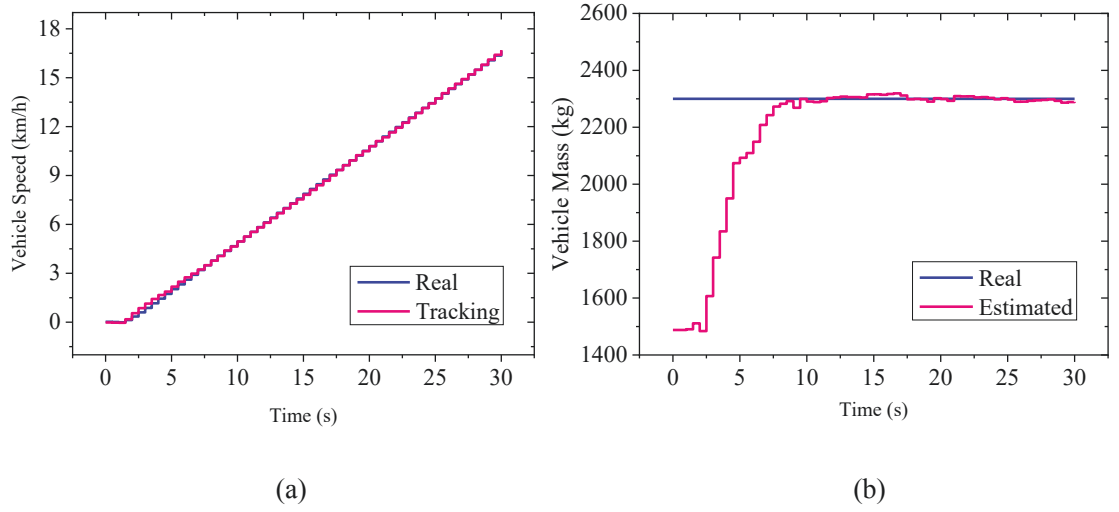
(a) Vehicle Speed Tracking   (b) Vehicle Mass Estimation

Figure 3.11 Vehicle Mass Estimation Performance When *m*=2300kg
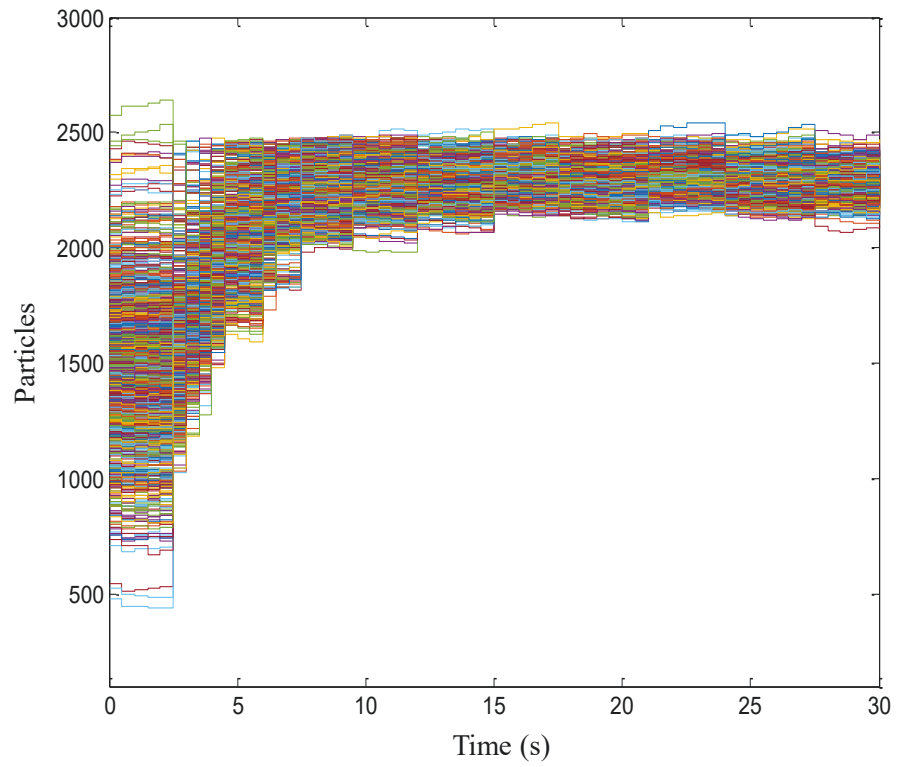
Figure 3.12 Particles Distribution in Time Sequence When *m*=2300kg

When vehicle mass comes to the upper limit as shown in Figure 3.13 and Figure 3.14, performance of the estimator also reaches the maximum under the current amount, mean and variance of particles, and the particles distribution converges to the upper bound at

this moment. Solution to this issue is increasing amount and expand variance of the particles so that the range of the estimator is augmented.
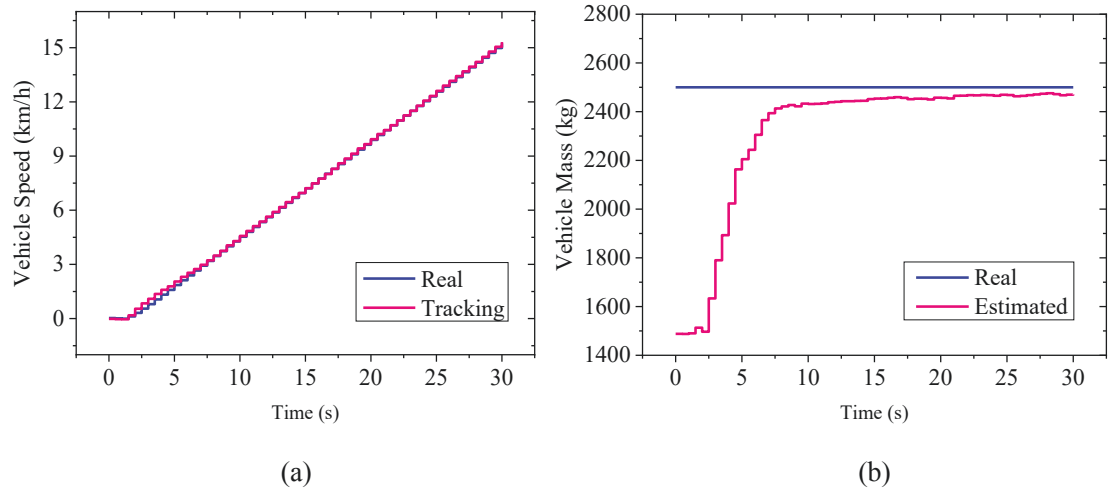
(a) Vehicle Speed Tracking　　(b) Vehicle Mass Estimation

Figure 3.13 Vehicle Mass Estimation Performance When *m*=2500kg

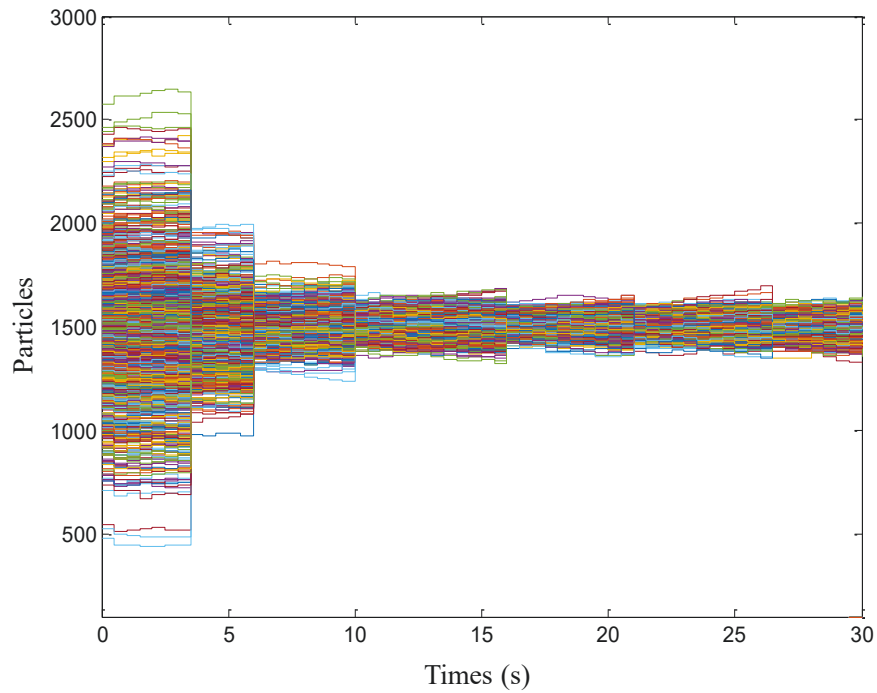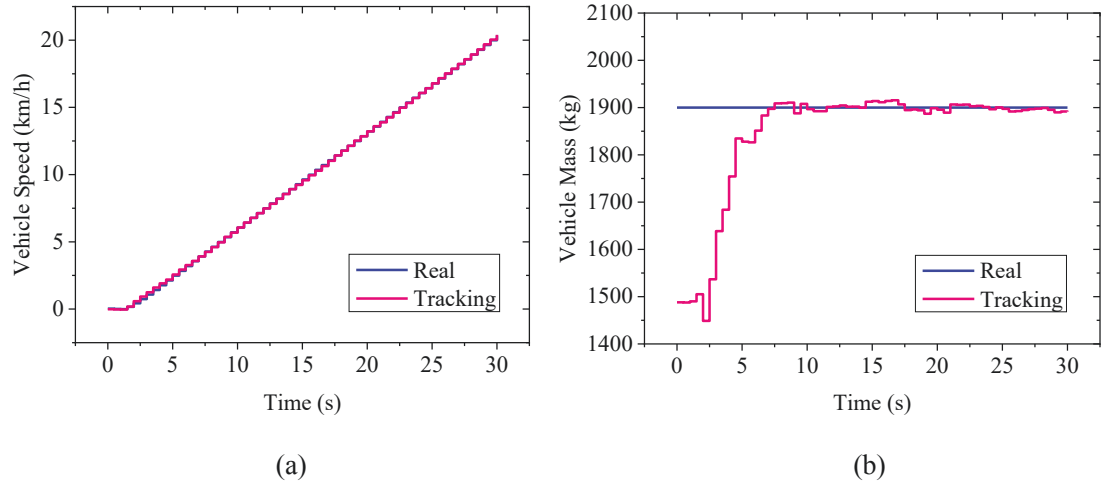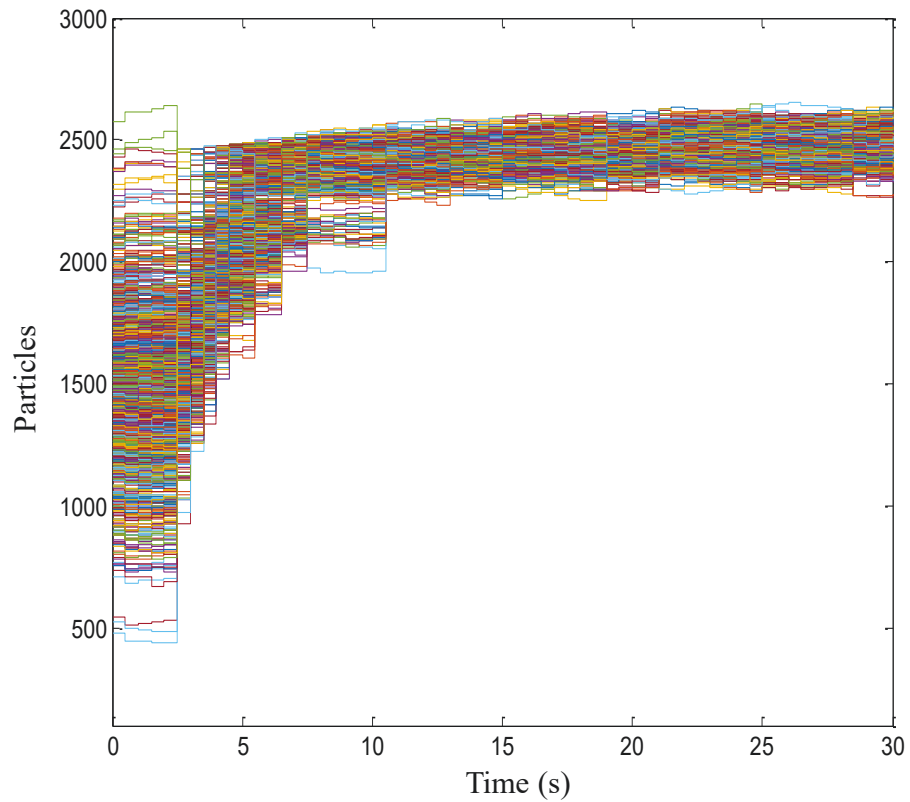Figure 3.14 Particles Distribution in Time Sequence When *m*=2500kg

3.6 Summary

This chapter is aiming to find an intelligent method to estimate vehicle mass without knowing or supposing statistical characteristics of noise and uncertainties in advance, therefore, nonlinear particle filter is introduced. Particle filter is a kind of Bayesian recursive estimator based on Monte Carlo method, it uses the probability distribution of particles and expectations of the samples to approximate the real parameter rather than deriving an analytical solution exactly. Particle filter breaks framework and limitations of Kalman filter so that the system doesn't have to be linear and subject to Gauss distribution, and information on noise or uncertainties is not required.

Based on the discrete vehicle longitudinal vehicle dynamic equation after Euler approximation, state equation and observation equation of vehicle mass estimator are established with vehicle mass constituting the state vector. Performance of the proposed vehicle mass estimator is tested by operation of start-up and acceleration with several masses. From the estimation results and particles distributions, the estimator is demonstrated that the estimation results can converge to the real values effectively.

CHAPTER 4: NOVEL SLIDING MODE OBSERVER FOR MOTION STATE OF ELECTRIC VEHICLE DRIVETRAIN

4.1 Introduction

In dynamic control for vehicle not only system parameters are required, but also various motion states, which are obtained usually and directly is equipping some sensors to offer information to the controller. However, in practical application, it is always limited by cost, space requirement, working condition and even some states are not measurable at all. As the development of control theory and improvement of computing ability of the hardware processor, observers that use the measurable states to estimate the unmeasurable states are introduced by many automotive producers.

In application of vehicle dynamic system, the observer is required to be simple in the formula, fast convergence to real values, accurate in signal tracking and sometimes nonlinear. Compared with methods such as pole placement, least squares, and Kalman filter, sliding mode algorithms is simple in form and suitable for nonlinear systems with less computing consumption, it is one of the ideal choices in vehicle system.

An accelerated second order super twisting sliding mode observer with an adaptive gain is proposed for a typical nonlinear system in this chapter. The key contribution of this algorithm is that the rate of convergence of observation error is accelerated remarkably by introducing "system damping". Chattering issue is attenuated with satisfactory performance compared to conventional sliding mode observer. The novel observer is proven mathematically to be convergent in a finite time. The proposed novel sliding mode observer is applied to observation of the torque in drive shaft so that it can avoid the elastic potential energy accumulated in the elastic driveshaft being released suddenly after shifting, and shock or torsional vibration will be avoided further. Moreover, it also provides indispensable information to the following chapter.

4.2 Accelerated Adaptive Second Order Super Twisting Sliding Mode Observer

4.2.1 Observability Criterion for Nonlinear Systems

Observability is the premise of observation for all systems, observability criteria are given in modern control theory. For the following n-dimensional nonlinear system:

$$\begin{cases} \dot{x}(t) = f\big(x(t), u(t)\big) \\ y(t) = h\big(x(t), u(t)\big) \end{cases} \tag{4.1}$$

Where $x = [x_1, x_2, \cdots, x_n]^{\mathrm{T}}$ is the state vector; $y = [y_1, y_2, \cdots y_m]^{\mathrm{T}}$ is the observer output vector; f is a smooth vector field in space $\mathbb{R}^n$. The Lie derivative of h with respect to f is defined as

$$\mathcal{L}_f h(x, u) = \frac{\partial h(x, u)}{\partial x} f(x, u) \tag{4.2}$$

And corresponding successive derivatives are:

$$\begin{cases} \mathcal{L}_f^0 h = h \\ \mathcal{L}_f^1 h = \dfrac{\partial}{\partial x}\big(\mathcal{L}_f^0 h\big) f \\ \vdots \\ \mathcal{L}_f^i h = \dfrac{\partial}{\partial x}\big(\mathcal{L}_f^{i-1} h\big) f \\ \vdots \end{cases} \tag{4.3}$$

Define the matrix

$$O = \frac{\partial}{\partial x} \begin{bmatrix} \mathcal{L}_f^0 h \\ \mathcal{L}_f^1 h \\ \vdots \\ \mathcal{L}_f^{n-1} h \end{bmatrix}\Bigg|_{x=x_0} = \begin{bmatrix} \dfrac{\partial}{\partial x_1}\mathcal{L}_f^0 h & \dfrac{\partial}{\partial x_2}\mathcal{L}_f^0 h & \cdots & \dfrac{\partial}{\partial x_m}\mathcal{L}_f^0 h \\ \dfrac{\partial}{\partial x_1}\mathcal{L}_f^1 h & \dfrac{\partial}{\partial x_2}\mathcal{L}_f^1 h & \cdots & \dfrac{\partial}{\partial x_m}\mathcal{L}_f^1 h \\ \vdots & \vdots & \ddots & \vdots \\ \dfrac{\partial}{\partial x_1}\mathcal{L}_f^{n-1} h & \dfrac{\partial}{\partial x_2}\mathcal{L}_f^{n-1} h & \cdots & \dfrac{\partial}{\partial x_m}\mathcal{L}_f^{n-1} h \end{bmatrix}_{x=x_0} \tag{4.4}$$

The above equation is the observability matrix, if $\text{Rank}(\boldsymbol{O}) = n$, the system of (4.1) is local observable over a neighborhood of x_0.

4.2.2 Principle of Sliding Mode Variable Structure

Sliding mode control is a variable structure control which is different from other control algorithms because of the discontinuity, a time-varying discontinuous switch function is introduced in the algorithm to make the system to vibrate up and down along the expected state trajectory in high frequency, i.e. sliding mode motion. Such sliding motion can be designed and doesn't relate to the system parameters and disturbance, therefore, the sliding motion state is robust [141].

Generally, in the state space

$$\dot{x} = f(x), x \in \mathbf{R}^n \tag{4.5}$$

There exists a sliding manifold $s(x) = s(x_1, x_2, \cdots x_n) = 0$, divide the space into two sections: $s > 0$ and $s < 0$; the system trajectory has three kinds of motion conditions on the switching surface as shown in Figure 4.1.
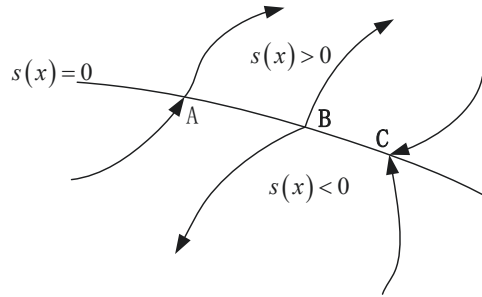
Figure 4.1 Motion of the System Trajectory Along the Sliding Manifold

A is the point where the system trajectory moves to the switching manifold $s(x) = 0$ and passes through; B is the point where the system trajectory moves close to the switching manifold $s(x) = 0$ and leaves to both sides, it is the starting point; C is the point where the system trajectory moves close to the switching manifold $s(x) = 0$ and goes toward to the

sliding manifold from both sides, it is the terminal point. In the sliding mode variable structure, the points of a certain area of the switching manifold are usually the terminal points, and the system trajectory that goes close to the area will be attracted. When the trajectory goes close to the sliding manifold $s(x) = 0$, the following characteristic exists:

$$\lim_{x \to 0} s\dot{s} \le 0 \tag{4.6}$$

The above equation provides a necessary condition of Lyapunov stability in form of $v(x_1, x_2, \cdots, x_n) = \left[s(x_1, x_2, \cdots, x_n) \right]^2$, because it is positive definite but derivate of s^2 according to (4.6) is negative semidefinite, so $v(x)$ is not an increasing function near $s(x)=0$, then the system is stable at $s(x)=0$ as long as (4.6) is meet. Hence, for such systems

$$\dot{x} = f(t, x, u), x \in \mathbf{R}^n, \quad u \in \mathbf{R}^m \tag{4.7}$$

There exists a switch function $s(x)$, by solving the Equation (4.8) the trajectory out of the sliding manifold will converge to the sliding manifold and keep steady in finite time, that is the sliding mode variable structure.

$$u = \begin{cases} u^+(x) & s(x) > 0 \\ u^-(x) & s(x) < 0 \end{cases} \tag{4.8}$$

Where $u^+(x) \ne u^-(x)$.

4.2.3 Accelerated Adaptive Super-Twisting Sliding Mode Observer

For such type of nonlinear systems

$$x^{(n)}(t) = f(t, x, u) + \delta(t, x, u) \tag{4.9}$$

And it can be transformed in the following state equations

$$\begin{cases} \dot{x}_1 = x_2 \\ \dot{x}_2 = x_3 \\ \vdots \\ x_n^{(n)} = f(t, x, u) + \delta(t, x, u) \end{cases} \tag{4.10}$$

The observation vector, real state vector, and observation error vector of the system state are denoted as:

$$\begin{cases} \hat{\pmb{x}} = \begin{bmatrix} \hat{x} & \dot{\hat{x}} & \cdots & \hat{x}^{(n-1)} \end{bmatrix}^{\mathrm{T}} \\ \pmb{x} = \begin{bmatrix} x & \dot{x} & \cdots & x^{(n-1)} \end{bmatrix}^{\mathrm{T}} \\ \tilde{\pmb{x}} = \pmb{x} - \hat{\pmb{x}} = \begin{bmatrix} \tilde{x} & \dot{\tilde{x}} & \cdots & \tilde{x}^{(n-1)} \end{bmatrix}^{\mathrm{T}} \end{cases} \tag{4.11}$$

Divide the state vector into x_1 and x_2 according to whether the state variables can be directly measured by the sensor, then the state equations are degenerated into

$$\begin{cases} \dot{x}_1 = x_2 \\ \dot{x}_2 = f\left(t, x_1, x_2, u\right) + \delta\left(t, x_1, x_2, u\right) \\ y = x_1 \end{cases} \tag{4.12}$$

Where x_1 is the measurable variable, y is the system output, u is the system input, $f\left(t, x_1, x_2, u\right)$ is the model function of the system. $\delta\left(t, x_1, x_2, u\right)$ is the disturbance and uncertainties.

Assumption 1. The system $f\left(t, \mathbf{x}, \mathbf{u}\right)$ in Equation (4.12) is a continuous function that is not known with high accuracy, but its uncertainty $\xi\left(t, \mathbf{x}, \mathbf{u}\right)$ is bounded by Ξ, $\Xi \geq 0$, the uncertain system can be expressed with a model function $\hat{f}\left(t, \mathbf{x}, \mathbf{u}\right)$ so that $f\left(t, \mathbf{x}, \mathbf{u}\right) = \hat{f}\left(t, \mathbf{x}, \mathbf{u}\right) + \xi\left(t, \mathbf{x}, \mathbf{u}\right)$, where $\left|\xi\left(t, \mathbf{x}, \mathbf{u}\right)\right| \leq \Xi$.

Assumption 2. The disturbance δ is bounded, $\left|\delta\right| \leq \Delta$, $\Delta \geq 0$.

Based on the regular sliding mode observer

$$\begin{cases} \dot{\hat{x}}_1 = \hat{x}_2 + k_1 \operatorname{sgn}\left(x_1 - \hat{x}_1\right) \\ \dot{\hat{x}}_2 = \hat{f}\left(t, x_1, \hat{x}_2, u\right) + k_2 \operatorname{sgn}\left(x_1 - \hat{x}_1\right) \end{cases} \tag{4.13}$$

And corresponding observation error

$$\begin{cases} \dot{\tilde{x}}_1 = \tilde{x}_2 - k_1 \operatorname{sgn}\left(\tilde{x}_1\right) \\ \dot{\tilde{x}}_2 = f\left(t, x_1, x_2, u\right) - \hat{f}\left(t, x_1, \hat{x}_2, u\right) + \delta\left(t, x_1, x_2, u\right) - k_2 \operatorname{sgn}\left(\tilde{x}_1\right) \end{cases} \tag{4.14}$$

The Lyapunov function is selected as follows

$$\mathrm{L}\left(\tilde{x}_1\right) = \frac{1}{2}\tilde{x}_1^2 \tag{4.15}$$

Hence, according to the Lyapunov stability criterion:

$$\frac{\mathrm{d}}{\mathrm{d}t}\left(\frac{1}{2}\tilde{x}_1^2\right) = \tilde{x}_1\dot{\tilde{x}}_1 = \tilde{x}_1\left(\tilde{x}_2 - k_1\,\mathrm{sgn}\left(\tilde{x}_1\right)\right) \tag{4.16}$$

If the k_1 is large enough the Equation (4.16) will not be positive so that the state variable $\tilde{x}_1$ is asymptotically stable and $\tilde{x}_1 \approx \dot{\tilde{x}}_1 \approx 0$ at this moment. According to Filippov transformation and introduce $\varepsilon = 0|1$, the Equation (4.14) is equivalent to

$$\begin{cases} \dot{\tilde{x}}_1 = \varepsilon\left(\tilde{x}_2 + k_1\right) + \left(1-\varepsilon\right)\left(\tilde{x}_2 - k_1\right) \\ \dot{\tilde{x}}_2 = \tilde{f} + \delta + \varepsilon k_2 + \left(1-\varepsilon\right)\left(-k_2\right) \end{cases} \tag{4.17}$$

In the neighborhood of the sliding manifold, $\tilde{x}_2$ conform the following relationship:

$$\dot{\tilde{x}}_2 = \tilde{f} + \delta - \frac{k_2}{k_1}\tilde{x}_2 \tag{4.18}$$

By solving the above equation, it can be obtained that

$$\left|\frac{k_2}{k_1}\tilde{x}_2 - \left(\tilde{f} + \delta\right)\right| = e^{-\frac{k_2}{k_1}t} \tag{4.19}$$

Therefore, $\tilde{x}_2$ will converge to $\frac{k_1}{k_2}\left(\tilde{f} + \delta\right)$ as long as $k_1 k_2 > 0$, the $\tilde{x}_2$ is asymptotically stable too. The more precise the observation model function and the less disturbance the system suffers, the more accurate the estimation of the observation state is. The more accurate and less disturbed the observation model function is, the more accurate observation vector x_2 will be.

In order to attenuate the "chattering" problem, high-order sliding mode and adaptive sliding mode gains are introduced to improve the accuracy of the tracking for desired sliding manifold, and the "system damping" is introduced as well to accelerate the convergence of observation trajectory towards sliding mode manifold. Therefore, the proposed Accelerated Adaptive Super-Twisting Sliding Mode Observer (AASTW) is expressed as

$$\begin{cases} \dot{\hat{x}}_1 = \alpha_1\left(x_1 - \hat{x}_1\right) + \hat{x}_2 + k_1\sqrt{\left|x_1 - \hat{x}_1\right|}\,\text{sgn}\left(x_1 - \hat{x}_1\right) \\ \dot{\hat{x}}_2 = \alpha_2\left(x_1 - \hat{x}_1\right) + \hat{f}\left(t, x_1, \hat{x}_2, u\right) + k_2\,\text{sgn}\left(x_1 - \hat{x}_1\right) \end{cases} \tag{4.20}$$

And corresponding observation error equation

$$\begin{cases} \dot{\tilde{x}}_1 = -\alpha_1\tilde{x}_1 + \tilde{x}_2 - k_1\sqrt{\left|\tilde{x}_1\right|}\,\text{sgn}\left(\tilde{x}_1\right) \\ \dot{\tilde{x}}_2 = -\alpha_2\tilde{x}_1 + f\left(t, x_1, x_2, u\right) - \hat{f}\left(t, x_1, \hat{x}_2, u\right) + \delta\left(t, x_1, x_2, u\right) - k_2\,\text{sgn}\left(\tilde{x}_1\right) \end{cases} \tag{4.21}$$

Where $\alpha_{1,2}$ is positive constant value, and $\alpha\tilde{x}$ is the so-called "system damping", the k_1 and

k_2 are adaptive gains defined as

$$\dot{k}_{1,2} = \begin{cases} \lambda_{1,2}\,\text{sgn}\left(\left|x_1 - \hat{x}_1\right| - \mu_{1,2}\right) & k_{1,2} > \kappa_{1,2} \\ 0 & k_{1,2} \leq \kappa_{1,2} \end{cases} \tag{4.22}$$

Where $\lambda_{1,2}$, $\mu_{1,2}$, and κ are constant values, but κ cannot be a small arbitrarily value and it

should be selected according to the limit of $k_{1,2}$ which will be discussed in the following

text. μ in (5) plays a role as a detector, when the estimation error $\tilde{x}_1$ comes through the

limit $\left|\tilde{x}_1\right| \leq \mu$, the adaptive gains will reduce dynamically and start a fine tuning phase, so

that overshoot of the trajectory can be further weakened until it leaves this domain as
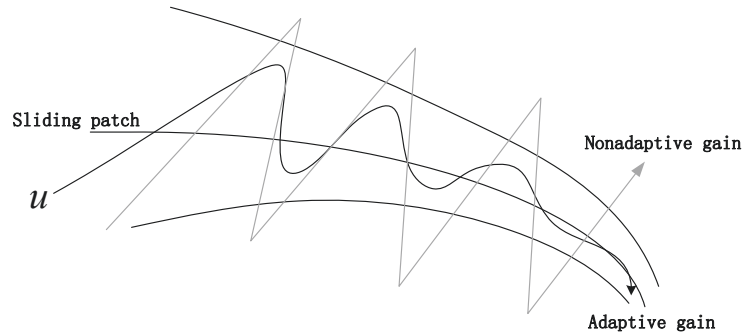
illustrated in Figure 4.2.

Figure 4.2 Sketch Map of Adaptive Gain Effect

Lemma. The adaptive gains k_1 and k_2 in Equation (4.22) are bounded.

Proof. (i) If $k_{1,2}$ comes into the interval $k_{1,2} \leq \kappa_{1,2}$, it is a constant value.

(ii) If $k_{1,2}$ is in the interval $k_{1,2} > \kappa_{1,2}$, integrate both sides of Equation (4.22) and obtain

the solution of the differential equation

$$k_{1,2} = k(t_0) \pm \lambda_{1,2} \cdot t, \quad t \in \left[t_0, t_f \right] \tag{4.23}$$

Therefore, in a finite time domain $k_{1,2}$ is bounded, the Lemma is proven.

Theorem 1. Based on Assumption 1 and Assumption 2, the proposed observer in Equation (4.20) and Equation (4.21) for nonlinear systems in (4.9) can drive the estimation errors $(\tilde{x}_1, \tilde{x}_2) \to (0,0)$ in finite time.

Proof. All kinds of observers are always affected by noise or disturbance in engineering practice, so robustness plays a critical role in the performance of the observer, this proof is based on Davila's proof method [142] and noise or disturbance is taken into consideration. Let $F(x_1, x_2, \hat{x}_2) = f(t, x_1, x_2, u) - \hat{f}(t, x_1, \hat{x}_2, u) + \delta(t, x_1, x_2, u)$. It is bounded according to Assumption 1 and Assumption 2, there exists a constant F_0, $F_0 \geq 0$, such that $|F(x_1, x_2, \hat{x}_2)| \leq F_0$, the Equation (4.21) can be transformed into

$$\begin{cases} \dot{\tilde{x}}_1 = -\alpha_1 \tilde{x}_1 + \tilde{x}_2 - k_1 \sqrt{|\tilde{x}_1|} \, \mathrm{sgn}(\tilde{x}_1) \\ \dot{\tilde{x}}_2 = -\alpha_2 \tilde{x}_1 + F(t, x_1, x_2, \hat{x}_2, u) - k_2 \, \mathrm{sgn}(\tilde{x}_1) \end{cases} \tag{4.24}$$

$k_{1,2}$ is adaptive as shown in (4.22) on the premise that it satisfies the following inequalities.

$$\begin{cases} k_1 > \sqrt{\dfrac{2}{k_2 - F_0}} \dfrac{(k_2 + F_0 + \Lambda)(1+p)}{1-p} \\ k_2 > F_0 \end{cases} \tag{4.25}$$

where p is a constant value, $p \in (0,1)$, $\Lambda \geq \alpha_2 \tilde{x}_{1_{\max}}^2$. Therefore, such relations can be obtained as follows:

$$\begin{cases} \dot{\tilde{x}}_1 = -\alpha_1 \tilde{x}_1 + \tilde{x}_2 - k_1 \sqrt{|\tilde{x}_1|} \, \mathrm{sgn}(\tilde{x}_1) \\ \dot{\tilde{x}}_2 \in [-F_0, F_0] - \alpha_2 \tilde{x}_1 - k_2 \, \mathrm{sgn}(\tilde{x}_1) \end{cases} \tag{4.26}$$

$$\ddot{\tilde{x}}_1 = -\alpha_1 \dot{\tilde{x}}_1 + \dot{\tilde{x}}_2 - \frac{1}{2} k_1 \frac{\dot{\tilde{x}}_1}{\sqrt{|\tilde{x}_1|}} \tag{4.27}$$

and further

$$\ddot{\tilde{x}}_1 \in [-F_0, F_0] - \alpha_2 \tilde{x}_1 - \left(\alpha_1 \dot{\tilde{x}}_1 + \frac{1}{2} k_1 \frac{\dot{\tilde{x}}_1}{\sqrt{|\tilde{x}_1|}} + k_2 \, \mathrm{sgn}(\tilde{x}_1) \right) \tag{4.28}$$
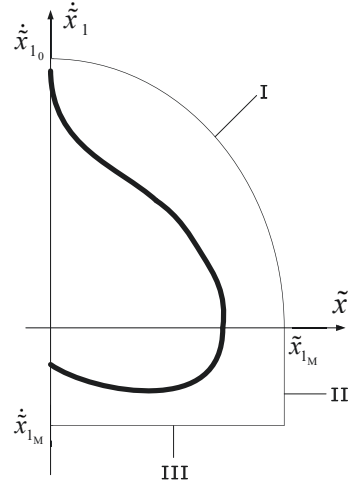

Figure 4.3 Sketch Map of Majorant Trajectory for the Observer

A graph of (4.28) can be drawn partially for the region $\left[0, \tilde{x}_{1_M} \right]$ as in Figure 4.3 shows.

Set the initial conditions, $\tilde{x}_1 = 0$, $x_2 = \dot{\tilde{x}}_1$, $\hat{x}_2 = 0$, thus $\tilde{x}_2 = x_2$.

(1) If the initial value of x_2 is positive, the trajectory will enter into right half-plane. Otherwise, it will enter into the left half-plane, and in this article the former condition is discussed. When the trajectory goes in the first quadrant it is confined between $\tilde{x}_1 = 0$, $\dot{\tilde{x}}_1 = 0$ and curve I $\ddot{\tilde{x}}_{1\max} = -(k_2 - F_0)$, let $(x_{1_M}, 0)$ indicate intersection point of $\dot{\tilde{x}}_1 = 0$ and $\ddot{\tilde{x}}_{1\max} = -(k_2 - F_0)$, $\left(0, \dot{\tilde{x}}_{1_0} \right)$ indicate intersection point of $\tilde{x}_1 = 0$ and $\ddot{\tilde{x}}_{1\max} = -(k_2 - F_0)$, it is easy to get $\dot{\tilde{x}}_{1_0}^2 = 2(k_2 - F_0) \tilde{x}_{1_M}$ by integral calculation. Therefore, the following inequality can be seen.

$$\ddot{\tilde{x}}_1 \leq F_0 - \alpha_2 \tilde{x}_1 - k_2 \, \mathrm{sgn}(\tilde{x}_1) - \alpha_1 \dot{\tilde{x}}_1 - \frac{1}{2} k_1 \frac{\dot{\tilde{x}}_1}{\sqrt{|\tilde{x}_1|}} < 0 \tag{4.29}$$

When the trajectory moves towards $\dot{\tilde{x}}_1 = 0$, it can be described by the following equation.

$$\dot{\tilde{x}}_1^2 = 2(k_2 - F_0)\left(\tilde{x}_{1_M} - \tilde{x}_1 \right) \tag{4.30}$$

Then it transits through $\dot{\tilde{x}}_1 = 0$, and enters the forth quadrant and moves towards $\tilde{x}_1 = 0$.

If $\ddot{\tilde{x}}_1 = 0$, $\dot{\tilde{x}}_1$ reaches the minimum value as (4.32) by solving (4.31).

$$\ddot{\tilde{x}}_1 = F(t, x_1, x_2, \hat{x}_2, u) - \alpha_2 \tilde{x}_1 - \left(\alpha_1 \dot{\tilde{x}}_1 + \frac{1}{2} k_1 \frac{\dot{\tilde{x}}_1}{\sqrt{|\tilde{x}_1|}} + k_2 \right) = 0 \tag{4.31}$$

$$
\begin{aligned}
\dot{\tilde{x}}_{1_{\min}} &= \frac{2\sqrt{|\tilde{x}_1|}}{2\alpha_1\sqrt{|\tilde{x}_1|} + k_1} \left[F(t, x_1, x_2, \hat{x}_2, u) - k_2 - \alpha_2 \tilde{x}_1 \right] \\
&> -\frac{2}{k_1} \sqrt{|\tilde{x}_{1_{\mathrm{M}}}|} \left(F_0 + k_2 + \alpha_2 \tilde{x}_{1_{\mathrm{M}}} \right)
\end{aligned}
\tag{4.32}
$$

Therefore, the trajectory in the fourth quadrant is confined between $\tilde{x}_1 = 0$, $\dot{\tilde{x}}_1 = 0$, $\tilde{x}_1 = \tilde{x}_{1_{\mathrm{M}}}$

(line II) and $\dot{\tilde{x}}_1 = -\left(2\tilde{x}_{1_{\mathrm{M}}}^{1/2} / k_1 \right)\left(F_0 + k_2 + \alpha_2 \tilde{x}_{1_{\mathrm{M}}} \right)$ (line III). Given the condition (4.25) and

$\dot{\tilde{x}}_{1_0}^2 = 2(k_2 - F_0) \tilde{x}_{1_{\mathrm{M}}}$, it is easy to derive the conclusion as follows.

$$\frac{|\dot{\tilde{x}}_{1_{\mathrm{M}}}|}{|\dot{\tilde{x}}_{1_0}|} < \frac{2}{k_1}\sqrt{\tilde{x}_{1_{\mathrm{M}}}} \frac{F_0 + k_2 + \alpha_2 \tilde{x}_{1_{\mathrm{M}}}}{\sqrt{2(k_2 - F_0)\tilde{x}_{1_{\mathrm{M}}}}} < \frac{(1-p)(F_0 + k_2 + \alpha_2 \tilde{x}_{1_{\mathrm{M}}})}{(1+p)(k_2 + F_0 + \Lambda)} \le \frac{1-p}{1+p} < 1 \tag{4.33}$$

It can be observed that the point of intersection between the trajectory and $\tilde{x}_1 = 0$ is getting

closer and closer to $\tilde{x}_1 = \dot{\tilde{x}}_1 = \tilde{x}_2 = 0$.

(2) If the initial value of x_2 is negative, the trajectory will enter into left half-plane and

move as mirror of the right half plane. Equation (4.33) is also established, the proof is left

out here.

The above process can ensure the observation states $(\tilde{x}_1, \dot{\tilde{x}}_1)$ converge to $\tilde{x}_1 = \dot{\tilde{x}}_1 = 0$; for $\tilde{x}_2$,

according to the first equation of (4.26) when $\tilde{x}_2 = \dot{\tilde{x}}_1$ there will exist $\tilde{x}_2 = \dot{\tilde{x}}_1$ at any time.

Furthermore, from the second equation of (4.24), it can be obtained that:

$$
\begin{aligned}
\dot{\tilde{x}}_2 &= -\alpha_2 \tilde{x}_1 + F(x_1, x_2, \hat{x}_2) - k_2 \operatorname{sgn}(\tilde{x}_1) \\
&= \begin{cases} -\alpha_2 \tilde{x}_1 + F(x_1, x_2, \hat{x}_2) - k_2 & \tilde{x}_1 > 0 \\ -\alpha_2 \tilde{x}_1 + F(x_1, x_2, \hat{x}_2) + k_2 & \tilde{x}_1 < 0 \end{cases}
\end{aligned}
\tag{4.34}
$$

Therefore,

$$0 < k_2 - F_0 \le |\dot{\tilde{x}}_2| \le k_2 + F_0 \tag{4.35}$$

Let t_i indicate one time interval between successive intersection points of the trajectory

and $\tilde{x}_1 = 0$, integrate (4.35) over a small time interval, thus

$$\int_{t_1}^{t_2} \left|\dot{\tilde{x}}_2\right| dt = \left|\tilde{x}_2\right|_{t=t_1} + \left|\tilde{x}_2\right|_{t=t_2} = \left|\dot{\tilde{x}}_{1_i}\right| + \left|\dot{\tilde{x}}_{1_{i+1}}\right| \geq (k_2 - F_0) t_i \tag{4.36}$$

$$t_i \leq \frac{\left|\dot{\tilde{x}}_{1_i}\right|}{2(k_2 - F_0)} \tag{4.37}$$

and the total convergence time is

$$T = \sum_{i=0}^{\infty} t_i \leq \sum_{i=0}^{\infty} \frac{\left|\dot{\tilde{x}}_{1_i}\right|}{k_2 - F} \tag{4.38}$$

It can be seen that the total convergence time is limited because of the decreasing $\left|\dot{\tilde{x}}_{1_i}\right|$ as derived in previous text, therefore, the observation errors can converge in finite time, theorem 1 is proven.

Theorem 2. The proposed observer is stable.

Proof. Select the Lyapunov function in the Equation (4.15), of which partial derivative is

$$\frac{\partial}{\partial t}\left(\frac{1}{2}\tilde{x}_1^2\right) = e\dot{e} = \tilde{x}_1\dot{\tilde{x}}_1 = \tilde{x}_1\left[-\alpha_1\tilde{x}_1 + \tilde{x}_2 - k_1\sqrt{|\tilde{x}_1|}\,\mathrm{sgn}(\tilde{x}_1)\right] \tag{4.39}$$

$$k_1 > \begin{cases} -\alpha_1\sqrt{|\tilde{x}_1|} + \dfrac{\tilde{x}_2}{\sqrt{|\tilde{x}_1|}} & \tilde{x}_1 < 0 \\[3mm] -\alpha_1\sqrt{|\tilde{x}_1|} - \dfrac{\tilde{x}_2}{\sqrt{|\tilde{x}_1|}} & \tilde{x}_1 < 0 \end{cases} \tag{4.40}$$

$$\lim_{\tilde{x}_1 \to 0, \tilde{x}_2 \to 0} \frac{\tilde{x}_2}{\sqrt{|\tilde{x}_1|}} = 0 \tag{4.41}$$

If k_1 meets the requirement of expressed as (4.40), $L(\tilde{x}_1)\cdot\dot{L}(\tilde{x}_1) < 0$ can be realized and the observer is stable. When the estimation errors $(\tilde{x}_1, \tilde{x}_2)$ reach a small neighborhood of the origin point $(0,0)$ and consider the (4.41) based on the infinitesimals of the same order theorem, $\exists\, k_1 > r$, $r \in \mathbb{R}^+$, it makes $L(\tilde{x}_1)\cdot\dot{L}(\tilde{x}_1) < 0$, theorem 2 is proven.

Remark 4. By introducing the "system damping" $\alpha\tilde{x}$, attraction of error trajectory is enhanced.

Consider the system in (4.21), in the sliding patch $\dot{\tilde{x}}_1 = 0$, there exist relations as follows.

$$\tilde{x}_2 \leq k_1\sqrt{|\tilde{x}_1|} + \alpha_1\tilde{x}_1 \qquad \tilde{x}_1 > 0$$
$$\tilde{x}_2 \geq -k_1\sqrt{|\tilde{x}_1|} + \alpha_1\tilde{x}_1 \qquad \tilde{x}_1 < 0$$

(4.42)

As illustrated in Figure 4.4, by introducing the "system damping" $\alpha_1\tilde{x}_1$, region of direction attraction is extended, so that trajectory is attracted toward $(0,0)$ earlier.
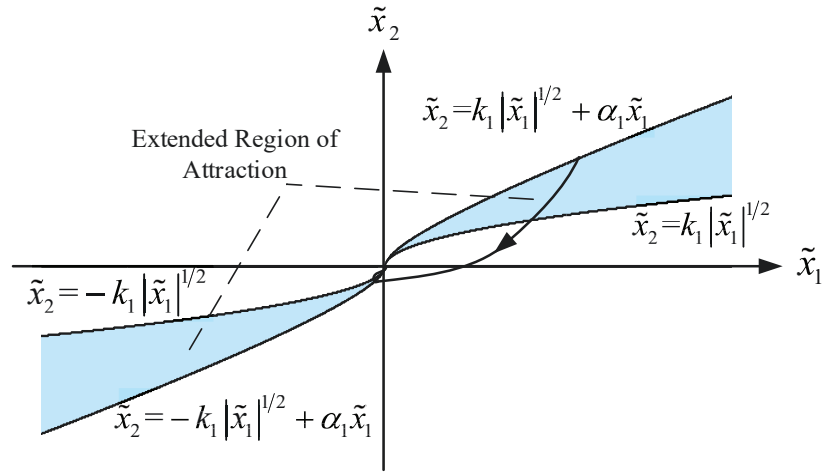

Figure 4.4 Effect of Damping on Reachability

4.2.4 Observer Performance Test

In this section the proposed novel sliding mode observer is tested comparing with several typical sliding mode observers in Table 4.1 in terms of convergence time and chattering conditions. The initial value of $(\tilde{x}_1, \dot{\tilde{x}}_1)$ is supposed to be $(10,10)$, and they are calculated for the same duration with identical sample time 100s.

It can be observed in the following figures, the conventional sliding mode observer in Figure 4.5 takes the longest time to converge the estimation errors to 0 because of the longest spiral trajectory and when the errors are getting close to $(0,0)$ chatter occurs intensely.

Table 4.1 Comparisons of Several Typical Sliding Mode Observers

| SMO Type	Observer Equations	Parameters Setting
SMO	$\begin{cases} \dot{\tilde{x}}_1 = \tilde{x}_2 - k_1 \operatorname{sgn}(\tilde{x}_1) \\ \dot{\tilde{x}}_2 = -k_2 \operatorname{sgn}(\tilde{x}_1) \end{cases}$	$k_1 = 1 \quad k_2 = 1$
STW	$\begin{cases} \dot{\tilde{x}}_1 = \tilde{x}_2 - k_1 \sqrt{|\tilde{x}_1|}\,\operatorname{sgn}(\tilde{x}_1) \\ \dot{\tilde{x}}_2 = -k_2 \operatorname{sgn}(\tilde{x}_1) \end{cases}$	$k_1 = 1 \quad k_2 = 1$
AcSTW	$\begin{cases} \dot{\tilde{x}}_1 = -\alpha_1 \tilde{x}_1 + \tilde{x}_2 - k_1 \sqrt{|\tilde{x}_1|}\,\operatorname{sgn}(\tilde{x}_1) \\ \dot{\tilde{x}}_2 = -\alpha_2 \tilde{x}_1 - k_2 \operatorname{sgn}(\tilde{x}_1) \end{cases}$	$k_1 = 1, k_2 = 1, \alpha_1 = 1, \alpha_2 = 1$
AdSTW	$\begin{cases} \dot{\tilde{x}}_1 = \tilde{x}_2 - k_1(\tilde{x}_1) \sqrt{|\tilde{x}_1|}\,\operatorname{sgn}(\tilde{x}_1) \\ \dot{\tilde{x}}_2 = -k_2(\tilde{x}_1) \operatorname{sgn}(\tilde{x}_1) \end{cases}$	$k_1(\tilde{x}_{10}) = 1, k_2(\tilde{x}_{10}) = 1, \mu_1 = 0.01, \mu_2 = 0.01$
AASTW	$\begin{cases} \dot{\tilde{x}}_1 = -\alpha_1 \tilde{x}_1 + \tilde{x}_2 - k_1(\tilde{x}_1) \sqrt{|\tilde{x}_1|}\,\operatorname{sgn}(\tilde{x}_1) \\ \dot{\tilde{x}}_2 = -\alpha_2 \tilde{x}_1 - k_2(\tilde{x}_1) \operatorname{sgn}(\tilde{x}_1) \end{cases}$	$k_1(\tilde{x}_{10}) = 1, k_2(\tilde{x}_{10}) = 1, \alpha_1 = 1, \alpha_2 = 1$ $\mu_1 = 0.01, \mu_2 = 0.01$
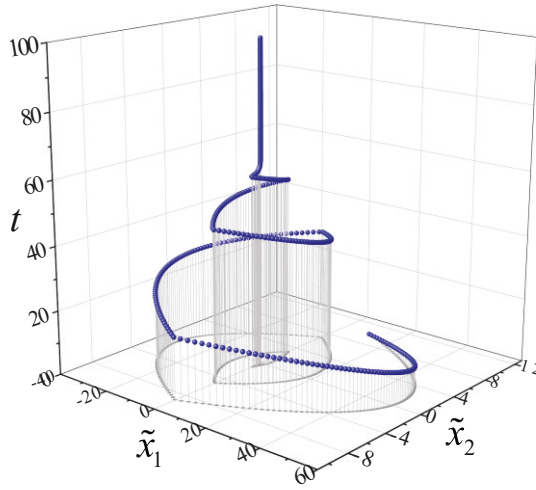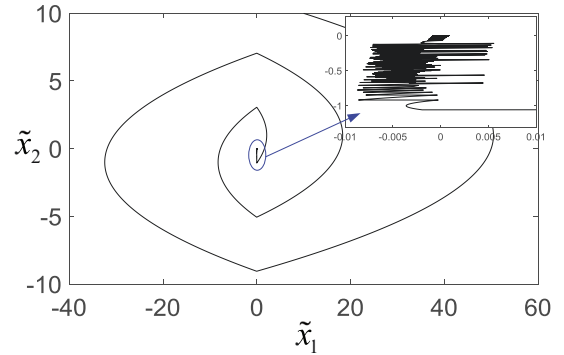
(a) 3-D View   (b) Planar graph of upward view

Figure 4.5 Observation Error Convergence of Regular Sliding Mode Observer

The super-twisting sliding mode observer in Figure 4.6 performs much better, time consumed for estimation errors convergence is reduced significantly and much less chattering hinders the rate of convergence.

(a) (b)

(a) 3-D View   (b) Planar graph of upward view

Figure 4.6 Observation Error Convergence of Super-Twisting Sliding Mode Observer

(a) (b)
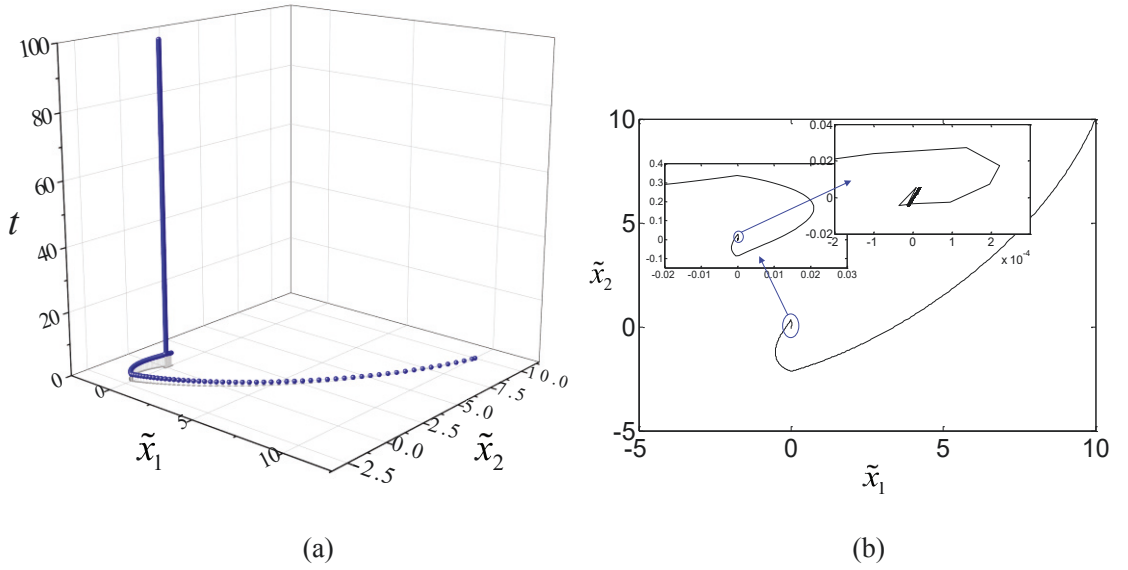
(a) 3-D View   (b) Planar graph of upward view

Figure 4.7 Observation Error Convergence of Accelerated Super-Twisting Sliding Mode Observer

As can be observed in Figure 4.7, by introducing a "system damping" to accelerate the super-twisting sliding mode observer, convergence time is reduced further with shorter trajectory towards to the (0,0) point and with little chattering.

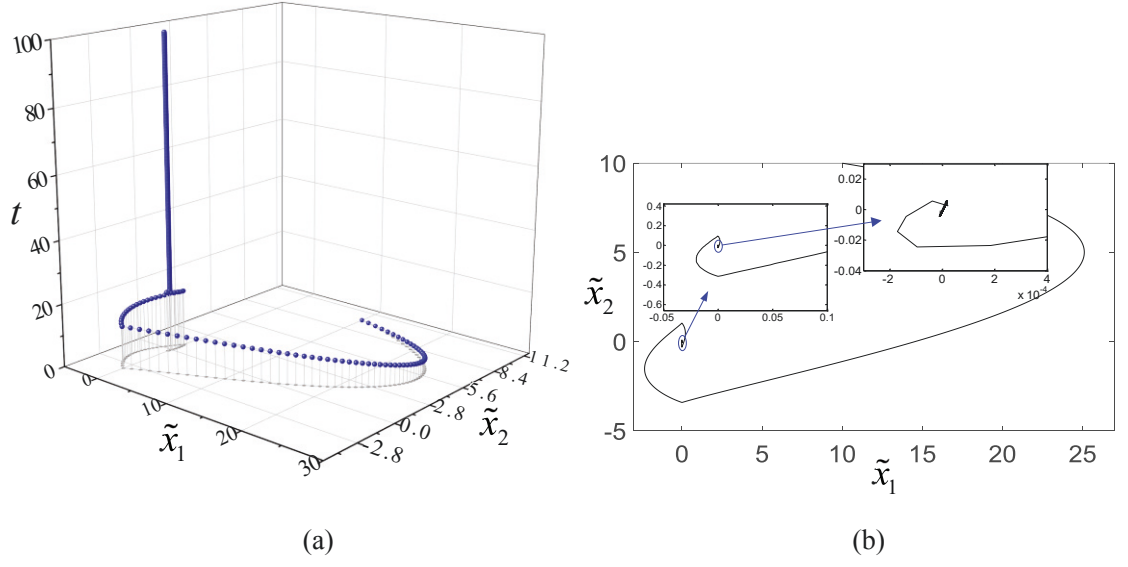(a)   (b)
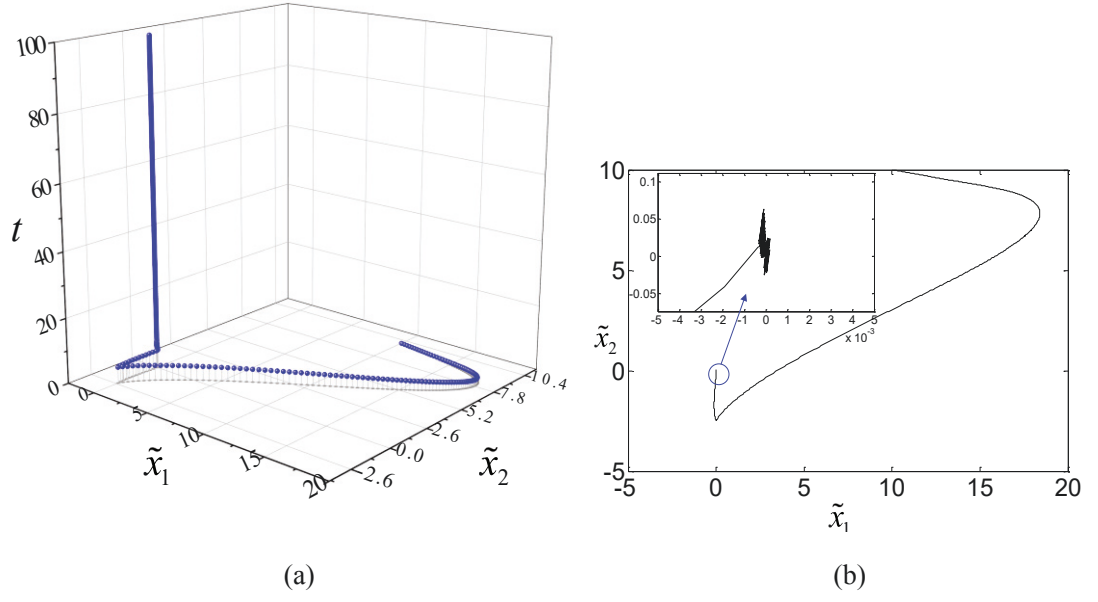
(a) 3-D View   (b) Planar graph of upward view

Figure 4.8 Observation Error Convergence of Adaptive Super-Twisting Sliding Mode Observer

(a)   (b)
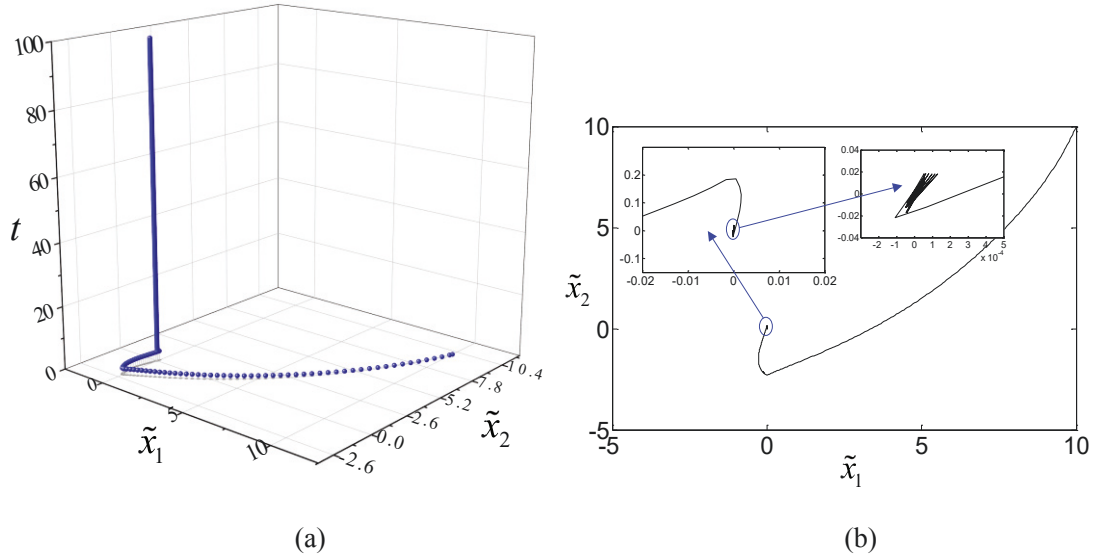
(a) 3-D View   (b) Planar graph of upward view

Figure 4.9 Observation Error Convergence of Accelerated Adaptive Super-Twisting Sliding Mode Observer

In Figure 4.8 it reveals that by introducing the adaptive sliding mode gains the convergence is also accelerated that is because the larger observation error is, the larger sliding mode gain is, but when the trajectory closes to (0,0) the chattering depends on adaptive gains configuration of the adaptive sliding mode gains. The proposed accelerated

adaptive super-twisting sliding mode observer in Figure 4.9 performs the best, the trajectory achieves (0,0) almost directly so that the rate of estimation errors convergence is accelerated effectively. From the partially enlarged view superficially it seems that both STW and AASTW do not bring obvious chattering when the estimation errors get close to the origin, that is because all sliding mode observers are tested in the same time period with the same sample time, trajectory of the proposed AASTW reaches close to the (0,0) point firstly and keep iteration but the others are still on going so that chattering of AASTW is accumulated in the remaining time, but the proposed AASTW can make the observation error converge to a required extent first with no doubt.

4.3 Observation of Torque in Drive Shaft Using AASTW

One of the main defects of AMT is the poor shift smoothness. For the electric vehicles with such type of transmission, the process of shifting starts at the vehicle control unit (VCU) sends command to the motor control unit (MCU) to unload torque output dynamically. In order to improve the shifting quality, motor torque unloading control is researched. However, stopping the motor torque output does not ensure that zero remaining torque in the meshed gears actually before the sleeve detached, because there may still exist much elastic potential energy accumulated in the elastic parts, especially for the heavy loading vehicles going on a rough road. If the sleeve is detached from the current gear at this moment, the accumulated elastic potential energy in the elastic parts will be released in quite a short time, this will cause torsional vibrations in the drivetrain and the driver will feel an unpleasant shifting jerk.

As the drive shaft and tires are the most important compliant parts of the drivetrain, the oscillating drive shaft will bring vibration and shocks to vehicle body further [143]. Therefore, knowing the real-time torque transmitted in the drive shaft can improve shifting quality a lot regarding computing an optimal shifting time and minimizing torsional oscillations [144,145].

4.3.1 Drive Shaft Torque Observer Design

The electric vehicle drivetrain model is still based on the clutchless motor-transmission integrated system with two-speed AMT as shown in Figure 2.1, and the drive shaft and tires are regarded elastically. Therefore, when the vehicle is operated under a fixed gear ratio, the drivetrain can be modeled as spring-damping system [146] as in the following equations.

$$\dot{\omega}_m = \frac{1}{J_i}\left(T_m - \frac{1}{i_t i_f}T_d\right) \tag{4.43}$$

$$\dot{\omega}_w = \frac{1}{J_v}\left(T_d - T_v\right) \tag{4.44}$$

$$\dot{T}_d = k_d\left(\frac{1}{i_t i_f}\omega_m - \omega_w\right) + d_d\left(\frac{1}{i_t i_f}\dot{\omega}_m - \dot{\omega}_w\right) \tag{4.45}$$

In above equations, the symbols ω is rotary speed, J is (equivalent) rotational inertia, T is torque, i is gear ratio, $i=1, 2$, K is torsional stiffness, and d is torsional damping. The subscripts m indicates motor, w indicates the wheel, i indicates the current meshed gear, f indicates the final drive, d indicates the drive shaft, v indicates equivalent vehicle body mass. The motor torque T_m depends on the accelerator pedal angle θ and motor speed.
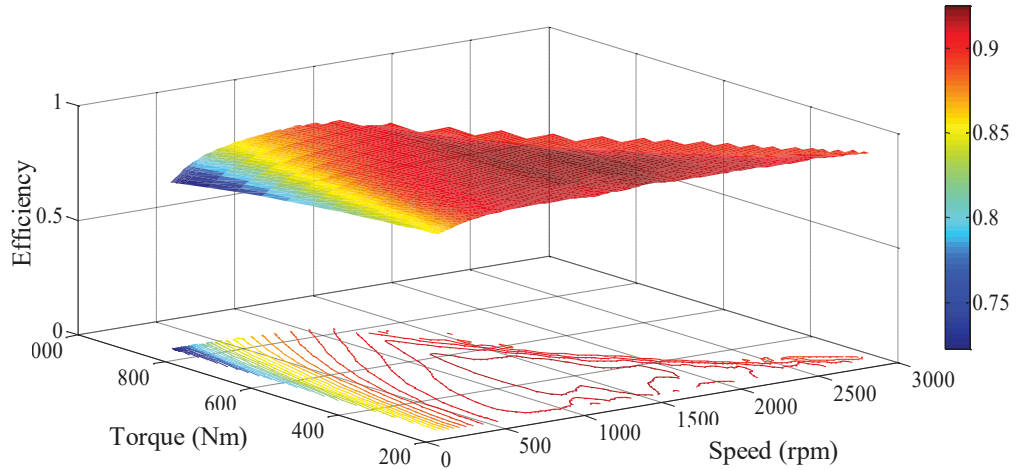

Figure 4.10 Motor Efficiency Map

Given motor torque output is restricted by the external characteristics of motor as shown in Figure 4.10, and in many practical cases motor actual torque output can also be

obtained by Look-up tables based on the map. Therefore, T_m should be expressed in a nonlinear function as Equation (4.46). The resistance includes rolling resistance, incline drag, air drag, and accelerating drag, it also should be a nonlinear function defined as Equation (4.47), in this drivetrain modelling tire slip is neglected.

$$T_m = T_m\left(\theta, \omega_m\right) \triangleq f_m\left(u, \omega_m\right) \tag{4.46}$$

$$T_v = r_w\left(\underbrace{mgc_r \cos\chi_{road}}_{rolling} + \underbrace{mg\sin\chi_{road}}_{incline} + \underbrace{\frac{1}{2}c_{air}\rho_a A_L \omega_w^2 r_w^2}_{air} + \underbrace{mr_w\frac{d\omega_w}{dt}}_{accelerating}\right) \triangleq f_v\left(\omega_w\right) \tag{4.47}$$

As motor angular speed and wheel angular speed can be measured directly, the two speed signals obtained by sensors in a fixed sample time are selected as output of measurement, together with the accelerator pedal angle are designed as inputs of the observer. The observation system structure is as Figure 4.11, the collected angular speed signals are transmitted on CAN bus, as well as motor torque output information, the observer reads these signals from the vehicle control unit (VCU), communications between driver's accelerator pedal command and the motor control unit (MCU) are also transmitted on another CAN bus, and noise or disturbance regarded as bounded is considered in the observer.

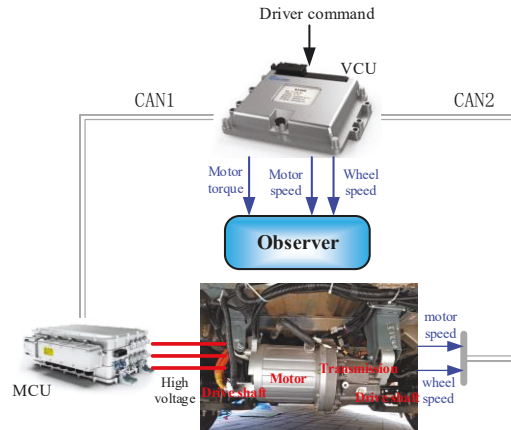Figure 4.11 Scheme of Drive Shaft Torque Estimation

Set $x_1 = \omega_m$, $x_2 = \omega_w$ and $x_3 = T_d$ which is to be observed. Consider disturbance and uncertainties in modeling and suppose the observation error and the uncertainties are bounded, i.e. $\left|\tilde{x}_{(\cdot)}\right| \le \tilde{x}_{(\cdot)}^+$, $\left|F\left(t, x_1, x_2, \hat{x}_3, u\right)\right| \le F^+$. The observation system is designed as

(4.48), and corresponding observation error equations with disturbance and uncertainties are as (4.49).

$$\begin{cases} \dot{\hat{x}}_1 = \alpha_1\left(x_1 - \hat{x}_1\right) + \dfrac{1}{J_i}\left[f_m\left(u, x_1\right) - \dfrac{1}{i_t i_f}\hat{x}_3\right] + k_1\left|x_1 - \hat{x}_1\right|^{\frac{1}{2}}\operatorname{sgn}\left(x_1 - \hat{x}_1\right) \\[4mm] \dot{\hat{x}}_2 = \alpha_2\left(x_2 - \hat{x}_2\right) + \dfrac{1}{J_v}\left[\hat{x}_3 - f_v\left(x_2\right)\right] + k_2\left|x_2 - \hat{x}_2\right|^{\frac{1}{2}}\operatorname{sgn}\left(x_2 - \hat{x}_2\right) \\[4mm] \dot{\hat{x}}_3 = \alpha_3\left(x_1 - \hat{x}_1\right) + \alpha_4\left(x_2 - \hat{x}_2\right) + k_d\left(\dfrac{1}{i_t i_f}x_1 - x_2\right) + d_d\left(\dfrac{1}{i_t i_f}\dot{x}_1 - \dot{x}_2\right) \\[4mm] + k_3\operatorname{sgn}\left(x_1 - \hat{x}_1\right) + k_4\operatorname{sgn}\left(x_2 - \hat{x}_2\right) \end{cases} \tag{4.48}$$

$$\begin{cases} \dot{\tilde{x}}_1 = -\alpha_1\tilde{x}_1 - \dfrac{1}{J_i}\left(\dfrac{1}{i_t i_f}\tilde{x}_3\right) - k_1\left|\tilde{x}_1\right|^{\frac{1}{2}}\operatorname{sgn}\left(\tilde{x}_1\right) \\[4mm] \dot{\tilde{x}}_2 = -\alpha_2\tilde{x}_2 + \dfrac{1}{J_v}\tilde{x}_3 - k_2\left|\tilde{x}_2\right|^{\frac{1}{2}}\operatorname{sgn}\left(\tilde{x}_2\right) \\[4mm] \dot{\tilde{x}}_3 = -\alpha_3\tilde{x}_1 - \alpha_4\tilde{x}_2 - k_3\operatorname{sgn}\left(\tilde{x}_1\right) - k_4\operatorname{sgn}\left(\tilde{x}_2\right) + F\left(t, x_1, x_2, \hat{x}_3\right) \end{cases} \tag{4.49}$$

Define of the parameters are the same as above. In order to make the observation error for torque in drive shaft to converge, i.e. $\left(\tilde{x}_1, \tilde{x}_2, \tilde{x}_3\right) \to \left(0, 0, 0\right)$, the adaptive sliding mode gains $k_{1,2}$ should be restricted in the feasible region of (4.50), where $\varepsilon_{1,2}$ are constant values, $0 < \varepsilon_{1,2} < 1$.

$$\begin{cases} k_1 > \max\left\{\begin{array}{l} \sqrt{\dfrac{2}{J_i i_t i_f}}\sqrt{F^+ + \alpha_3\tilde{x}_1^+ + \alpha_4\tilde{x}_2^+ + k_3 + k_4}, \\[5mm] \sqrt{\dfrac{2}{J_i i_t i_f}}\dfrac{F^+ + \alpha_3\tilde{x}_1^+ + \alpha_4\tilde{x}_2^+ + k_3 + k_4}{\sqrt{F^+ + \alpha_3\tilde{x}_1^+ + k_3 - k_4}} \end{array}\right\} \cdot \dfrac{1+\varepsilon_1}{1-\varepsilon_1} \\[12mm] k_2 > \max\left\{\begin{array}{l} \sqrt{\dfrac{2}{J_v}}\dfrac{F^+ + \alpha_3\tilde{x}_1^+ + \alpha_4\tilde{x}_2^+ - k_3 + k_4}{\sqrt{F^+ - k_3 - k_4}}, \\[5mm] \sqrt{\dfrac{2}{J_v}}\dfrac{F^+ + \alpha_3\tilde{x}_1^+ + \alpha_4\tilde{x}_2^+ - k_3 + k_4}{\sqrt{F^+ + \alpha_3\tilde{x}_1^+ + k_3 - k_4}} \end{array}\right\} \cdot \dfrac{1+\varepsilon_2}{1-\varepsilon_2} \\[12mm] k_3 < -F^+ - \alpha_3\tilde{x}_1^+ - \dfrac{1}{2}\alpha_4\tilde{x}_2^+ \\[4mm] k_4 > F^+ + \dfrac{1}{2}\alpha_3\tilde{x}_1^+ \end{cases} \tag{4.50}$$

Proof: The initial estimation errors are set to $\tilde{x}_1 = 0$, $\tilde{x}_2 = 0$, $\tilde{x}_3 = x_3 - 0 = x_3$. If the initial $\dot{\tilde{x}}_1$,

$\dot{\tilde{x}}_2$ are positive, the sliding mode trajectories of $\tilde{x}_1 - \dot{\tilde{x}}_1$ and $\tilde{x}_2 - \dot{\tilde{x}}_2$ will get into the first quadrant. Contrarily, the sliding mode trajectories will get into the third quadrant. Positive $\dot{\tilde{x}}_1$ and $\dot{\tilde{x}}_2$ are taken into consideration in this proof, the proof for the other case is equally valid and is omitted. From the Equation (4.49) the following relationship can be obtained:

$$\begin{cases} \ddot{\tilde{x}}_1 \in \dfrac{1}{J_i i_t i_f}\left[-F^+, F^+\right] - \alpha_1 \dot{\tilde{x}}_1 + \dfrac{1}{J_i i_t i_f}\left[\alpha_3 \tilde{x}_1 + \alpha_4 \tilde{x}_2 + k_3 \operatorname{sgn}(\tilde{x}_1) + k_4 \operatorname{sgn}(\tilde{x}_2)\right] - \dfrac{k_1 \dot{\tilde{x}}_1}{2\sqrt{|\tilde{x}_1|}} \\ \ddot{\tilde{x}}_2 \in \dfrac{1}{J_v}\left[-F^+, F^+\right] - \alpha_2 \dot{\tilde{x}}_2 + \dfrac{1}{J_v}\left[-\alpha_3 \tilde{x}_1 - \alpha_4 \tilde{x}_2 - k_3 \operatorname{sgn}(\tilde{x}_1) - k_4 \operatorname{sgn}(\tilde{x}_2)\right] - \dfrac{k_2 \dot{\tilde{x}}_2}{2\sqrt{|\tilde{x}_2|}} \end{cases} \quad (4.51)$$

$$\ddot{\tilde{x}}_{1_{max}} \leq \begin{cases} \left|\dfrac{F^+}{J_i i_t i_f} + \dfrac{1}{J_i i_t i_f}\left(\alpha_3 \tilde{x}_1^+ + \alpha_4 x_2^+ + k_3 + k_4\right)\right| & \tilde{x}_2 > 0 \\ \left|\dfrac{F^+}{J_i i_t i_f} + \dfrac{1}{J_i i_t i_f}\left(\alpha_3 \tilde{x}_1^+ + k_3 - k_4\right)\right| & \tilde{x}_2 \leq 0 \end{cases} \quad (4.52)$$

$$\ddot{\tilde{x}}_{2_{max}} \leq \begin{cases} \left|\dfrac{F^+}{J_v} + \dfrac{1}{J_v}\left(-k_3 - k_4\right)\right| & \tilde{x}_1 \geq 0 \\ \left|\dfrac{F^+}{J_v} + \dfrac{1}{J_v}\left(\alpha_3 \tilde{x}_1^+ + k_3 - k_4\right)\right| & \tilde{x}_1 < 0 \end{cases} \quad (4.53)$$
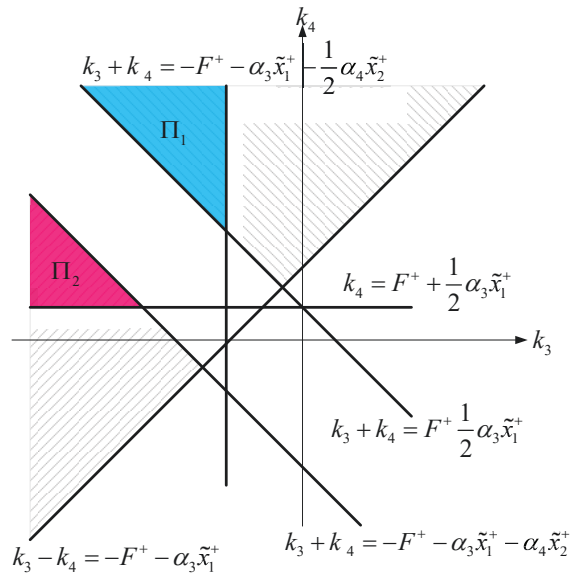

Figure 4.12 Domain of Π_1 and Π_2

When the trajectory is in the first quadrant the following inequalities shown as (4.52) and (4.53) can be obtained based on (4.51). If $k_3 \in \Pi_1, k_4 \in \Pi_2$ as shown in Figure 4.12, the

limitations of k_3 and k_4 will make $\ddot{\tilde{x}}_1 < 0$ and $\ddot{\tilde{x}}_2 < 0$, so that the trajectory is driven towards $\dot{\tilde{x}}_{1,2} = 0$ and it is limited in the scope enclosed by $\tilde{x}_{1,2} = 0$, $\dot{\tilde{x}}_{1,2} = 0$ and $\dot{\tilde{x}}_{1,2}^2 = 2\left|\ddot{\tilde{x}}_{1,2_{max}}\right|\left(\tilde{x}_{1,2_M} - \tilde{x}_{1,2}\right)$ (line I in Figure 4.13, derived from integral calculation).
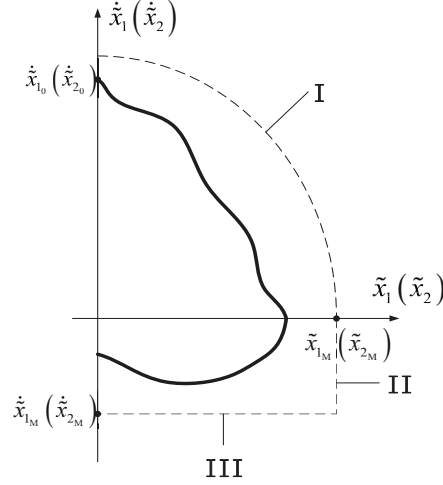

Figure 4.13 Sketch of Sliding Mode Trajectory

When the trajectory transits through $\dot{\tilde{x}}_{1,2} = 0$, it comes into the fourth quadrant, and the trajectory is driven towards $\tilde{x}_{1,2} = 0$ because of the passive $\dot{\tilde{x}}_{1,2}$. The minimum $\dot{\tilde{x}}_{1,2}$ can be obtained as (4.55) by solving Equation (4.54).

$$\begin{cases} \ddot{\tilde{x}}_1 = -\dfrac{1}{J_i i_t i_f} F\left(t, x_1, x_2, \hat{x}_3\right) - \alpha_1 \dot{\tilde{x}}_1 + \dfrac{1}{J_i i_t i_f}\left[\alpha_3 \tilde{x}_1 + \alpha_4 \tilde{x}_2 + k_3 + k_4 \operatorname{sgn}\left(\tilde{x}_2\right)\right] - \dfrac{k_1 \dot{\tilde{x}}_1}{2\sqrt{|\tilde{x}_1|}} = 0 \\ \ddot{\tilde{x}}_2 = \dfrac{1}{J_v} F\left(t, x_1, x_2, \hat{x}_3\right) - \alpha_2 \dot{\tilde{x}}_2 + \dfrac{1}{J_v}\left[-\alpha_3 \tilde{x}_1 - \alpha_4 \tilde{x}_2 - k_3 \operatorname{sgn}\left(\tilde{x}_1\right) - k_4\right] - \dfrac{k_2 \dot{\tilde{x}}_2}{2\sqrt{|\tilde{x}_2|}} = 0 \end{cases} \quad (4.54)$$

Therefore, the trajectory is enclosed by $\tilde{x}_{1,2} = 0$, $\dot{\tilde{x}}_{1,2} = 0$, $\tilde{x}_{1,2} = \tilde{x}_{1,2_M}$ and $\dot{\tilde{x}}_{1,2} = \dot{\tilde{x}}_{1,2_M}$. From the (4.55), it is obvious that derivative of observation errors is bounded by the line III as shown in Figure 4.13, and given the limits of the sliding mode gains shown in (4.50), a further conclusion can be drawn as (4.56) and (4.57). Therefore, $\dot{\tilde{x}}_{1,2}$ will converge to 0, and considering the equation $\dot{\tilde{x}}_{1,2}^2 = 2\left|\ddot{\tilde{x}}_{1,2_{max}}\right|\left(\tilde{x}_{1,2_M} - \tilde{x}_{1,2}\right)$, $\tilde{x}_{1,2}$ is convergent as well. According to Equation (4.49), as long as the model is accurate $\tilde{x}_3$ will be driven to converge to 0 because of the bounded and convergent $\tilde{x}_1$ and $\tilde{x}_2$, convergence of the

proposed AASTW-based drive shaft torque observer is proven.

$$
\begin{cases}
\dot{\tilde{x}}_1 = \dfrac{2\sqrt{|\tilde{x}_1|}}{2\alpha_1\sqrt{|\tilde{x}_1|}+k_1} \dfrac{1}{J_i i_t i_f}\left[-F\left(t,x_1,x_2,\hat{x}_3\right)+\alpha_3\tilde{x}_1+\alpha_4\tilde{x}_2+k_3+k_4\,\mathrm{sgn}\left(\tilde{x}_2\right)\right] \\[4mm]
> -\dfrac{2}{k_1}\sqrt{x_{1_M}}\dfrac{1}{J_i i_t i_f}\left(F^+ +\alpha_3\tilde{x}_1^+ +\alpha_4\tilde{x}_2^+ +k_3+k_4\right) \triangleq \dot{\tilde{x}}_{1_M} \\[4mm]
\dot{\tilde{x}}_2 = \dfrac{2\sqrt{|\tilde{x}_2|}}{2\alpha_2\sqrt{|\tilde{x}_2|}+k_2} \dfrac{1}{J_v}\left[F\left(t,x_1,x_2,\hat{x}_3\right)-\alpha_3\tilde{x}_1-\alpha_4\tilde{x}_2-k_3\,\mathrm{sgn}\left(\tilde{x}_1\right)-k_4\right] \\[4mm]
> -\dfrac{2}{k_2}\sqrt{x_{2_M}}\dfrac{1}{J_v}\left(F^+ +\alpha_3\tilde{x}_1^+ +\alpha_4\tilde{x}_2^+ -k_3+k_4\right) \triangleq \dot{\tilde{x}}_{2_M}
\end{cases}
\tag{4.55}
$$

$$
\dfrac{\left|\dot{\tilde{x}}_{1_M}\right|}{\left|\dot{\tilde{x}}_{1_0}\right|} \le \dfrac{\dfrac{2}{k_1}x_{1_M}^{\frac{1}{2}}\dfrac{1}{J_i i_t i_f}\left(F^+ +\alpha_3\tilde{x}_1^+ +\alpha_4\tilde{x}_2^+ +k_3+k_4\right)}{\min\left\{\begin{array}{l}\sqrt{2x_{1_M}\left[\dfrac{F^+}{J_i i_t i_f}+\dfrac{1}{J_i i_t i_f}\left(\alpha_3\tilde{x}_1^+ +\alpha_4 x_2^+ +k_3+k_4\right)\right]}, \\[4mm] \sqrt{2x_{1_M}\left[\dfrac{F^+}{J_i i_t i_f}+\dfrac{1}{J_i i_t i_f}\left(\alpha_3\tilde{x}_1^+ +k_3-k_4\right)\right]}\end{array}\right\}}
$$

$$
< \max\left\{\begin{array}{l}\dfrac{1}{k_1}\sqrt{\dfrac{2}{J_i i_t i_f}}\sqrt{F^+ +\alpha_3\tilde{x}_1^+ +\alpha_4\tilde{x}_2^+ +k_3+k_4}, \\[4mm] \dfrac{1}{k_1}\sqrt{\dfrac{2}{J_i i_t i_f}}\dfrac{F^+ +\alpha_3\tilde{x}_1^+ +\alpha_4\tilde{x}_2^+ +k_3+k_4}{\sqrt{F^+ +\alpha_3\tilde{x}_1^+ +k_3-k_4}}\end{array}\right\} < \dfrac{1-\varepsilon_1}{1+\varepsilon_1} < 1
\tag{4.56}
$$

$$
\dfrac{\left|\dot{\tilde{x}}_{2_M}\right|}{\left|\dot{\tilde{x}}_{1_0}\right|} \le \dfrac{\dfrac{2}{k_2}x_{2_M}^{\frac{1}{2}}\dfrac{1}{J_v}\left(F^+ +\alpha_3\tilde{x}_1^+ +\alpha_4\tilde{x}_2^+ -k_3+k_4\right)}{\min\left\{\sqrt{2x_{2_M}\left[\dfrac{F^+}{J_v}+\dfrac{1}{J_v}\left(-k_3-k_4\right)\right]},\ \sqrt{2x_{2_M}\left[\dfrac{F^+}{J_v}+\dfrac{1}{J_v}\left(\alpha_3\tilde{x}_1^+ +k_3-k_4\right)\right]}\right\}}
$$

$$
< \max\left\{\dfrac{1}{k_2}\sqrt{\dfrac{2}{J_v}}\dfrac{F^+ +\alpha_3\tilde{x}_1^+ +\alpha_4\tilde{x}_2^+ -k_3+k_4}{\sqrt{F^+ -k_3-k_4}},\ \dfrac{1}{k_2}\sqrt{\dfrac{2}{J_v}}\dfrac{F^+ +\alpha_3\tilde{x}_1^+ +\alpha_4\tilde{x}_2^+ -k_3+k_4}{\sqrt{F^+ +\alpha_3\tilde{x}_1^+ +k_3-k_4}}\right\}
\tag{4.57}
$$

$$
< \dfrac{1-\varepsilon_2}{1+\varepsilon_2} < 1
$$

The Lyapunov function is designed as

$$
L(\tilde{\mathrm{x}}) = \frac{1}{2}\tilde{x}_1^2 + \frac{1}{2}\tilde{x}_2^2 > 0
\tag{4.58}
$$

and corresponding partial derivative

$$\frac{\partial}{\partial t} L\left(\tilde{x}_1, \tilde{x}_2\right) = \tilde{x}_1 \dot{\tilde{x}}_1 + \tilde{x}_2 \dot{\tilde{x}}_2$$

$$= \tilde{x}_1 \left[-\alpha_1 \tilde{x}_1 - \frac{1}{J_i i_t i_f} \tilde{x}_3 - k_1 |\tilde{x}_1|^{\frac{1}{2}} \operatorname{sgn}\left(\tilde{x}_1\right) \right] + \tilde{x}_2 \left[-\alpha_2 \tilde{x}_2 + \frac{1}{J_v} \tilde{x}_3 - k_2 |\tilde{x}_2|^{\frac{1}{2}} \operatorname{sgn}\left(\tilde{x}_2\right) \right] \tag{4.59}$$

If k_1 and k_2 meet the requirement of (4.60), $L\left(\tilde{x}_1, \tilde{x}_2\right) \cdot \dot{L}\left(\tilde{x}_1, \tilde{x}_2\right) < 0$ will be realized to make the system stable.

$$k_1 > \begin{cases} -\alpha_1 \sqrt{|\tilde{x}_1|} - \dfrac{\tilde{x}_3}{J_i i_t i_f \sqrt{|\tilde{x}_1|}} & x_1 > 0 \\[3mm] -\alpha_1 \sqrt{|\tilde{x}_1|} + \dfrac{\tilde{x}_3}{J_i i_t i_f \sqrt{|\tilde{x}_1|}} & x_1 < 0 \end{cases} , \quad k_2 > \begin{cases} -\alpha_2 \sqrt{|\tilde{x}_2|} + \dfrac{\tilde{x}_3}{J_v \sqrt{|\tilde{x}_2|}} & x_2 > 0 \\[3mm] -\alpha_2 \sqrt{|\tilde{x}_2|} - \dfrac{\tilde{x}_3}{J_v \sqrt{|\tilde{x}_2|}} & x_2 < 0 \end{cases} \tag{4.60}$$

When the estimation errors $\left(\tilde{x}_1, \tilde{x}_2, \tilde{x}_3\right)$ get close to the small neighbourhood of the origin $(0,0,0)$, combining with the (4.61) based on the infinitesimals of the same order theorem, a conclusion can be drawn that positive k_1 and k_2 can meet the requirement of

$$\tilde{x}_1 \left[-\alpha_1 \tilde{x}_1 - \frac{1}{J_i i_t i_0} \tilde{x}_3 - k_1 |\tilde{x}_1|^{\frac{1}{2}} \operatorname{sgn}\left(\tilde{x}_1\right) \right] < 0 \text{ and } \tilde{x}_2 \left[-\alpha_2 \tilde{x}_2 + \frac{1}{J_v} \tilde{x}_3 - k_2 |\tilde{x}_2|^{\frac{1}{2}} \operatorname{sgn}\left(\tilde{x}_2\right) \right] < 0. \text{ It}$$

is obvious that $L\left(\tilde{x}_1, \tilde{x}_2\right) \cdot \dot{L}\left(\tilde{x}_1, \tilde{x}_2\right) < 0$ is satisfied, so that $\tilde{x}_1$ and $\tilde{x}_2$ are asymptotic stable; similar to the Filippove transformation in Equation (4.17), $\tilde{x}_1$ is stable too. Stability of the proposed drive shaft torque observer is proven.

$$\lim_{\tilde{x}_1 \to 0, \tilde{x}_3 \to 0} \frac{\tilde{x}_3}{\sqrt{|\tilde{x}_1|}} = 0 , \quad \lim_{\tilde{x}_2 \to 0, \tilde{x}_3 \to 0} \frac{\tilde{x}_3}{\sqrt{|\tilde{x}_2|}} = 0 \tag{4.61}$$

4.3.2 Simulation Test

Simulation of the AASTW-based observer of torque in drive shaft is carried on AMEsim-MATLAB joint environment. Physical model of EV powertrain is established on AMEsin as in Figure 4.14 (a), from which motor speed, wheel speed and real torque in drive shaft are measured by sensors and then send them to the observer module on Matlab as in Figure 4.14 (b), so that performance of observer is tested.
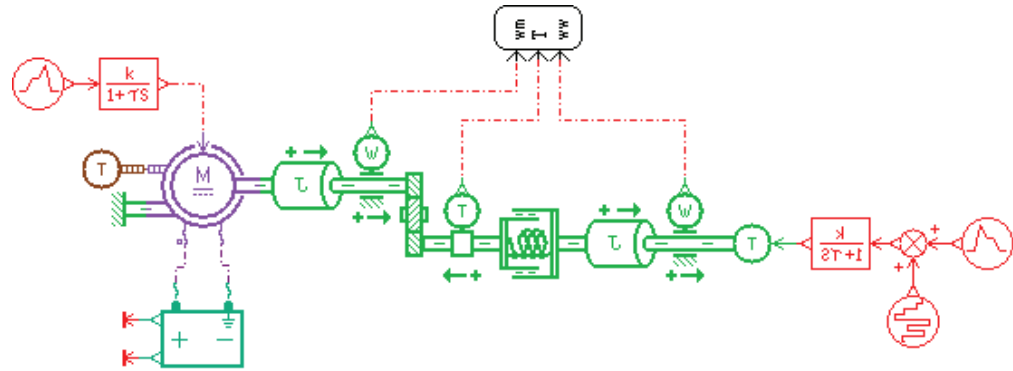
(a)
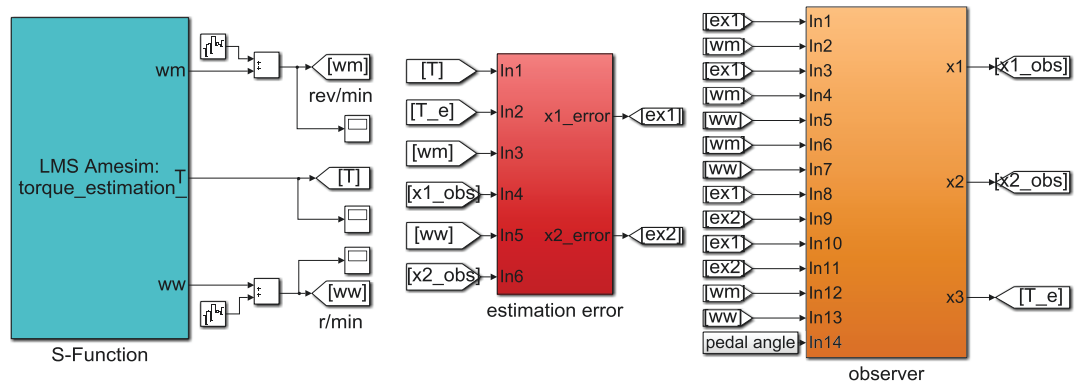
(b)

Figure 4.14 Simulation Model of Observer for Torque in EV Drive Shaft
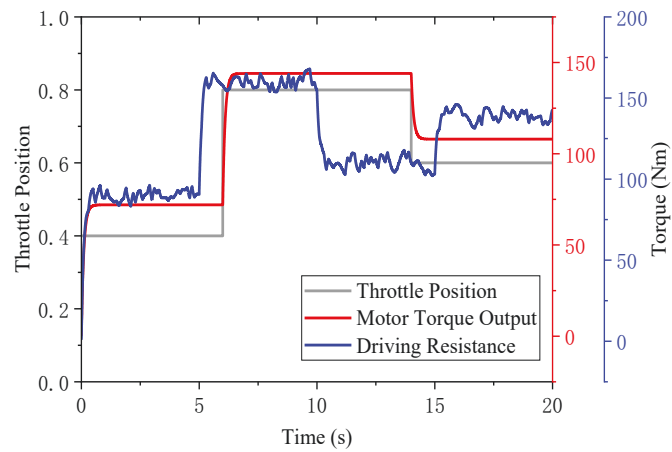

Figure 4.15 Working Condition Settings for Simulation

In the simulation test, resistance in driving is simulated by a step signal as in Figure 4.15, and high power noise is introduced to simulate road condition variation, disturbance or uncertainties, and the unstable deviation in vehicle mass estimation, etc. In Figure 4.15

driving operation is also illustrated, driver's command to pedal is also simulated by step signal and an inertial element is introduced to simulate the time delay of motor torque output. Critical parameters of the simulation are shown in Table 4.2.

Table 4.2 Parameters Configuration for Simulation

| Parameters of Powertrain	Value	Parameters of Observer	Value
Motor Power (kW)	53	Initial Value of k_1	30
Motor Maximum Torque (Nm)	180	Initial Value of k_2	10
Motor Maximum Speed (rpm)	9000	Sliding Mode Gain k_3	- 20
Current Gear Ratio	6.135	Sliding Mode Gain k_4	30
Equivalent Moment of Inertia J_i (kgm2)	2.8	System Damping α_1	1
Equivalent Moment of Inertia J_v (kgm2)	183.75	System Damping α_2	1
Drive Shaft Torsional Stiffness (Nm/rad)	90729.58	System Damping α_3	1
Drive Shaft Torsional Damp (Nm/(rad/s))	3500	System Damping α_4	1
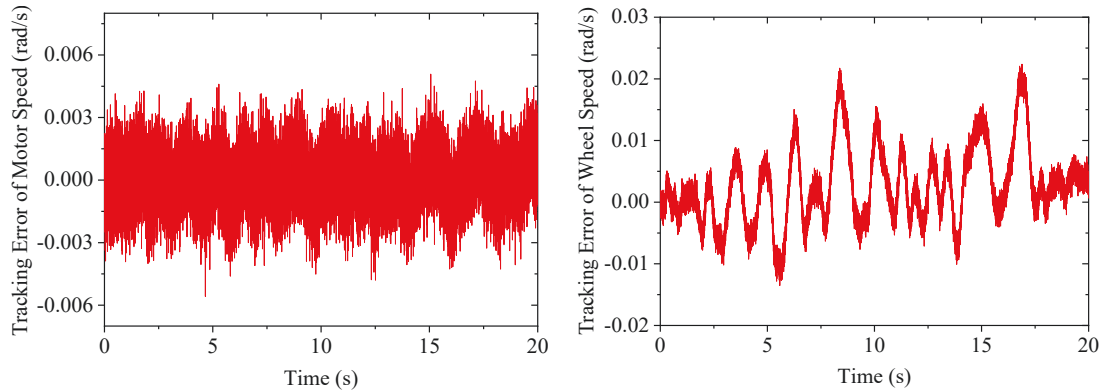
Figure 4.16 Tracking Errors of the Measurable States of EV Drivetrain

In the simulation of driver's tipping in/out within 20s, shifting doesn't come about and gear ratio is fixed, the vehicle keeps accelerating at this period. Because vehicle longitudinal force model in Matlab is close to the physical powertrain model in AMEsim accurately, but in practice vehicle powertrain usually works in bad conditions and order of magnitude of resistance or disturbance is quite large, so high-power of noise signals are added in the measured signals. In Figure 4.16, tracking performances of motor speed and wheel speed are illustrated, tracking of the measurable speeds is in an accurate level
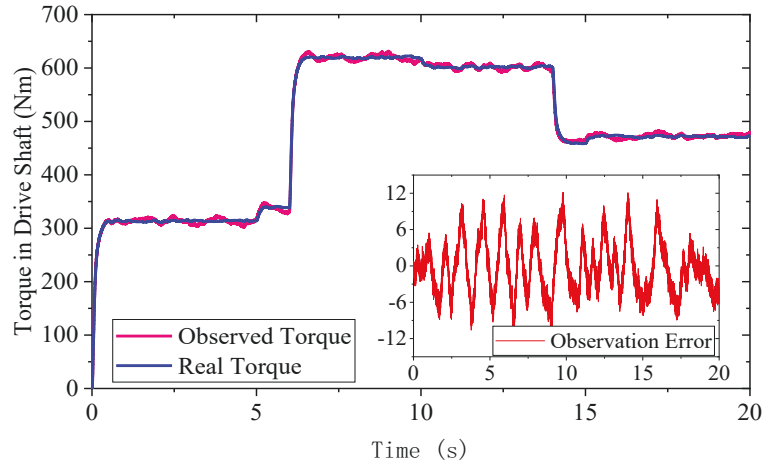
in this test even under much noises.

Figure 4.17 Observation Performance of the Torque Observer

Under joint action of the motor torque and the driving resistance in Figure 4.15, the drive shaft torque observation result is shown in Figure 4.17. The observation error can still be kept with about 4% with little overshoot and fast tracking performance, chattering is attenuated as well even though high power noise and disturbance exist.

4.4 Summary

In this chapter a novel sliding mode observer is proposed, by introduction of the system damping convergence of observation error is accelerated, and the adaptive sliding mode gains can make the variable structure more accurate so that the inherent problem of chattering is attenuated. Convergence and stability of the observer are proven mathematically. The proposed observer is applied to observe the torque in EV drive shaft and it performs satisfactorily by simulation results.

CHAPTER 5: QUANTUM OPTIMAL CONTROL OF TORSIONAL OSCILLATIONS FOR EV DRIVETRAIN

5.1 Introduction

As the absence of energy saving and buffering components in the research target, i.e. the motor-transmission integrated powertrain system, torsion oscillations will come about in the second-order system with torsional compliance and damping at the moment of driver's tipping in/out or shifting, and further it will transform into longitudinal vehicle shuffle. In this chapter research on active damping control for EV drivetrain will follow two aspects of motor torque output unloading before shifting and motor torque output increasing after shifting.

With the development of driving motor and the progress of power electronics technology, it is possible to control the driving motor more and more quickly and accurately. By calculating the optimal output of the motor torque, which is opposite to the direction of the torsional oscillation of the drivetrain system, so that the oscillation can be offset or compensated. Since the active control of torsional oscillation requires the driving motor to quickly and accurately output torque which conforms to the control law in a short time, and the control algorithm should not consume excessive computational power and long calculation time, so it should be as simple as possible in execution. Linear quadratic Gaussian makes the active damping control for torsional oscillation more feasible because of the simplicity, high efficiency and closed loop stability.

In this chapter a joint optimal damping control algorithm with an optimization unit is proposed. LQG is regarded as one of the most effective methods in vibration control under the premise of appropriate weighting matrices **Q** and **R** which directly influence optimal control law by minimizing the performance index. However, they are selected based on designer's subjective preference currently and generally, and such optimal results may not be the actual optimal usually, therefore, objective selecting method is researched

intensively. Quantum Genetic Algorithm (QGA) is a probabilistic search algorithm that introduces qubits and quantum superposition states. It uses the probability amplitude of qubit to represent the coding of chromosomes in genetic algorithms so that one chromosome contains multiple states at the same time and diversity of the population is increased. Furthermore, evolution of chromosomes is realized by application of the quantum revolving gate, searching speed for optimization is improved greatly.

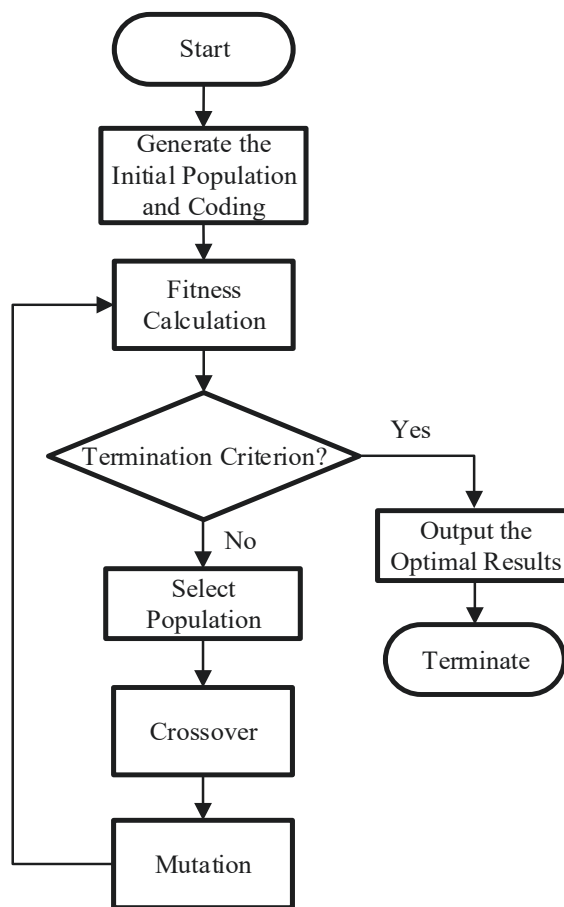## 5.2 Intelligent Optimization Based on Quantum Genetic Algorithm

Figure 5.1 Typical Genetic Algorithm Optimization Flow Chart

As an intelligent optimization algorithm, genetic algorithm simulates the evolution process in nature and the searching principle through a computer. By simulating the process of crossover, mutation and elimination of chromosomes in evolution, searching or evolution is going on for the optimal solutions. It is suitable for solving complex and nonlinear optimization problems in fields of artificial intelligence, machine learning, etc.

The typical genetic algorithm optimization flow is shown in Figure 5.1.

Quantum computing uses quantum states as the basic information unit and utilizes the characteristics of superposition, entanglement and interference in the quantum world to establish an unprecedented computing model, it breaks through the limitation of Turing model and the computing performance is improved exponentially. The quantum genetic algorithm is based on the principle of quantum computing and uses the probability of the qubit to represent genetic coding of the chromosome so that one chromosome can express the superposition of polymorphism to carry more information. Crossover and mutation in classical genetic algorithm are replaced by quantum revolving gate and searching speed for optimization is increased [147].

5.2.1 Qubit Coding

Qubit is the basic information unit in quantum computing and can be expressed as a linear superposition of two mutually independent quantum state vectors $|0>$ and $|1>$, rather than 0 or 1 in classical genetic algorithm. Because of the characteristic of entanglement and interference, qubit can also express random state $|\varphi>$ from linear superposition of the quantum ground states $|0>$ and $|1>$:

$$|\varphi> = \alpha|0> + \beta|1> \tag{5.1}$$

Where α and β are the probability amplitude of $|0>$ and $|1>$, respectively, and they meet requirement of normalization:

$$|\alpha|^2 + |\beta|^2 = 1 \tag{5.2}$$

It can be generalized to multi-qubit condition too, if there are $N = 2^n$ quantum ground state in a quantum system $|\varphi_0>, |\varphi_1> \cdots |\varphi_{N-1}>$, any one of the quantum states can be expressed as superposition state of these quantum ground state:

$$|\varphi> = \sum_{j=0}^{N-1} \alpha_j |\varphi_j> \tag{5.3}$$

Where probability amplitude α_j of quantum ground state $|\varphi_j>$ should meet the requirement of normalization as

$$\sum_{j=0}^{N-1} |\alpha_j|^2 = 1 \tag{5.4}$$

Therefore, in the parallel processing of quantum systems A n-bit quantum register can simultaneously represent 2n quantum ground states, the operation of a computer on a quantum register is equivalent to simultaneous operation on the superposition state $|\varphi>$ based on each quantum ground state, and the result is also a new superposition state, which greatly improves the calculation efficiency.

In order to demonstrate physical meaning of quantum motion better, 3D spherical coordinate is introduced to represent the qubit as:

$$|\varphi>= \cos\frac{\theta}{2}|0> + e^{i\varphi}\sin\frac{\theta}{2}|1> \tag{5.5}$$

Where probability amplitude $\cos\frac{\theta}{2}$ and $e^{i\varphi}\sin\frac{\theta}{2}$ are a pair of plural and meet normalization requirement that sum of squares is 1. Therefore, the qubit can be uniquely determined by probability amplitude vector $\left[\cos\frac{\theta}{2} \quad e^{i\varphi}\sin\frac{\theta}{2}\right]^{\mathrm{T}}$, as point P in Figure 5.2.
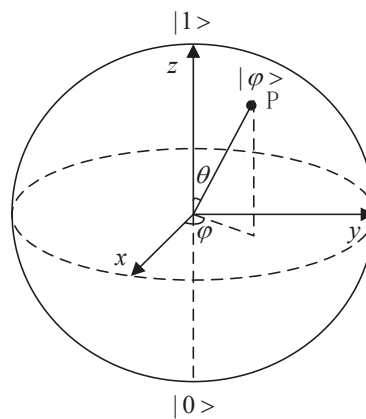

Figure 5.2 Expression of Qubit on Spherical Coordinate

On the spherical P is indicated by a pair of phase angles (θ,φ), and corresponding code of 3D chromosome is expressed as

$$q_i^y = \begin{bmatrix} \theta_{i1}^y \\ \varphi_{i1}^y \end{bmatrix} \cdots \begin{bmatrix} \theta_{ij}^y \\ \varphi_{ij}^y \end{bmatrix} \cdots \begin{bmatrix} \theta_{in}^y \\ \varphi_{in}^y \end{bmatrix} \tag{5.6}$$

The phase angle can be considered as a pair of juxtaposed genes, which can be transformed into two parallel gene chains:

$$\begin{cases} q_{i\theta}^y = \left(\theta_{i1}^y, \theta_{i2}^y, \cdots \theta_{ij}^y \cdots \theta_{in}^y \right) \\ q_{i\varphi}^y = \left(\varphi_{i1}^y, \varphi_{i2}^y, \cdots \varphi_{ij}^y \cdots \varphi_{in}^y \right) \end{cases} \tag{5.7}$$

Which the right side of the equal sign indicates the ith chromosome (i=1,2···m; j=1,2···n) of the population in yth generation, m is the population size, n is the number of quantum bits (chromosome length) which equals to dimension of the optimization, θ_{ij}^y and φ_{ij}^y represent the phase angles of the ith chromosome on the jth qubit in yth generation population, respectively.

5.2.2 Revolving Gate of Quantum Evolution

Revolving gate of quantum is used for evolution of the chromosome based on characteristics of quantum genetic algorithm, of which operation is expressed as

$$R(\Theta_i) = \begin{bmatrix} \cos \Theta_i & -\sin \Theta_i \\ \sin \Theta_i & \cos \Theta_i \end{bmatrix} \tag{5.8}$$

$$\begin{bmatrix} \alpha_i' \\ \beta_i' \end{bmatrix} = R(\Theta_i) \begin{bmatrix} \alpha_i \\ \beta_i \end{bmatrix} = \begin{bmatrix} \cos \Theta_i & -\sin \Theta_i \\ \sin \Theta_i & \cos \Theta_i \end{bmatrix} \begin{bmatrix} \alpha_i \\ \beta_i \end{bmatrix} \tag{5.9}$$

Where Θ_i is the revolving gate angle of the ith qubit, $R(\Theta_i)$ is the quantum revolving gate, $[\alpha_i, \beta_i]^T$ and $[\alpha_i', \beta_i']^T$ is the probability amplitude of the qubit after revolution; from the Equation (5.9) α_i' and β_i' can be expressed as Equation (5.10), respectively.

$$\begin{cases} \alpha_i' = \alpha_i \cos \Theta_i - \beta_i \sin \Theta_i \\ \beta_i' = \alpha_i \sin \Theta_i + \beta_i \cos \Theta_i \end{cases} \tag{5.10}$$

It still meets the requirements of normalization after evolution:

$$|\alpha_i'|^2 + |\beta_i'|^2 = (\alpha_i \cos \Theta_i - \beta_i \sin \Theta_i)^2 + (\alpha_i \cos \Theta_i + \beta_i \sin \Theta_i)^2 = |\alpha_i|^2 + |\beta_i|^2 = 1 \tag{5.11}$$

5.2.3 Realization of Quantum Genetic Algorithm

Initialization: Substitute the qubit coding for the binary coding of conventional GA, set k be the number of qubits encoding each gene, set the population in y^{th} negation including n individuals as $Q(x) = \{q_1^y, q_2^y, \cdots q_n^y\}$, q_i^y is the ith quantum chromosome in y^{th} generation which is expressed as

$$q_i^y = \begin{bmatrix} \alpha_{11}^y & \alpha_{12}^y & \cdots & \alpha_{1k}^y & \alpha_{21}^y & \alpha_{22}^y & \cdots & \alpha_{2k}^y & \cdots & \alpha_{m1}^y & \alpha_{m1}^y & \cdots & \alpha_{mk}^y \\ \beta_{11}^y & \beta_{12}^y & \cdots & \beta_{1k}^y & \beta_{21}^y & \beta_{22}^y & \cdots & \beta_{2k}^y & \cdots & \beta_{m1}^y & \beta_{m1}^y & \cdots & \beta_{mk}^y \end{bmatrix} \quad (5.12)$$

The total amount of chromosome is 2kmn of which probability amplitude is initialized to $1/\sqrt{2}$, so that each chromosome in 0 generation can be linearly superposed with the same probability as (5.13), where X_j is the string $(x_1, x_2 \cdots x_m)$, x_i is 0 or 1.

$$|\varphi_{q_i^0}\rangle = \sum_{j=1}^{2^{km}} \frac{1}{\sqrt{2^{km}}} |X_j\rangle \quad (5.13)$$

Table 5.1 Adjustment Strategy of Quantum Revolving Gate

x_i	x_{Besti}	$f(x)>f(x_{Besti})$	$\Delta\Theta_i$	$s(\alpha_i, \beta_i)$			
				$\alpha_i\beta_i > 0$	$\alpha_i\beta_i < 0$	$\alpha_i = 0$	$\beta_i = 0$
0	0	False	0	0	0	0	0
0	0	True	0	0	0	0	0
0	1	False	0.01π	+1	- 1	0	±1
0	1	True	0.01π	- 1	+1	±1	0
1	0	False	0.01π	- 1	+1	±1	0
1	0	True	0.01π	+1	- 1	0	±1
1	1	False	0	0	0	0	0
1	1	True	0	0	0	0	0

Revolving Gate of Quantum: In quantum genetic algorithm the revolving gate is the execution of evolution, in this chapter a general strategy is adopted as in Table 5.1 [148]. In the table x_i is the ith bit of the current chromosome, x_{Besti} is the ith bit of the current optimal chromosome, $f(x)$ is the fitness function in optimization, $s(\alpha_i, \beta_i)$ is direction

of revolving angle, $\Delta\Theta_i$ is the revolving angle, which is designed as Table 5.1. Flow chart

of the quantum genetic algorithm is in Figure 5.3, of which key content is comparing the

fitness function $f(x)$ corresponding to individual q_i^y with the fitness function $f(x_{\text{Best}i})$

corresponding to the optimal individual, if $f(x_i) > f(x_{\text{Best}i})$, by adjustment of qubit

corresponding to q_i^y so that probability amplitude of α_i and β_i can make individuals evolve

towards x_i, otherwise, evolve towards $x_{\text{Best}i}$.
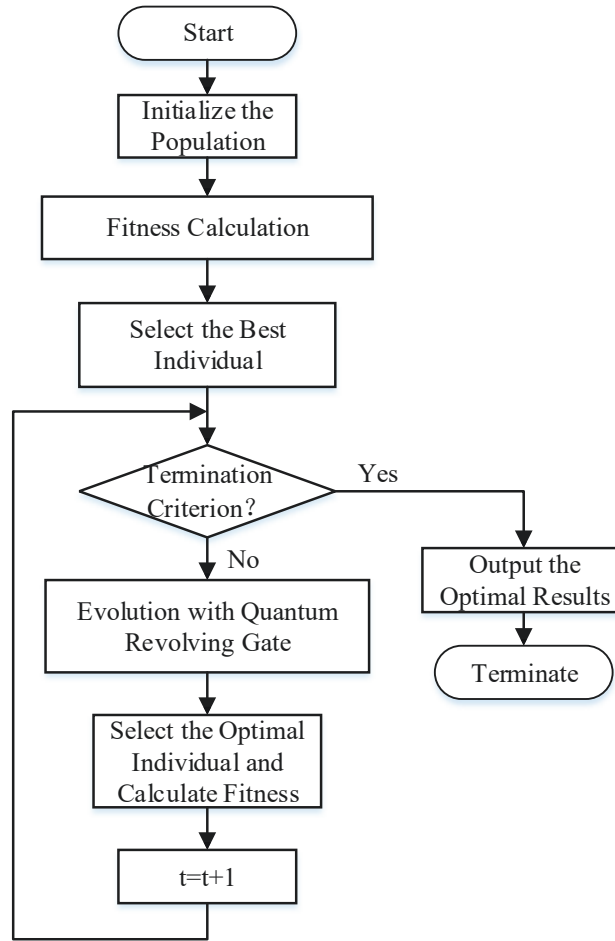
Figure 5.3 Quantum Genetic Algorithm Optimization Flow Chart

5.3 Active Damping Control for EV Drivetrain Oscillation

5.3.1 Optimal Control of Motor Torque Unloading Before Shifting

Based on the model of EV powertrain in Chapter 2, motor speed, drive shaft torsional

angle and wheel speed are selected as state variables, the dynamic equations in (2.50) and (2.51) can be transformed into

$$\dot{x} = Ax + Bu + Hl \tag{5.14}$$

Where $x_1 = \dfrac{\theta_m}{i_t i_f} - \theta_w$, $x_2 = \dot{\theta}_w$, $x_3 = \dot{\theta}_m$, $i = i_t i_f$, $J_1 = J_m + \dfrac{J_t}{i_t^2} + \dfrac{J_f}{i_t^2 i_f^2}$, $J_2 = J_w + mr_w^2$,

$d_1 = \dfrac{d_t}{i_t^2} + \dfrac{d_f}{i_t^2 i_f^2}$, $d_2 = d_w + mgc_{r2}r_w^2$, $l = r_w m\left(c_{r1} + g\sin\chi_{road}\right)$,

$$A = \begin{pmatrix} 0 & -1 & \dfrac{1}{i} \\[2mm] \dfrac{k}{J_2} & -\dfrac{d+d_2}{J_2} & \dfrac{d}{iJ_2} \\[2mm] -\dfrac{k}{iJ_1} & \dfrac{d}{iJ_1} & -\dfrac{d_1+\dfrac{d}{i^2}}{J_1} \end{pmatrix}, \quad B = \begin{pmatrix} 0 \\[2mm] 0 \\[2mm] \dfrac{1}{J_1} \end{pmatrix}, \quad H = \begin{pmatrix} 0 \\[2mm] -\dfrac{1}{J_2} \\[2mm] 0 \end{pmatrix}.$$

Among the selected state variables the drive shaft torsional angle is usually difficult to be measured timely, in [149] correlation of the torque in drive shaft and torsional angle is researched, similarly, in this chapter drive shaft torsional angle is obtained from drive shaft torque divided by torsional stiffness.

Active damping control of oscillation for shifting is unloading motor torque to 0 dynamically rather than directly so that it is suitable for detaching the meshed gears in transmission and introduces much less motion oscillation. Therefore, the transmitted torque τ in transmission is selected as the objective function. Figure 5.4 illustrates a simplified model of transmission considering damping of input shaft and output shaft d_{t1} and d_{t2}. Each gear shaft in the transmission is modeled mathematically with respect to the transmitted torque τ as follows:

$$J_{t1}\ddot{\theta}_m = u - d_{t1}\dot{\theta}_m - \tau \tag{5.15}$$

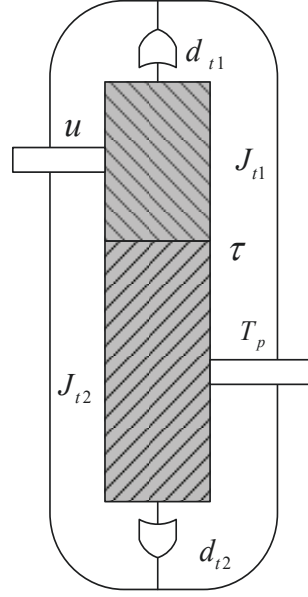$$J_{t2}\ddot{\theta}_t = i_g\tau - d_{t2}\dot{\theta}_t - T_p \tag{5.16}$$

Figure 5.4 Simplified Transmission Model

Combine with the Equation (2.50), above equations can be transformed into

$$u - d_{t1}\dot{\theta}_m - \tau = \frac{J_{t1}}{\dfrac{J_t}{i_t^2} + \dfrac{J_f}{i_t^2 i_f^2}}\left[u - \left(\dfrac{d_t}{i_t^2} + \dfrac{d_f}{i_t^2 i_f^2}\right)\dot{\theta}_m - \dfrac{k\left(\dfrac{\theta_m}{i_t i_f} - \theta_w\right)}{i_t i_f} - \dfrac{d\left(\dfrac{\dot{\theta}_m}{i_t i_f} - \dot{\theta}_w\right)}{i_t i_f}\right] \quad (5.17)$$

Which can be further transformed into state equation:

$$\tau = \boldsymbol{M}_s \boldsymbol{x} + D_s u \qquad (5.18)$$

Where $\boldsymbol{M}_s = \begin{pmatrix} \dfrac{J_{t1}k}{J_1 i_t i_f} & -\dfrac{J_{t1}d}{J_1 i_t i_f} & \dfrac{J_{t1}\left(d_1 + \dfrac{d}{i_t^2 i_f^2}\right)}{J_1} - d_{t1} \end{pmatrix}$, $D_s = 1 - \dfrac{J_{t1}}{J_1}$, and others are identical

to those in Chapter 2. Furthermore, relationships of J_t, J_{t1}, J_{t2} and d_t, d_{t1}, d_{t2} are expressed

as follows:

$$J_t = i_t^2 J_{t1} + J_{t2} \qquad (5.19)$$

$$d_t = i_t^2 d_{t1} + d_{t2} \qquad (5.20)$$

The objective of the control system is to minimize deviation between torque τ transmitted

in transmission and desirable reference value, and should be reduced to zero before gear

change begins to ensure shifting can be realized smoothly and quickly. Therefore, the cost

function should be extended as Equation (5.21), where η_s is introduced as a trade-off between response time and overshoot or oscillation, it is the variable to be optimized.

$$\lim_{T\to\infty}\int_0^T \tau^2 + \eta_s \left(u - u_{\text{shift}}\right)^2 dt \qquad (5.21)$$

From Equation (5.15) τ can be expressed as a function of wheel speed as follows:

$$\tau = u - d_{t1} i\dot{\theta}_w - J_{t1} i\ddot{\theta}_w \qquad (5.22)$$

Combine with Equation (5.23), the rigid differential equation of drive shaft, performance output τ can be derived as Equation (5.24).

$$(J_1 i + \frac{J_2}{i})\ddot{\theta}_w = u - d_1 i\dot{\theta}_w - \frac{l}{i} \qquad (5.23)$$

$$\tau = \left[1 - \frac{(J_m + J_{t1})i^2}{J_1 i^2 + J_2}\right]u - \left[d_{t1}i - \frac{(J_m + J_{t1})i}{J_1 i^2 + J_2}\left(d_1 i^2 + d_2\right)\right]\dot{\theta}_w + \frac{(J_m + J_{t1})i}{J_1 i^2 + J_2}l \qquad (5.24)$$

Therefore, u_{shift} can be derived as in Equation (5.25) by setting $\tau = 0$:

$$u_{\text{shift}} = \mu_x \dot{\theta}_w + \mu_l l \qquad (5.25)$$

Where $\mu_x = (d_{t1}i - \frac{J_{t1}i}{J_1 i^2 + J_2}d_1 i^2)[1 - \frac{J_{t1}i^2}{J_1 i^2 + J_2}]^{-1}$, $\mu_l = -\frac{J_{t1}i}{J_1 i^2 + J_2}[1 - \frac{J_{t1}i^2}{J_1 i^2 + J_2}]^{-1}$.

Thus, Equation (5.21) can be transformed into Equation (5.26), the ultimate active control objective:

$$\lim_{T\to\infty}\int_0^T \tau^2 + \eta_s \left[u - u_{\text{shift}}\left(\dot{\theta}_w, l\right)\right]^2 dt$$
$$= \lim_{T\to\infty}\int_0^T \left(M_s x + D_s u\right)^2 + \eta_s \left(u - \mu_x \dot{\theta}_w - \mu_l l\right)^2 dt \qquad (5.26)$$

However, the Equation (5.14) is an affine system because of the constant term l, in order to obtain an optimal feedback unit based on LQG algorithm, Equation (5.14) should be linearized in the area near the equilibrium point, and the linearized state space equation is given as follows:

$$\Delta\dot{x} = A\Delta x + B\Delta u \qquad (5.27)$$

Where $\Delta x = x - x_0$, $\Delta u = u - u_0$, $x_0 = x_0\left(x_{20}, l\right)$, $u_0 = u_0\left(x_{20}, l\right)$, x_{20} and u_0 are the initial values of x_2 and u, respectively, which are shown in Equation (5.28). Consider the

Equation (5.18), Equation (5.26) can be transformed into Equation (5.29).

$$u_0\left(\dot{\theta}_w, l\right) = \left(\begin{array}{cc} \dfrac{\left(d_1 i^2 + d_2\right)}{i} & \dfrac{1}{i} \end{array}\right)\left(\begin{array}{c} \dot{\theta}_w \\ l \end{array}\right) \triangleq \lambda_x \dot{\theta}_w + \lambda_l l, \quad x_0\left(\dot{\theta}_w, l\right) = \left(\begin{array}{cc} \dfrac{d_2}{k} & \dfrac{1}{k} \\ 1 & 0 \\ i & 0 \end{array}\right)\left(\begin{array}{c} \dot{\theta}_w \\ l \end{array}\right) \triangleq \delta_x \dot{\theta}_w + \delta_l l \ (5.28)$$

$$\lim_{T\to\infty}\int_0^T \left(M_s \Delta x + D_s \Delta u + M_s x_0 + D_s u_0\right)^2 + \eta_s \left(\Delta u - \mu_x \Delta x_2 + u_0 - \mu_x x_{20} - \mu_l l\right)^2 \mathrm{d}t$$

$$= \lim_{T\to\infty}\int_0^T \left(M_s \Delta x + D_s \Delta u + r_1\right)^2 + \eta_s \left(\Delta u - \mu_x \Delta x_2 + r_2\right)\mathrm{d}t$$
(5.29)

Where $r_1 = M_s x_0 + D_s u_0$, $r_2 = u_0 - \mu_x x_{20} - \mu_l l$. Based on Equation (5.14), model of

drivetrain is augmented into Equation (5.30), where should σ be small enough so that $r_{1,2}$

is a slow-varying value, i.e. $\dot{r}_1 = -\sigma r_1$, $\dot{r}_2 = -\sigma r_2$, and the linearized system will be stable

[150].

$$A_r = \left(\begin{array}{ccccc} & & & 0 & 0 \\ & A & & 0 & 0 \\ & & & 0 & 0 \\ \hline 0 & 0 & 0 & -\sigma & 0 \\ 0 & 0 & 0 & 0 & -\sigma \end{array}\right), B_r = \left(\begin{array}{c} B \\ \cdots \\ 0 \\ 0 \end{array}\right), x_r = \left(\begin{array}{c} \Delta x \\ r_1 \\ r_2 \end{array}\right) \tag{5.30}$$

Similarly, the cost function (5.29) can is augmented as

$$\lim_{T\to\infty}\int_0^T \left(x_r^{\mathrm{T}} Q_s x_r + R_s \Delta u^2 + 2 x_r^{\mathrm{T}} N_s \Delta u\right)\mathrm{d}t \tag{5.31}$$

Where $Q_s = \left(\begin{array}{ccc} M_s & 1 & 0\end{array}\right)^{\mathrm{T}}\left(\begin{array}{ccc} M_s & 1 & 0\end{array}\right) + \eta_s \left(\begin{array}{ccccc} 0 & -\mu_x & 0 & 0 & 1\end{array}\right)^{\mathrm{T}}\left(\begin{array}{ccccc} 0 & -\mu_x & 0 & 0 & 1\end{array}\right)$,

$R_s = \eta_s$, $N_s = \left(\begin{array}{ccc} M_s & 1 & 0\end{array}\right)^{\mathrm{T}} D_s + \eta_s\left(\begin{array}{cccc} 0 & -\mu_x & 0 & 0 & 1\end{array}\right)^{\mathrm{T}}$.

In order to minimize the Equation (5.31), the optimal feedback unit can be obtained as

the following equation based on LQG algorithm.

$$K_{sc} = Q_s^{-1}\left(B_r^{\mathrm{T}} P_{sc} + N_s^{\mathrm{T}}\right) \tag{5.32}$$

Where P_{sc} is the solution of Riccati equation as follows:

$$A_r^{\mathrm{T}} P_{sc} + P_{sc} A_r + R_s - \left(P_{sc} B_r + N_s\right) Q_s^{-1}\left(P_{sc} B_r + N_s\right)^{\mathrm{T}} = 0 \tag{5.33}$$

The control signal Δu can be obtained according to the optimal gain $\boldsymbol{K}_{sc}$:

$$\Delta u = -\boldsymbol{K}_{sc}\boldsymbol{x}_r = -\begin{pmatrix} K_{sc1} & K_{sc2} & K_{sc3} \end{pmatrix}\Delta \boldsymbol{x} - K_{sc4}r_1 - K_{sc5}r_2 \tag{5.34}$$

Therefore, the output of the controller, i.e. torque command of the motor u, can be obtained ultimately as follows:

$$u = K_{s0}\boldsymbol{x}_{20} + K_{sl}l - \begin{pmatrix} K_{sc1} & K_{sc2} & K_{sc3} \end{pmatrix}\boldsymbol{x} \tag{5.35}$$

Where $K_{s0} = (1 - K_{sc4}D_s - K_{sc5})\lambda_x + \begin{pmatrix} K_{sc1} & K_{sc2} & K_{sc3} \end{pmatrix}\delta_x - K_{sc4}\boldsymbol{M}_s\delta_x + K_{sc5}\mu_x$,

$K_{sl} = (1 - K_{sc4}D_s - K_{sc5})\lambda_l + \begin{pmatrix} K_{sc1} & K_{sc2} & K_{sc3} \end{pmatrix}\delta_l - K_{sc4}\boldsymbol{M}_s\delta_l + K_{sc5}\mu_l$,

$\lambda_x = (d_1i^2 + d_2)/i$, $\delta_x = \begin{pmatrix} d_2/k & i & 1 \end{pmatrix}^{\mathrm{T}}$, $\lambda_l = 1/i$, $\delta_l = \begin{pmatrix} 1/k & 0 & 0 \end{pmatrix}^{\mathrm{T}}$.

5.3.2 Optimal Control of Motor Torque Loading for Launch

The EV powertrain model of motor control during launch is identical to Equation (5.14) in 5.3.1, the control objective is aiming to compute an optimal motor torque output after driver's tip in/out so that deviation between motion states in drivetrain and desired state r_{ref} is compensated or offset and oscillations are attenuated too. Because the wheel speed z is convenient to be measured, and it relates to longitudinal impact to passengers, it is selected to constitute the cost function to minimize the motion state $\dot{\theta}_w - r_{ref}$. Since fast response of motor torque output may bring overshoot and oscillations, deviation between the control signal u and corresponding steady state u_0 is taken into consideration, therefore, the cost function is designed as (5.37).

$$z = \dot{\theta}_w = \boldsymbol{M}_t\boldsymbol{x} \tag{5.36}$$

$$\lim_{T\to\infty}\int_0^T \left(z - r_{ref}\right)^2 + \eta_t\left(u - u_0\left(r_{ref},l\right)\right)^2 dt \tag{5.37}$$

Where $\boldsymbol{M}_t = \begin{bmatrix} 0 & 1 & 0 \end{bmatrix}$, r_{ref} is the desired speed of driver's command, η_t is trade off between response time and overshoot or oscillation, it is the variable to be optimized. The steady state u_0 is function of desired speed and load, when the command signal is u_0 the equilibrium point $z = r_{ref}$ will be reached in the system, steady state condition of the

system is identical to Equation (5.28) in 5.3.1.

Similar to 5.3.1, designing of the LQG controller still needs linearization of the state equation, and after that the cost function (5.37) can be transformed into:

$$\lim_{T \to \infty} \int_0^T \left(M_t \Delta x + r_1 \right)^2 + \eta_t \left(\Delta u - r_2 \right)^2 dt \qquad (5.38)$$

Where $r_1 = M_t x_0 - r_{ref}$, $r_2 = u_0 - u_0 \left(r_{ref}, l \right)$. And after augmenting as in (5.30) in 5.3.1 for the state equation (5.14), the cost function can be transformed into:

$$\lim_{T \to \infty} \int_0^T \left(x_r^T Q_t x_r + R_t \Delta u^2 + 2 x_r^T N_t \Delta u \right) dt \qquad (5.39)$$

Where $Q_t = \left(M_t \quad 1 \quad 0 \right)^T \left(M_t \quad 1 \quad 0 \right) + \eta_t \left(0 \quad 0 \quad 0 \quad 0 \quad 1 \right)^T \left(0 \quad 0 \quad 0 \quad 0 \quad 1 \right)$, $R_t = \eta_t$,

$N_t = \eta_t \left(0 \quad 0 \quad 0 \quad 0 \quad 1 \right)^T$. The cost function (5.39) can be realized by the compensating control command Δu, $\Delta u = -K_{tc} x_r \triangleq -\left(K_{tc1} \quad K_{tc2} \quad K_{tc3} \quad K_{tc4} \quad K_{tc5} \right) \Delta x$, where

$K_{tc} = Q_t^{-1} \left(B_r^T P_{tc} + N_t^T \right)$ and P_{tc} is solution of the Riccati equation as follows:

$$A_r^T P_{tc} + P_{tc} A_r + R_t - \left(P_{tc} B_r + N_t \right) Q_t^{-1} \left(P_{tc} B_r + N_t \right)^T = 0 \qquad (5.40)$$

Therefore, the optimal motor control law of active damping control during speeding up/down is obtained:

$$u = K_{t0} x_{20} + K_{tl} l + K_{tr} r_{ref} - \left(K_{tc1} \quad K_{tc2} \quad K_{tc3} \right) x \qquad (5.41)$$

Where $K_{t0} = \left(K_{tc1} \quad K_{tc2} \quad K_{tc3} \right) \delta_x - K_{tc4} M_t \delta_x + \lambda_x - K_{tc5} \lambda_x$, $K_{tr} = K_{tc4} + K_{tc5} \lambda_x$,

$K_{tl} = \left(K_{tc1} \quad K_{tc2} \quad K_{tc3} \right) \delta_l - K_{tc4} M_t \delta_l + \lambda_l$.

5.3.3 Active Damping Controller with Off-line QGA Optimization Unit

In designing of the LQG controller selection of the weight η is quite important which influences the control law directly. In this chapter an LQG active damping controller with quantum genetic algorithm is proposed to search the optimal weight parameter η objectively rather than subject selection by designers so that actual optimal control performance can be realized.

In order to drive the drivetrain with less oscillation in drivetrain, root mean square of motor speed, torsional angle and rotary speed of drive shaft are introduced to constitute the fitness function, as their unit and magnitude are different, so the above three indexes should be normalized to be the fitness function f, which is designed as

$$\text{minimize} \quad f = \frac{\sqrt{\dfrac{\sum_{j=1}^{j=N_1} x_{1j}^2(\eta)}{N_1}}}{\sqrt{\dfrac{\sum_{j=1}^{j=N_1} x_{1j\text{pass}}^2}{N_1}}} + \frac{\sqrt{\dfrac{\sum_{j=1}^{j=N_2} x_{2j}^2(\eta)}{N_2}}}{\sqrt{\dfrac{\sum_{j=1}^{j=N_2} x_{2j\text{pass}}^2}{N_2}}} + \frac{\sqrt{\dfrac{\sum_{j=1}^{j=N_3} x_{3j}^2(\eta)}{N_3}}}{\sqrt{\dfrac{\sum_{j=1}^{j=N_3} x_{3j\text{pass}}^2}{N_3}}} \qquad (5.42)$$

$$\text{s.t.} \quad \begin{cases} 0.001 \le \eta \le 100 \\ x_1(\eta) < x_{1\text{pass}} \\ x_2(\eta) < x_{2\text{pass}} \\ x_3(\eta) < x_{3\text{pass}} \end{cases} \qquad (5.43)$$

Where $N_i\ (i=1,2,3)$ is number of the sample points, $x_i(\eta)$ is a drivetrain state corresponds to the current η, $x_{i\text{pass}}$ is the corresponding state in open loop system, which is obtained and sampled from simulation of corresponding passive system. For the passive underdamped condition, response $c(t)$ of the second order system to step input signal is as the Equation (5.44), where $\omega_d = \omega_n \sqrt{1-\zeta^2}$ is the damped oscillation frequency, $\theta = \arctan \dfrac{\sqrt{1-\zeta^2}}{\zeta}$ is the phase angle.

$$\begin{aligned} c(t) &= 1 - e^{-\zeta\omega_n t}\left(\cos\sqrt{1-\zeta^2}\,\omega_n t + \frac{\zeta}{\sqrt{1-\zeta^2}}\sin\sqrt{1-\zeta^2}\,\omega_n t \right) \\ &= 1 - \frac{e^{-\zeta\omega_n t}}{\sqrt{1-\zeta^2}}\sin\left(\sqrt{1-\zeta^2}\,\omega_n t + \arctan\frac{\sqrt{1-\zeta^2}}{\zeta} \right) \\ &= 1 - \frac{e^{-\zeta\omega_n t}}{\sqrt{1-\zeta^2}}\sin\left(\omega_d t + \theta \right) \end{aligned} \qquad (5.44)$$

From the above equation it can be deduced that amplitude of oscillation in drivetrain only relates to the system inherent parameters, and is independent to input. Therefore, it is reasonable and objective to select $x_{i\text{pass}}$ as the normalization factor.
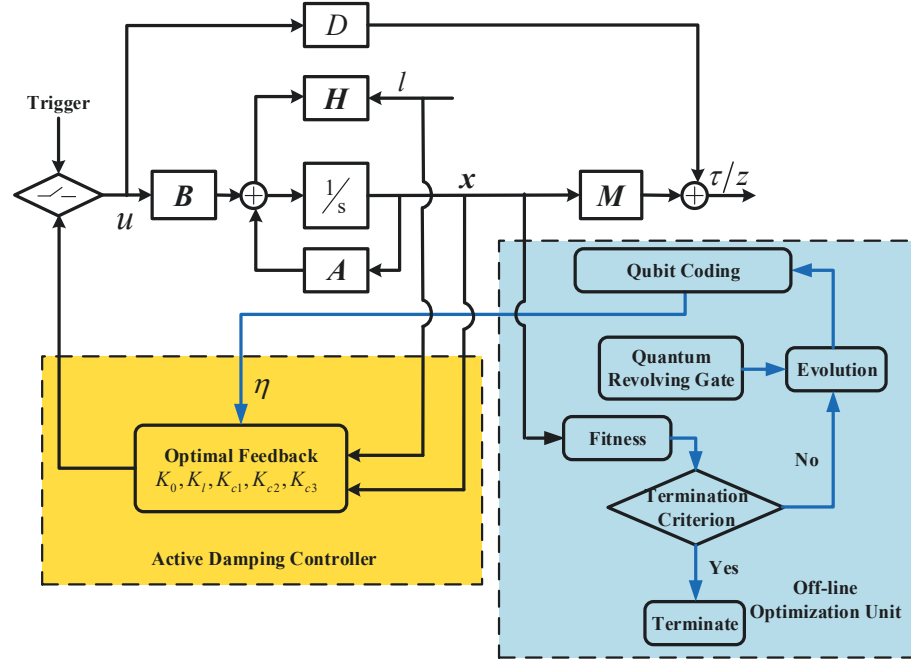
Figure 5.5 Structure of the Joint Control Algorithm with QGA Off-line

Figure 5.5 shows the structure of the proposed joint optimal control algorithm, it collects state variables $x_i(\eta)$ with current weight η in the controller to calculate the current fitness, and then it will revolute by quantum revolving gate to search a better η, such that the fitness function will get closer to the minimum. Considering the calculation speed of rolling online optimization is far from enough to meet requirements of vibration control, therefore, the optimization is completed off-line and save a group of η corresponding to variable of parameters of the system.

5.4 Simulation Test

The powertrain physical model is established in AMEsim as shown in Figure 5.6, which includes a PMSM, a transmission, a final drive, an elastic drive shaft, equivalent moment of inertia of multi-bodies, several sensors and a controller. Parameters in the simulation are given in Table 5.2 and define of the parameters is identical to that in 5.3. The control law in the AMEsim controller is calculated with the optimized weight η by Matlab.
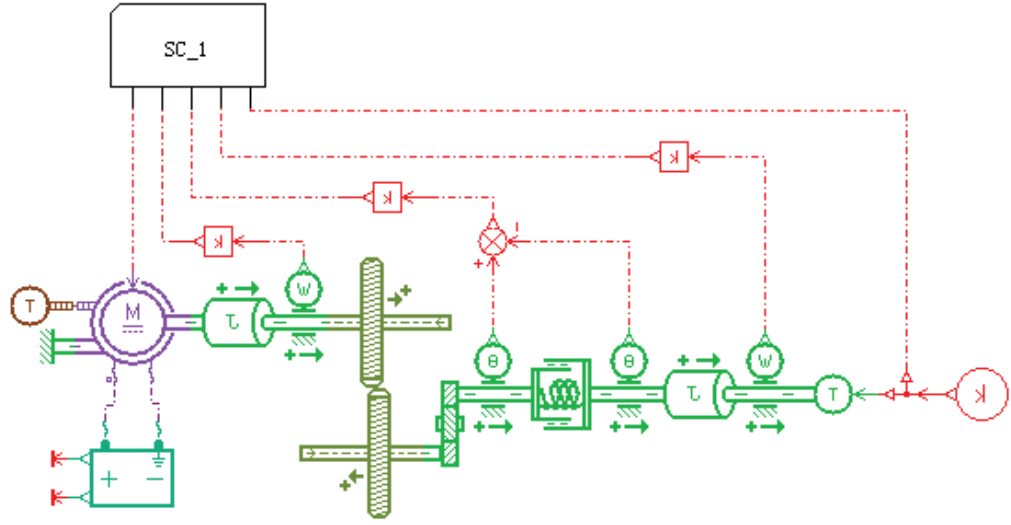
Figure 5.6 Electric Vehicle Powertrain Model in AMEsim

Table 5.2 Main Parameters of Drivetrain for Simulation

Parameters	Value	Parameters	Value
Vehicle Mass m	1500kg	Damping d_1	0.2 Nm/(rad/s)
Wheel Radius r_w	0.29m	Damping d_2	31.17 Nm/(rad/s)
Gear Ratio $i_t i_f$	3.45×4.831	Motor Moment of Inertia J_m	0.05kgm²
Drive Shaft Equivalent Torsional Stiffness k	246371Nm/rad	Moment of Inertia J_1	0.0105 kgm²
Drive Shaft Equivalent Torsional Damping d	9.549Nm/(rad/s)	Moment of Inertia J_2	128.15 kgm²

5.4.1 Torque Unloading Phase

Based on the above parameters configuration, 100 generations of evolution in Matlab is completed as in Figure 5.7 so that the optimal weight parameter η_{sbest} =9.5486 is obtained, and further parameters constituting the control law for motor torque are obtained:

K_{s0}=6.58×10^{-7}, K_{sl}=−0.0054, K_{sc1} = −4556.89, K_{sc2} = −43.41, K_{sc3} = 2.42.

Optimal Value: 0.420019 Mean Value: 0.420427
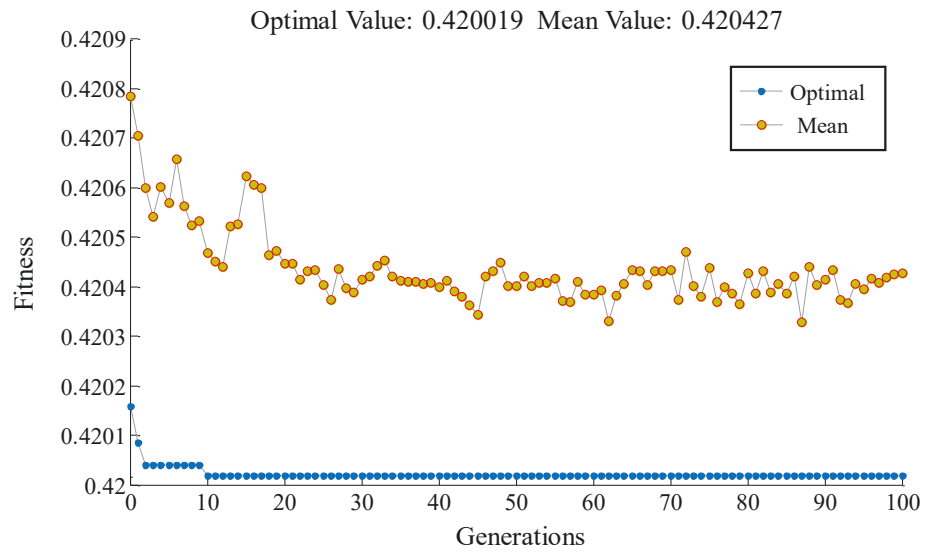
Figure 5.7 Evolution of the Fitness

In the simulation test, the motor receives command of reducing torque output for shifting at the 3rd second. Suppose that the PMSM can be controlled accurately and inertia of the rotor is taken into consideration, there is deviation between the actual motor torque output and torque command, therefore, the actual motor torque output complying to the control law and considering deviation is illustrated in Figure 5.8, rather than a step unloading.
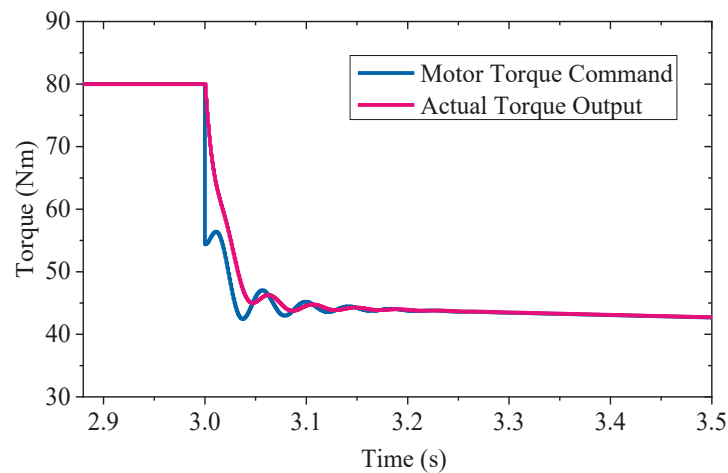
Figure 5.8 Motor Torque Output Under Optimal Control Law
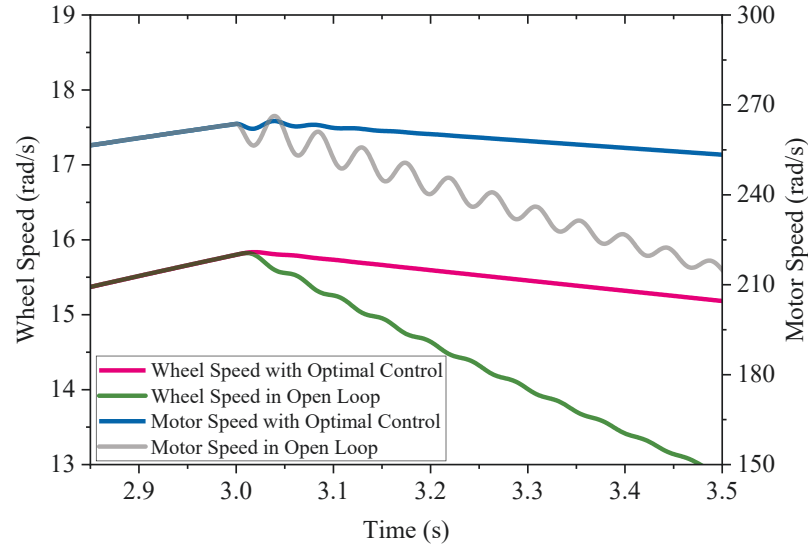
Figure 5.9 Control Performance of the Drivetrain
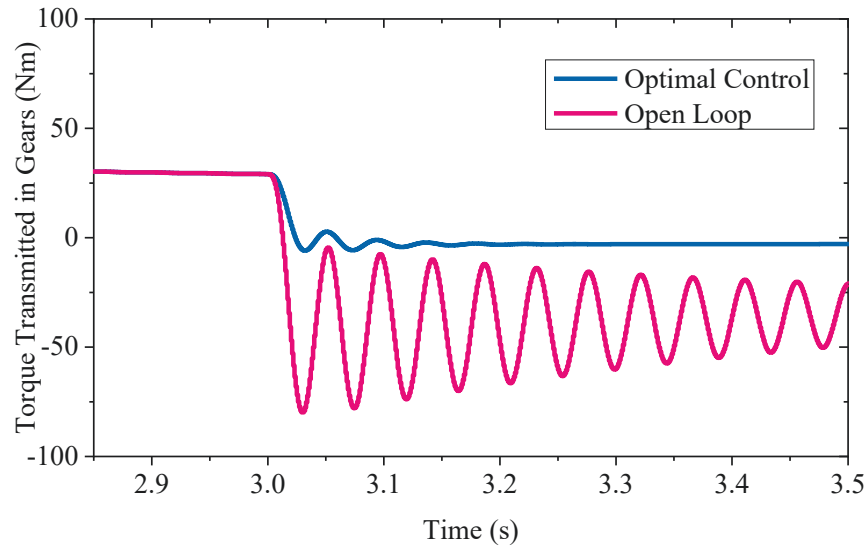
Figure 5.10 Torque Transmitted in the Gears of Transmission

Under the optimal control as the torque command, the motion states of EV drivetrain react as in Figure 5.9. In order to compare the control performance, open loop control is introduced, i.e. unload motor torque step to 0 directly. Suppose that the motor starts to decrease torque output from 80Nm and oscillations come about in both motor rotor and wheel speed. From Figure 5.9 and 5.10 it can be seen that the oscillations in drivetrain under QGA-LQG joint control is attenuated obviously comparing with motor torque step unloading to 0 directly. Furthermore, because of reaction from the driven gear in

transmission, the torque transmitted in the gears will not be 0 actually as in Figure 5.10 if totally cut down the driving torque input, it may bring abrasion on teeth; but with the optimal control the transmitted torque in gears will actually reduce to 0 as motor torque decreasing dynamically, so that the meshed gear and sleeve can be detached at this moment and abrasion will be reduced as well.

No matter it is LQG or other model-based algorithms, a main challenge is the accuracy in modeling. Since uncertainties from errors in modeling and disturbance from signal processing or powertrain working condition will influence the stability of controller, stability and sensitivity are analyzed for the optimal controller as in Figures 5.11-5.14. Because wheel speed oscillation directly brings longitudinal shuffle of vehicle, wheel speed is selected as the feedback signal C_w, $C_w = \begin{pmatrix} 0 & 1 & 0 \end{pmatrix}$. Denote the transfer function of feedback to $F_y(s)$, $F_y(s) = K_c(sI - A + BK_c + C)$; denote the transfer function of PMSM control command u to wheel speed to $G_{uw}(s)$, $G_{uw}(s) = C_w(sI - A)^{-1}$; denote the function of PMSM control command u to transmitted torque in gears to $G_{uz}(s)$, $G_{uz}(s) = M(sI - A)^{-1}B + D$.
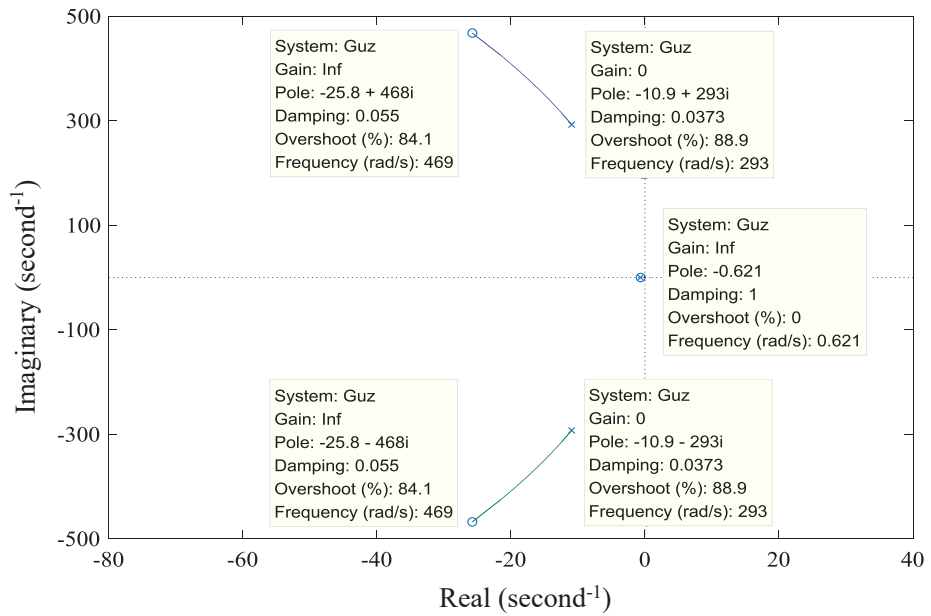

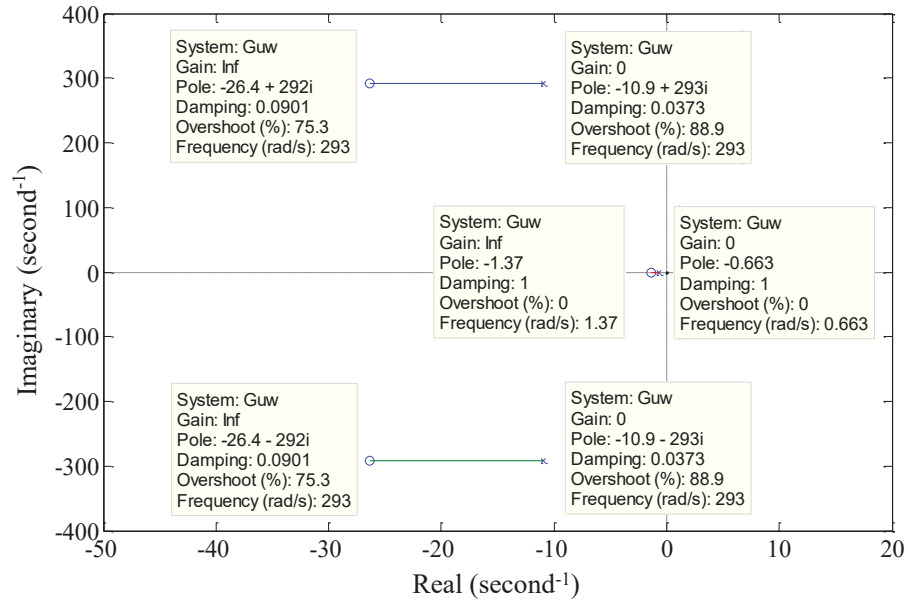Figure 5.11 Root Locus of the Drivetrain with Transmitted Torque Feedback

Figure 5.12 Root Locus of the Drivetrain with Wheel Speed Feedback

In Figure 5.11 and Figure 5.12 illustrate root locus of the system with transmitted toque feedback and wheel speed, respectively. It can be observed that when the feedback gain of corresponding to open loop system varies $0 \rightarrow \infty$, the root locus of both transfer functions are all in the negative part of the coordinate, according to the cybernetics the system is stable.
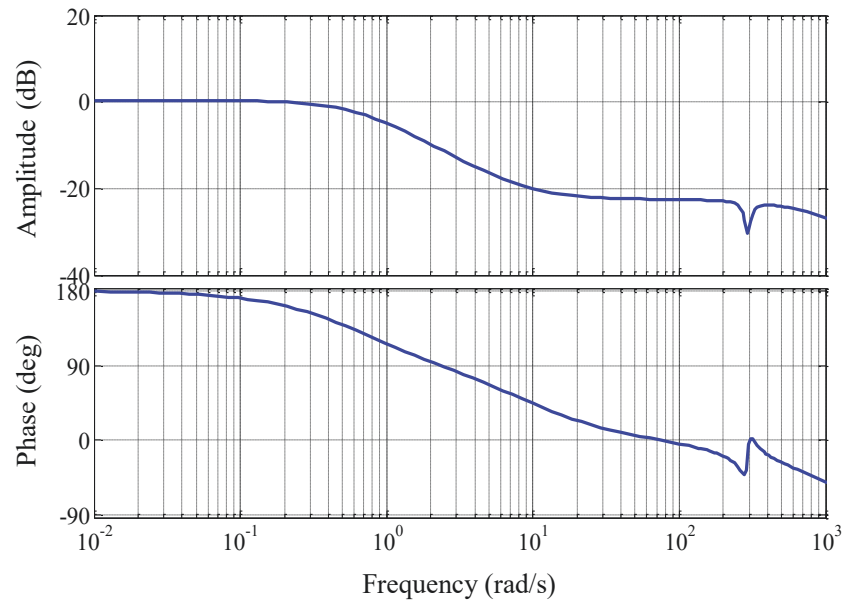
Figure 5.13 Sensitivity S_{ww} of Wheel Speed Response
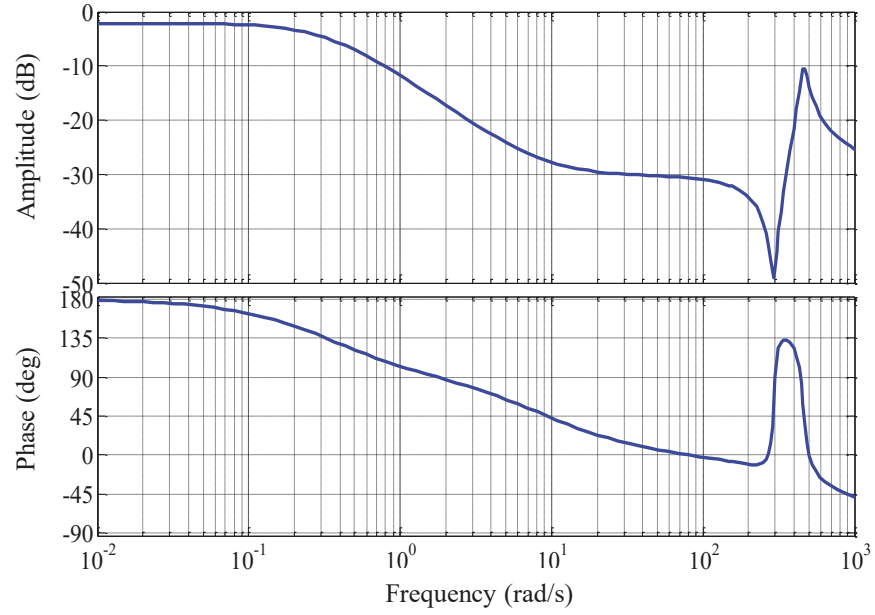
Figure 5.14 Sensitivity S$_{ww}$ of Transmitted Torque Response

Parameters variation or the input signal disturbed by noise will affect the response performance, which can be expressed by introducing the sensitivity S_w. Sensitivity corresponding to the two feedback is derived by following formula:

$$S_{ww} = \frac{1}{1+G_{uw}(s)F_y(s)} \tag{5.45}$$

$$S_{wz} = \frac{1}{1+G_{uz}(s)F_y(s)} \tag{5.46}$$

Where S_{ww} denotes sensitivity corresponding to wheel speed feedback, S_{wz} denotes sensitivity corresponding to transmitted torque feedback. From Figures 5.13-5.14 it can be seen that both feedback is not sensitive to low frequency and will not affect the control objectives a lot. As is all known, sensitivity is conflict to the response performance, high sensitivity requires accurate parameters of the plants, otherwise, the output may overshoot severely. Sensitivity of the closed loop system is usually less than that of corresponding open loop system so that stability is improved, that is just the advantage of the closed loop system.

5.4.2 Torque Increasing for Launch Phase

Parameters configuration is set identically to 5.4.1, 100 generations of evolution in Matlab is completed as in Figure 5.15 so that the optimal weight parameter $\eta_{tbest}=0.1004$ is obtained, and further parameters constituting the control law for motor torque are obtained: $K_{t0}=1.14\times10^{-4}$, $K_{tl}=0.0599$, $K_{tc1}=0.391$, $K_{tc2}=0.863$, $K_{tc3}=0.0012$, $K_{tr}=6.0885$.
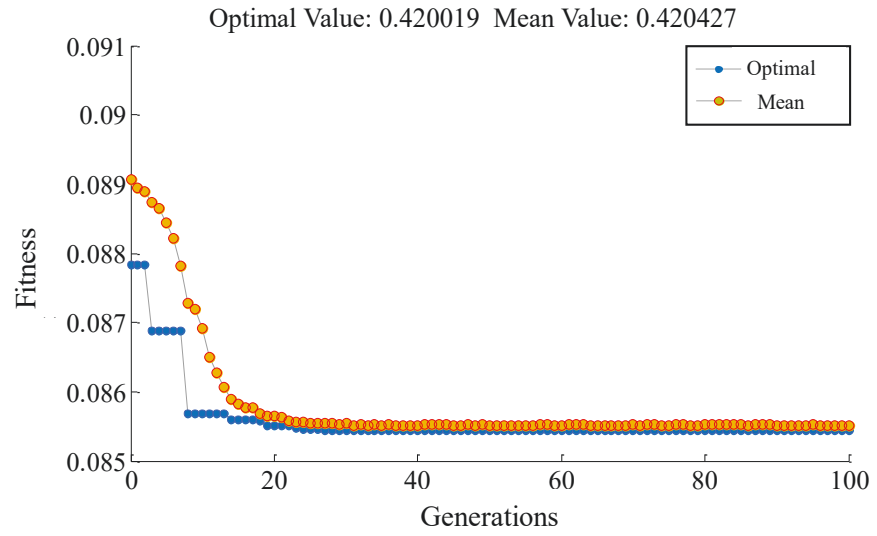
Optimal Value: 0.420019 Mean Value: 0.420427

Figure 5.15 Evolution of the Fitness

In simulation driver's tipping in and tipping out command are given in the 3rd and 7th seconds, respectively, in this period the PMSM outputs torque as in Figure 5.16 and corresponding wheel speed is illustrated in Figure 5.17. Conventional PID speed tuning control is introduced for comparison in the simulation, of which parameters are set t0 P=0.28, I=0.01, D=0.02; the PID collect speed signal to constitute a closed loop control system and by tuning motor torque output dynamically speed tracking can be realized. From Figure 5.17 it can be seen that both control algorithm can track the desired speed of no oscillations but the one with the proposed QGA-LQG joint optimal control can attenuate the torsional oscillation better. When tip in/out command is given by the driver, the wheel speed will vary more smoothly under the optimal control so that vehicle longitudinal shuffle will be reduced.
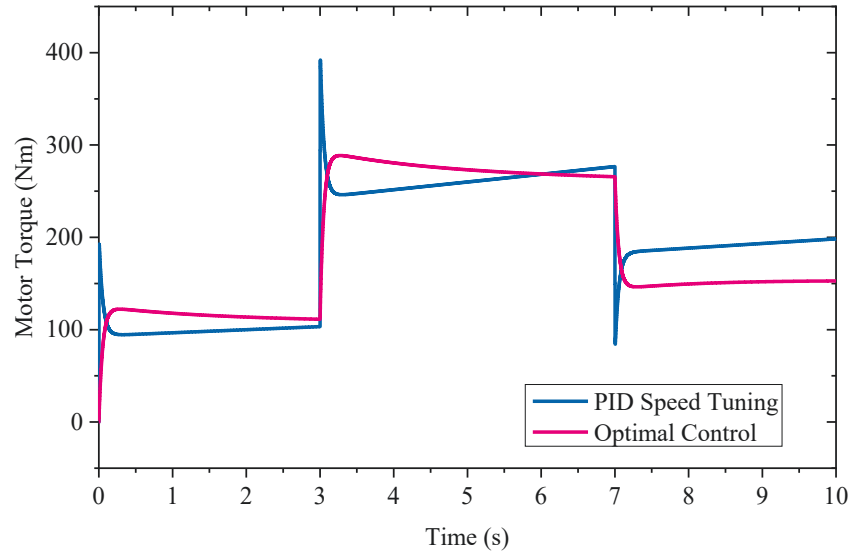
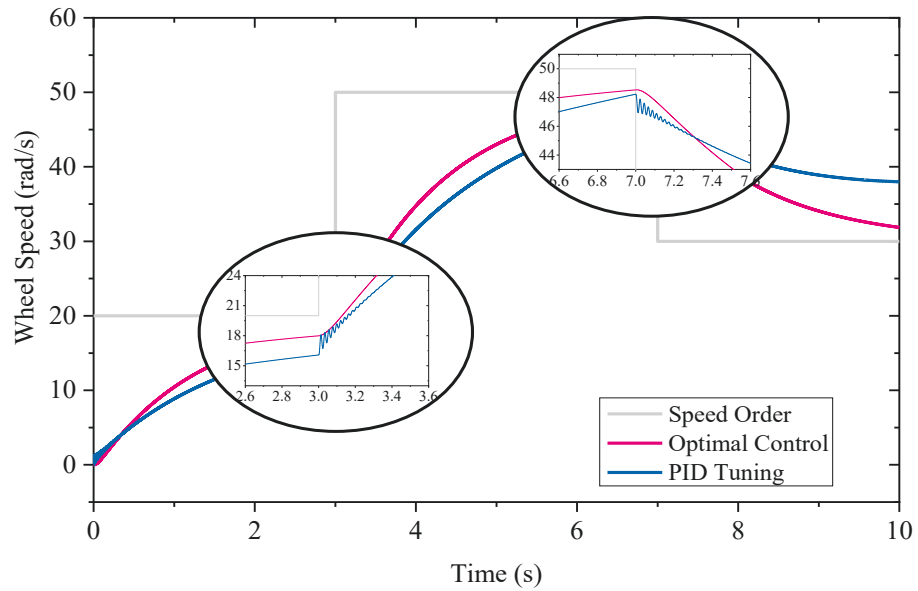Figure 5.16 Motor Torque Output of Control Laws

Figure 5.17 Control Performance of Wheel Speed During Acceleration

In the simulation of speed optimal control for launch the stability and sensitivity are analyzed as well, and selection of the transfer function Guw is identical to 5.4.1. Figure 5.18 illustrates that root locus of the system all locates at the negative part of the coordinate and the system is stable.

Sensitivity calculation of the speed control system with wheel speed as feedback and with motor torque as input is similar to 5.4.1, the Figure 5.19 illustrates that in low frequency scope the wheel speed is not sensitive to the input variation, it will not response
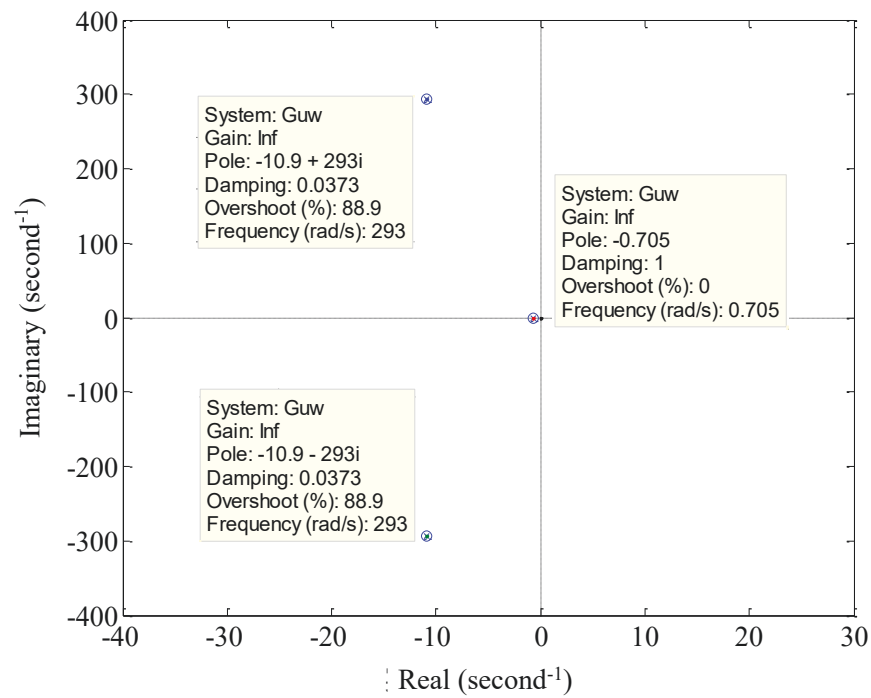
excessively to disturbance from the input.

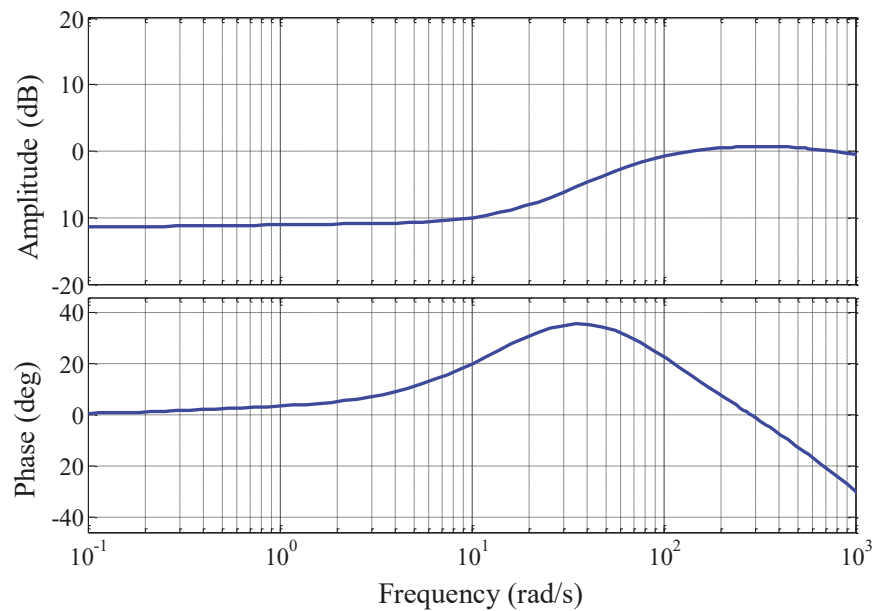Figure 5.18 Root Locus of the Speed Control System

Figure 5.19 Sensitivety of Wheel Speed Response

5.4 Summary

In this chapter a QGA-LQG joint active damping control for torsional oscillations in EV drivetrain is proposed. Quantum computing is introduced to the optimization and utilize the qubit coding to replace the binary code such that a chromosome can carry more information because of the superposition, interference and entanglement characteristics; and the conventional cross and mutation operation are replaced by quantum revolving gate, so that the parallel computing can accelerate optimization speed in searching the optimal parameters.

An LQG controller is designed to active damp the torsional oscillation with multi-feedback from drivetrain states. By off-line optimization with the QGA the optimal weight parameter in LQG controller is searched rather than subjective selection, such that actual optimal control performance is achieved.

CHAPTER 6: HARDWARE-IN-LOOP SIMULATION AND REAL VEHICLE EXPERIMENT

6.1 Introduction

The proposed parameter intelligent estimation, AASTW state observation and active damping control have been simulated by Matlab or AMEsim in previous text, one of the main advantage of simulation by commercial software is the convenience and short development cycle, and it is an evitable process in development and testing of all control system. But the simulation is just a primary stage of the whole system development, and it is not enough to transplant the model in simulation to real vehicle application. Usually, before the application to real vehicle there are experiments on test rigs and hardware-in-loop simulation. The main advantage of real vehicle experiment is it can reflect the real performance of the designed in vehicle practice but it costs a lot, consumes quite a long time and sometimes dangerous. Therefore, selection of the test type depends on the specific purpose and condition in this thesis.

In this chapter the proposed algorithms in Chapter 3, Chapter4 and Chapter 5 are tested. Real vehicle experiment was carried on for the nonlinear particle filter-based vehicle mass intelligent in Chapter 3, real vehicle-test rig experiment was carried out for AASTW-based drive shaft torque observation in Chapter 4, rapid prototype experiment was carried out for QGA-LQG joint active damping control for torsional oscillations in EV drivetrains.

6.2 Overview of the Rapid Prototype Experimental Platform

The rapid prototype experiments depend on dSPACE real time simulation system and a test rig with EV powertrain. The dSPACE real time simulation modules can be embedded in Simulink environment, it is a semi-physical simulation working platform and is widely used in automotive research and development due to good expandability, reliability and real-time performance. dSPACE real time simulation system mainly includes simulation

software such as ControlDesk, ModelDesk, MotionDesk and other hardware simulation platforms such as Micro AutoBox and dSPACE Simulator.

6.2.1 Software

1. ControlDesk

ControlDesk is dSPACE simulation tool which includes control and detection functions, seamlessly links to Simulink, and have access to vehicle CAN bus systems, such that rapid control of prototypes, hardware-in-the-loop simulation, VCU testing, calibration and diagnostics, and a range of virtual experiments can be realized. Figure 6.1 shows ControlDesk that integrates the commonly used functions that not only provides special tools connecting simulation platform and CAN bus, but also measurements, calibrations, and diagnostics on ECU.
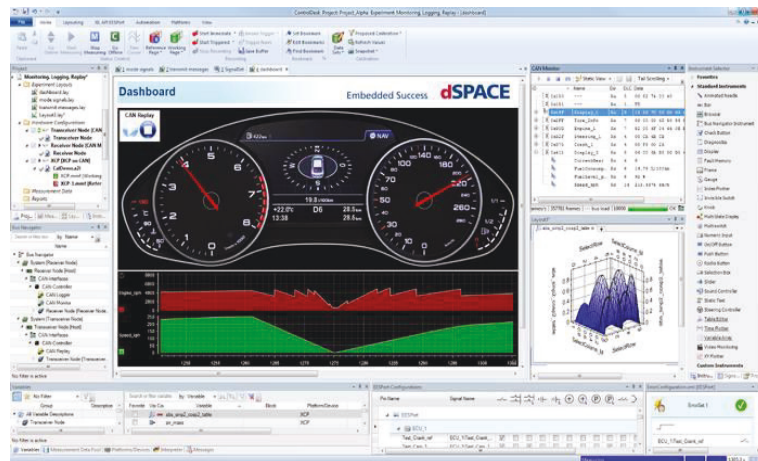

Figure 6.1 Interface of ControlDesk

2. ModelDesk

Figure 6.2 shows the ModelDesk that is used for simulation, graphical user interface for model parameterization and parameters management, and it is also used to perform major tasks before, during, and after the simulation; to realize seamless simulation from model-in-the-loop simulation to hardware-in-the-loop. In ModelDesk various parameters of the vehicle can be modified for more accurate simulation based on the intuitive parameterization of graphics and parameters management online or offline
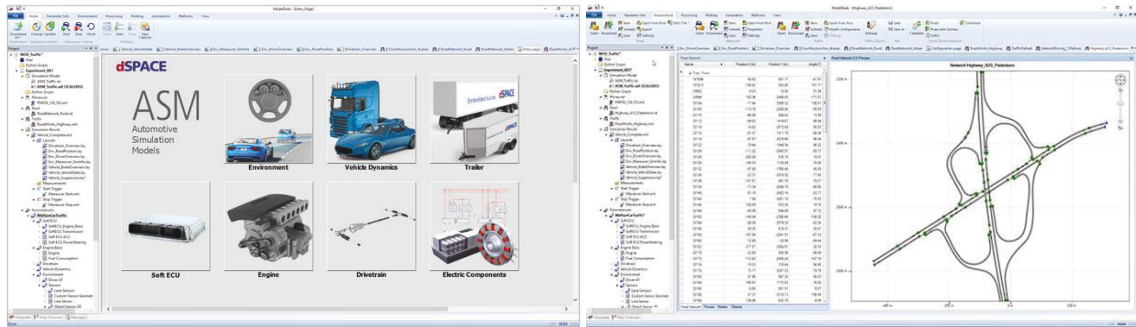
Figure 6.2 Interface of ModelDesk

ModelDesk-based simulations can manage parameters such as road routes, driving maneuvers, vehicle configuration, simulation results and all measured data so that simulations are easy to be reproduced, and offline and online simulations can be easily compared.

6.2.2 Hardware

1. Micro Autobox

Micro AutoBox is a real-time system for performing rapid functional prototype as in Figure 6.3, of which solid and compact design is ideal for vehicle utilities and is equipped with a comprehensive I/O interface including CAN, CAN FD, LIN, K-Line / L-Line, FlexRay, Ethernet and bypass interfaces, it can be programmed by Simulink. Micro AutoBox can be started automatically after power-on with startup time close to ECU and can be easily connected (hot-plugged) to a PC or laptop for program download, such that model parameterization and data analysis can be realized with Ethernet.

Figure 6.3 MicroAutobox

2. dSPACE Simulator

dSPACE Simulator is a hardware-in-the-loop simulator of dSPACE as in Figure 6.4, which is quite suitable for testing of EV powertrain, dynamics and ECU. It consists of a standard processor board and I/O board, which simplifies adjustments and modifications due to changes in project requirements. dSPACE Simulator can be used for ECU function and integrated test signal tuning, load simulation and electrical fault simulation, and it is open and extensible. dSPACE Simulator generates and measures I/O signals via integrated dSPACE I/O boards, and the function is complemented by load and fault simulation.

Figure 6.4 dSPACE Simulator

6.3 Experiment of Vehicle Mass Intelligent Parameter Estimation

In this section an experiment was carried on for the nonlinear particle filter-based vehicle mass estimation in Chapter 3, in this experiment 10.5m AUV electric bus of Beijing Foton Motor co. LTD as shown in Figure 6.5, of which main parameter is listed in Table 6.1.

Table 6.1 Parameters of Experimental Electric Bus

Parameter	Configuration	Parameter	Configuration
Kerb Mass	9900kg	Maximum Speed	69km/h
Length	10500mm	Motor Rated Power/Speed	100/1000(kw/r/min)
Tyre	275/70R22.5	Motor Peak Power/Speed	165/3000(kw/r/min)

Figure 6.5 Experiment for Vehicle Mass Estimation

In this experiment drag torque is obtained by free sliding, and during the low speed operation air drag is neglected. In the sliding experiment the electric bus is loading 50% rated mass and is accelerated to 65 km/h and then pedal is released totally, and then the bus begins to decrease in sliding until stops, during this period speed varying with time is recorded.
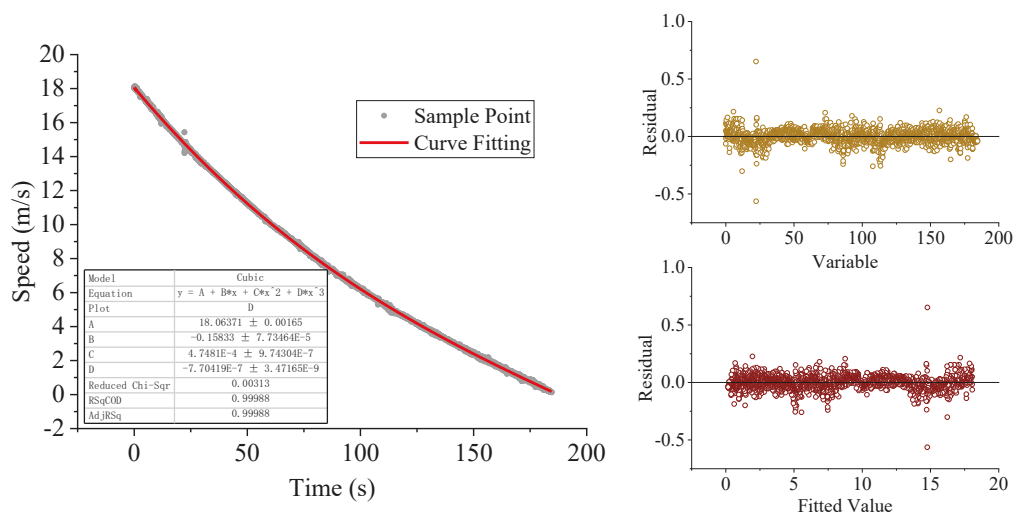

Figure 6.6 Fitting of the Sliding Speed

By polynomial fitting after unit conversion, a fitted curve is obtained as in Figure 6.6, the fitted sliding speed u with respect to time is obtained as follows:

$$u = 18.0637 - 0.1583t + 4.7481 \times 10^{-4} t^2 - 7.7042 \times 10^{-7} t^3 \tag{6.1}$$

And then take derivative of the above equation so that relationship of acceleration and time is obtained. By $T_f = r_w ma$ the fitted drag torque with respect to speed is obtained as Figure 6.7 and the corresponding fitting function as

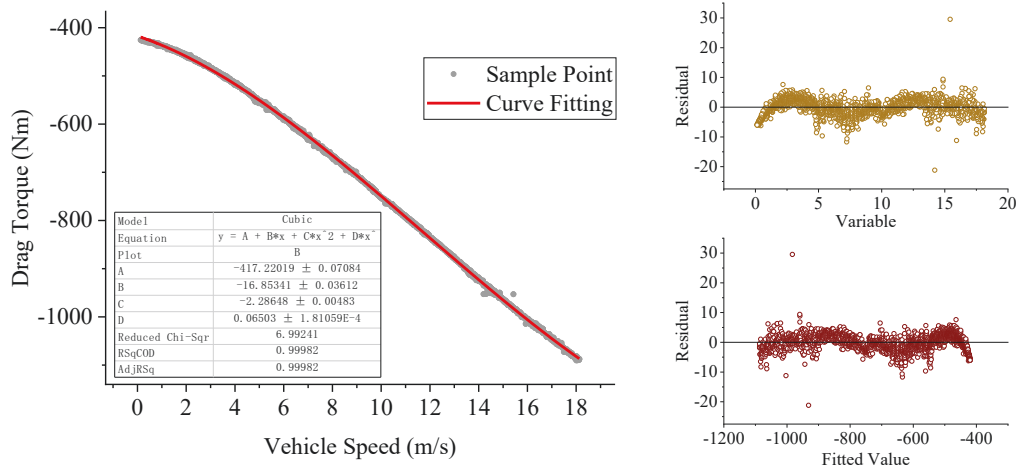$$T_f = -417.2202 - 16.8534u - 2.2865u^2 + 0.065 \tag{6.2}$$

Figure 6.7 Fitting of the Drag Torque and Vehicle Speed

Utilize the fitted drag torque with respect to vehicle speed to obtain the longitudinal force of vehicle, at the initial moment drive steps the pedal and keeps constant, and the bus keeps accelerating. The signals are read on CAN bus and filtered by a low-pass filter as the black line in Figure 6.8, which also illustrates other motion states and mass estimating performance.

The estimator downloaded in the rapid prototype is configured with systematic resampling, 1000 particles of which mean value are [0,8000] variance is diag ([100 10000000]), and 500ms sample time for reducing computing power consumption. In Figure 6.8 the dark blue line is vehicle mass estimation result in real time as the bus accelerating, in the first few seconds the estimated result converges towards the real mass and then some overshoot come about, but with the estimation going on with information increasing and updating the estimated result converges to the real value and keeps stable.
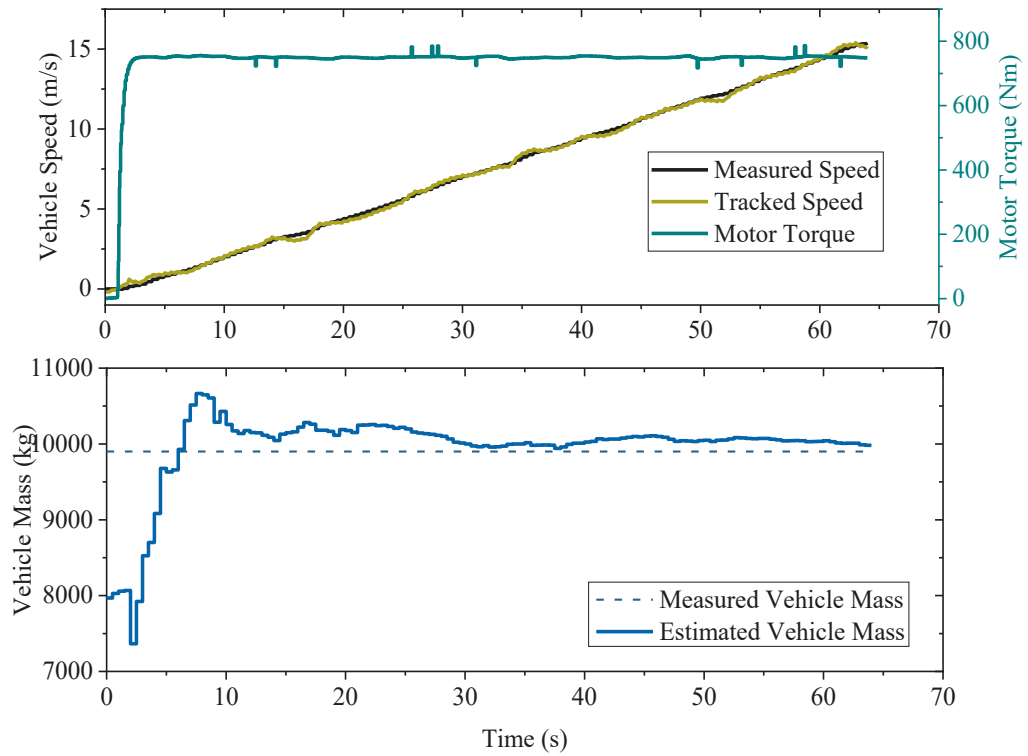
Figure 6.8 Performance of the Vehicle Mass Estimation

6.4 Experiment of Drive Shaft Torque Observation

Figure 6.9 Experiment for Drive Shaft Torque Observation

Configuration of this experiment is shown in Figure 6.9, and Chery electric SUV 3xe, the

drive shafts are connected to dynamometers by flanges, in the connections there are also

two torque sensors on each side. Control and monitor of the dynamometer and sensors are in the host computer on console. In order to simulate total drag torque in real road, drag torque is provided by the dynamometer, meanwhile, wheel speed is measured.

The main parameters of the experimental device are shown in Table 6.2. However, due to the limitations of the experimental conditions such as lack of CAN bus communication protocol, such that actual torque output of the motor cannot be measured. Therefore, according to the external characteristic map of the motor in Figure 6.10, the pedal is stepped on the bottom to output the maximum motor torque, and the actual motor torque output is approximately replaced by the maximum torque in the motor external characteristic map, so that the torque can be known.

Table 6.2 Parameters of Experimental Electric SUV

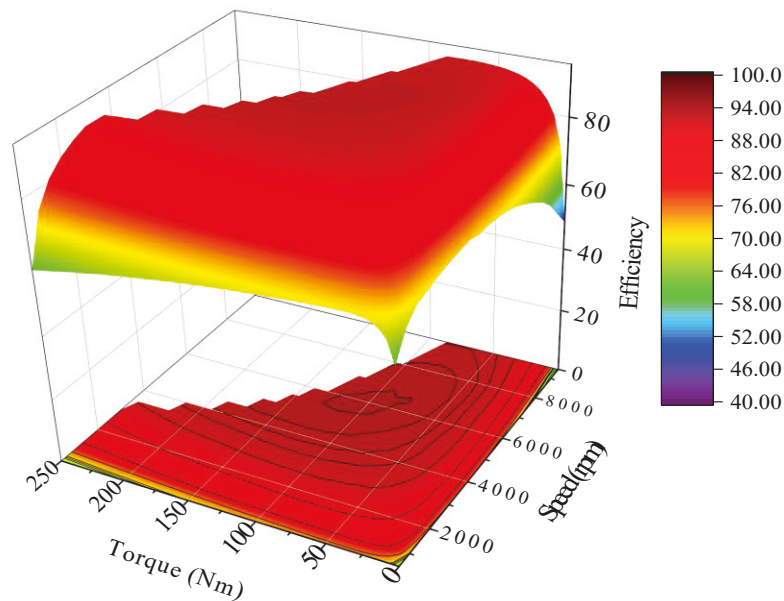| Parameter	Value
Maximum Motor Torque	276Nm
Maximum Motor Power	90kw
Motor Rated Power	46kw
Total Transmission Ratio (fixed)	9.11
Dynamometer Moment of Inertia	5.76kgm^2

Figure 6.10 PMSM External Characteristic Map

In the driving torque measurement, the resistance torque includes not only constant resistance torque from the dynamometer but also frictional drag torque and the inertia resistance. In this experiment, frictional drag torque and the inertia resistance are still obtained by acceleration measurement in free-sliding with sample time 1s. As fitted in Figure 6.11, the fitting function of drive shaft speed ω (rpm) with respect to time t(s) is:

$$\omega=642.3043-149.1685t+8.8986t^2 \tag{6.3}$$

After unit conversion and derivative calculation, by applying $T_f = J\dot{\omega}$ the fitted function of dynamometer frictional drag torque (Nm) with respect to speed (rpm) is obtained as Equation (6.4) and illustrated in Figure 6.12.

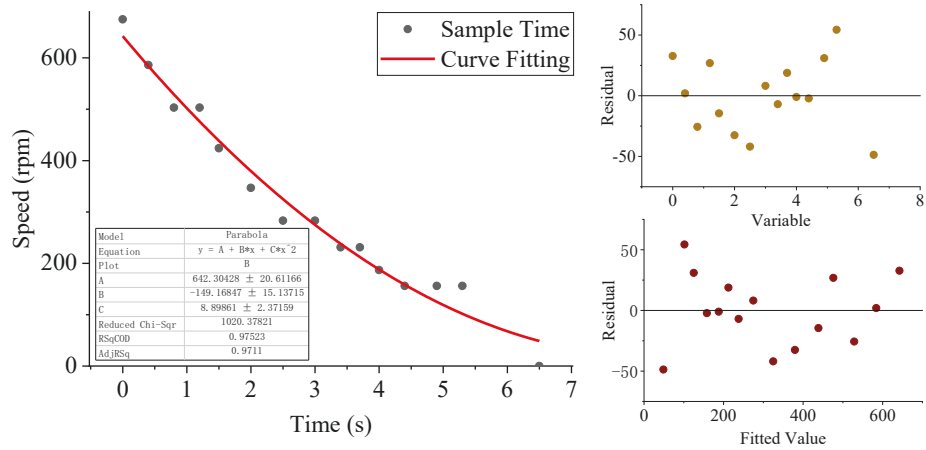$$T_f =-16.5412-0.1747\omega+9.6593\times10^{-5}\omega^2 \tag{6.4}$$
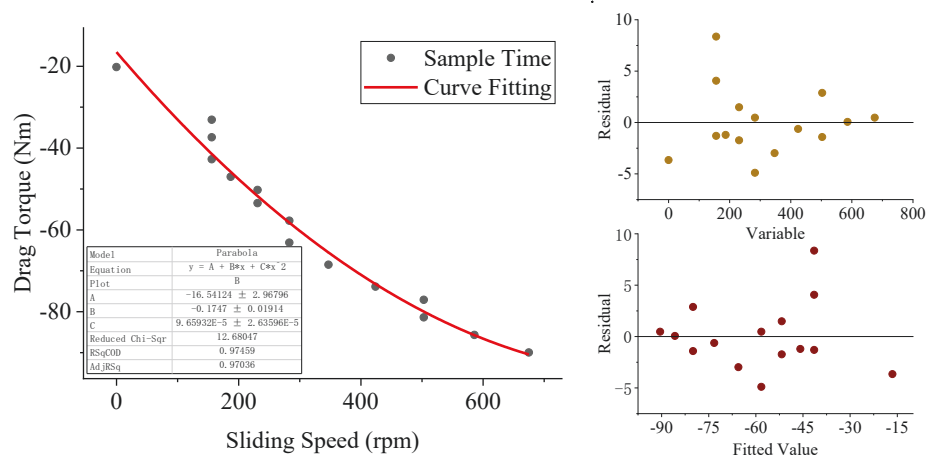

Figure 6.11 Fitting of the Sliding Speed

Figure 6.12 Fitting of the Drag Torque and Sliding Speed

In order to avoid the motor speed increasing exceedingly to get out of the external

characteristic map and to make the torque unknown after pedal is stepped on, a large resistance 750Nm from the dynamometer is given such that drive shaft speed will not be too fast and the motor torque output can be kept in 276Nm.

Set the sample time is 1s, step the pedal to the bottom after starting data measuring and then drive shaft speed increases as the brown line in Figure 6.13. After the speed is maintained constant for several seconds, the accelerator pedal is quickly released, then the drive shaft speed drops rapidly under the resistance from the dynamometer until it stops. Since there is no tire of low torsion stiffness, the drivetrain can be regarded rigid, therefore, the motor speed can be obtained by multiplying the measured drive shaft speed by transmission ratio. According to the drive shaft observer designed in 4.3, the observation is as the dark blue line in Figure 6.13. Because absence of the communication protocol and indirect measurement of motor torque and speed is not accurate enough, the actual motor torque is not 276Nm certainly, so that there is deviation between the measured torque and the observed torque.
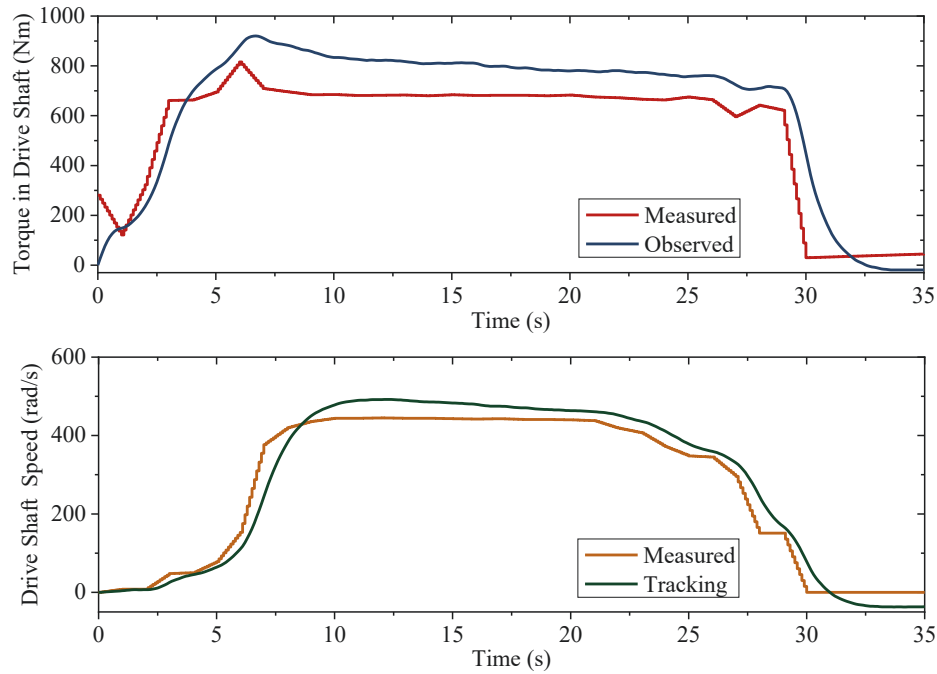

Figure 6.13 Observation of Torque in Drive Shaft

6.5 Experiment of Active Damping Control for EV Drivetrain

In this section experiment for LQG-QGA joint active damping control algorithm for EV drivetrain is carried out. However, because of the limitation of experimental equipment, the driving motor and MCU cannot meet requirements of accuracy and response time required by the optimal control law. Therefore, the proposed active damping control method is tested by the rapid control prototype. The control law is downloaded into the Micro AutoBox as the controller, and utilize the model in dSPACE Simulator to imitate real electric powertrain, throttle command is given by a host computer that communicates with the Micro AutoBox, measurement and saving of drivetrain states are realized by ControlDesk on a host computer of Simulator and MATLAB, communication between the devices is over CAN bus. The established rapid control prototype system is shown in Figure 6.14.
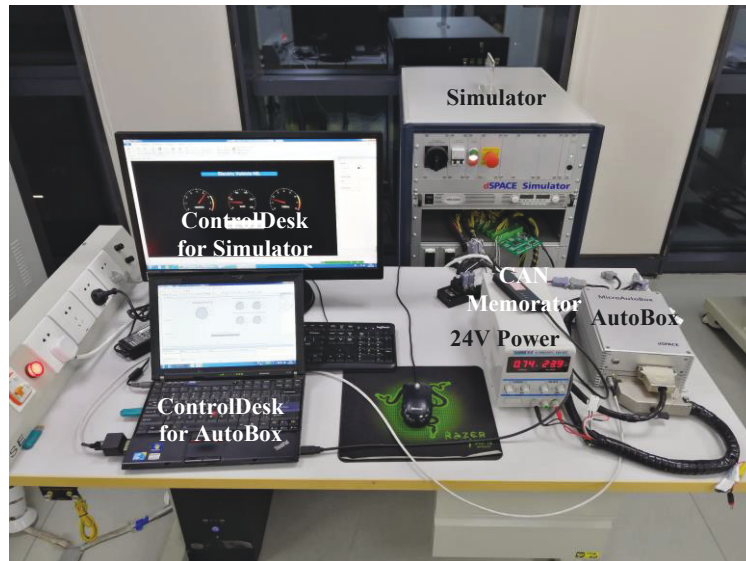

Figure 6.14 Experimental Equipment of Active Damping Control for EV Drivetrain

In the host computer for controlling the dSPACE Simulator, there is an EV powertrain dynamic model established by MATLAB, interfaces of vehicle speed command, motor speed, wheel speed are left for communications, of which parameters are set identical to Table 5.2 in 5.4. In the rapid control prototype experiment sample time is set to 10 ms, the established model is built into C code and sdf file is generated to be downloaded to

the dSPACE Simulator.

Similar operations are done to the host computer for controlling the Micro Autobox, the another generated sdf file is downloaded to the Micro AutoBox, and the control command is given from the host computer. When target speed is given from the ControlDesk, the EV drivetrain motion states will response as in Figure 6.15. It can be seen that the motor torque can response rapidly after the target speed command is given to make the wheel speed to increase or decrease. The control law with the optimized weight parameter is obtained from calculation with MATLAB with identical parameters to Chapter 5, the wheel speed under the optimal control law can vary smoothly with little torsional oscillations, it can track the target speed accurately.
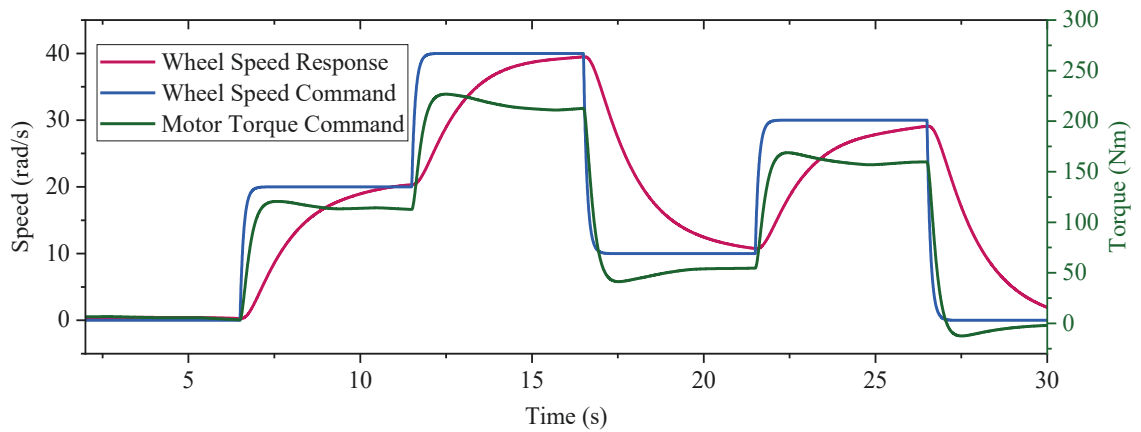

Figure 6.15 Experiment Results of RCP for Active Damping Control

6.6 Summary

In this chapter experiments are carried out for algorithms proposed in previous chapters, different experimental schemes are developed for different purpose based on existing experimental conditions. For the vehicle mass parameter estimation in Chapter 3, experiment of real electric bus is realized; for the AASTW-based drive shaft torque observation, experiment of real vehicle and test rig is realized; for the active damping control for EV drivetrain, experiment is carried out on rapid control prototype system.

CHAPTER 7: SUMMARY AND PROSPECT

Electric vehicles are playing an increasingly important role in daily life, and various of types developed after passenger vehicles and commercial vehicles are becoming more and more abundant. The technical approaches to improve the dynamic and economy performance of electric vehicles are researched internationally. This thesis is based on the collaborative project of Beijing Electric Vehicle Co., LTD and Beijing collaborative innovation center for electric vehicles and is supported financially by National Natural Science Foundation of China and National Key R&D Program of China, in this thesis active control algorithms of torsional oscillations are researched with intelligent parameter estimation and state observation.

7.1 Summary

Because the permanent magnet synchronous motor applied to electric vehicle responses quickly and there is no fly wheel for buffering and saving energy, and considering the PMSM torque step output torsional oscillations will come about in the EV drivetrain comprising elastic-damping parts at the moment of driver tipping in/out and detaching the synchronizer for shifting, it will further transform into longitudinal shuffle that more sensitive to human bodies. Taking advantage of the PMSM such as good controllability and response performance research focusing on active damping control for EV drivetrain is carried out with several algorithms proposed, which are listed specifically as follows:

(1) Based on the drivetrain structure of electric logistics vehicle, differential dynamic models are established for all rotational components and the whole drivetrain, from which several natural frequencies and corresponding modes of the drivetrain are analyzed. The multi-body dynamics equation is Fourier transformed to obtain the frequency response function of vehicle body to motor excitation, such that frequency response characteristics of vehicle body to motor excitation is analyzed, and further necessity and performance of equipping a torsional damper is discussed further.

(2) As one of the most important parameter in dynamic control for vehicle drivetrain, vehicle mass is not only impossible to be measured directly during running but also varies in large scale with passengers or load, therefore, intelligent parameter estimation for vehicle mass based on nonlinear filter is proposed. The estimator is based on Monte Carlo method and is a recursive Bayesian estimation essentially, through processes of importance sampling and resampling, etc. searching of the vehicle mass is realized from posterior probability distribution of a large number of particles according to the measured information of motor speed, vehicle speed and motor torque. The main advantage of the proposed method is being different from the common Kalman filters, it does not require to know the statistical characteristics of noise or uncertainties of the systems, so it is suitable for nonlinear vehicle systems working in complex and random conditions.

(3) In order to obtain the necessary states of EV drivetrain for the active controller, an accelerated adaptive super-twisting sliding mode observer is proposed for observation of drivetrain states that are difficult to be measured. By introducing high-order sliding mode, and adaptive gains and the "system damping" the inherent "chattering" issue, and the "system damping" can accelerate convergence of observation error obviously because the region of attraction is expanded and the trajectory of observation error goes in the attraction region earlier. The proposed novel sliding mode observer is applied to observation of torque in drive shaft to avoid excessive elastic potential energy accumulated in the drive shaft is released suddenly to bring vibration and impact, it also provides necessary state information for active damping control.

(4) With the multi-feedback from the drivetrain states joint optimal active damping control algorithm is proposed, to active compensate the torsional oscillations in drivetrain by regulating motor torque output when shifting and launching. The control law is obtained from the introduced QGA-LQG joint optimal algorithm of which weight parameter is optimized by quantum genetic algorithm off line rather than subjective selection. The quantum genetic algorithm applies quantum computing to replace the binary coding in genetic algorithm with the qubit containing polymorphic information, and he quantum revolving gate is introduced to realize updating and evolution of the

chromosomes, the optimization is significantly accelerated.

(5) Based on the proposed algorithms corresponding experimental scheme are designed. experiment of real electric bus is realized for the vehicle mass estimation; experiment of real vehicle and test rig is realized for the AASTW-based drive shaft torque observation; experiment is carried out on rapid control prototype system for the active damping control for EV drivetrain.

7.2 Prospect and Future Work

Although the research content of this thesis is self-contained logically, there is still a certain distance to the practical applications. Outlook of the future research work will focus on the following aspects:

(1) The structure of estimation → state observation → active damping control should be realized in actual communication, i.e. the necessary state information required by active damping controller is provided by the state observation unit timely, the required parameter information is provided by particle filter-based parameter estimation unit timely; and vehicle mass required by the state observation unit is output by the vehicle mass parameter estimation unit timely. Therefore, a network between parameter estimation unit, state observation unit and active control unit can be connected in real time.

(2) At this present, since the ordinary permanent magnet synchronous motor and ordinary MCU are still incompetent to realize torque control in sufficient high frequency and accuracy, usually there is still a little deviation between the actual motor torque output and the torque control command. Active damping control by regulating motor torque output is still on the way to practical application of real vehicles and it is still prevalent to improve drivability and shifting quality by decrease loading of motor torque output. But it is quite prospective with the improvement of motor manufacturing technique and MCU performance, the active damping control method will be subject to more realistic experiment and application definitely.

APPENDICES

Appendix A

The moment of inertia matrix $\boldsymbol{J}$, damping matrix $\boldsymbol{C}$, stiffness matrix $\boldsymbol{K}$, angular displacement vector $\boldsymbol{\theta}$, excitation vector $\boldsymbol{T}$ are expressed as follows:
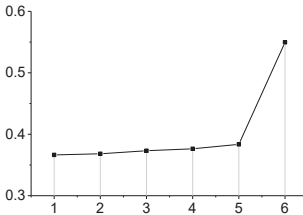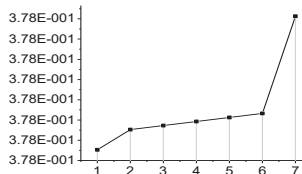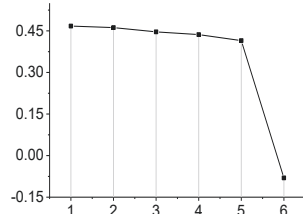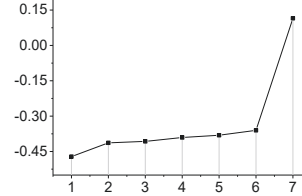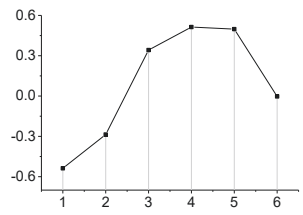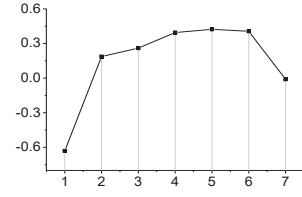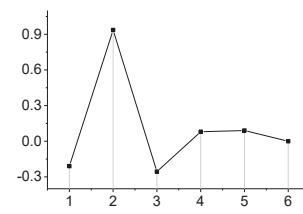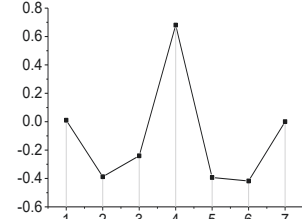
$$\boldsymbol{J} = \begin{bmatrix} J_1 & & & & & & \\ & J_2 & & & & & \\ & & J_3 & & & & \\ & & & J_4 & & & \\ & & & & J_5 & & \\ & & & & & J_6 & \\ & & & & & & J_7 \end{bmatrix}, \quad \boldsymbol{\theta} = \begin{bmatrix} \theta_1 \\ \theta_2 \\ \theta_3 \\ \theta_4 \\ \theta_5 \\ \theta_6 \\ \theta_7 \end{bmatrix}, \quad \boldsymbol{T} = \begin{bmatrix} T_m \\ 0 \\ 0 \\ 0 \\ 0 \\ 0 \\ 0 \end{bmatrix},$$
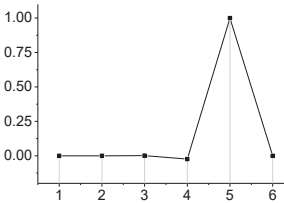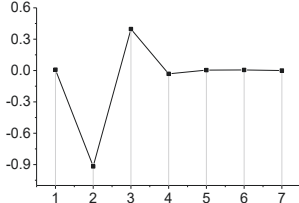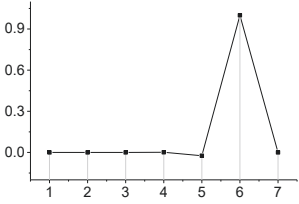
$$\boldsymbol{K} = \begin{bmatrix} K_1 & -K_1 & & & & & \\ -K_1 & K_1+K_2 & -K_2 & & & & \\ & -K_2 & K_2+K_3 & -K_3 & & & \\ & & -K_3 & K_3+K_4 & -K_4 & & \\ & & & -K_4 & K_4+K_5 & -K_5 & \\ & & & & -K_5 & K_5+K_6 & -K_6 \\ & & & & & -K_6 & K_6 \end{bmatrix},$$
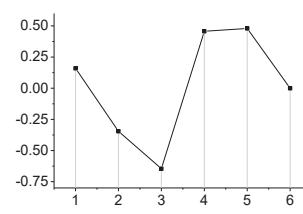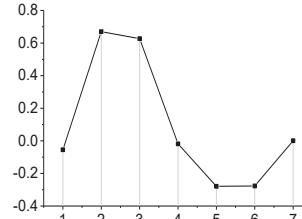
$$\boldsymbol{C} = \begin{bmatrix} C_1 & -C_1 & & & & & \\ -C_1 & C_1+C_2 & -C_2 & & & & \\ & -C_2 & C_2+C_3 & -C_3 & & & \\ & & -C_3 & C_3+C_4 & -C_4 & & \\ & & & -C_4 & C_4+C_5 & -C_5 & \\ & & & & -C_5 & C_5+C_6 & -C_6 \\ & & & & & -C_6 & C_6 \end{bmatrix}.$$

Appendix B

Table B1 Natural Frequencies and Vibration Mode of Electric Drivetrain

	Rigid Connection			Equip Torsional Damper	
Order	Natural Frequency (Hz)	Mode Shape	Order	Natural Frequency (Hz)	Mode Shape
1	4.15		1	1.13×10^{-6}	
2	6.49		2	6.47	
3	40.97		3	20.93	
4	106.56		4	66.92	
5	140.16		5	113.28	

6	364.89	
-	-	-

6	202.87	
7	364.89	

REFERENCES

[1] Sun Y., Li L., Yan B., et al. A Hybrid Algorithm Combining EKF and RLS in Synchronous Estimation of Road Grade and Vehicle′ Mass for a Hybrid Electric Bus. Mechanical Systems & Signal Processing, 2016, 68–69: 416-430.

[2] Vahidi A., Stefanopoulou A., Peng H. Recursive Least Squares with Forgetting for Online Estimation of Vehicle Mass and Road Grade: Theory and Experiments. Vehicle System Dynamics, 2005, 43(1): 31-55.

[3] Gao B., Chen H., Ma Y., et al. Design of Nonlinear Shaft Torque Observer for Trucks with Automated Manual Transmission. Mechatronics, 2011, 21(6): 1034-1042.

[4] Bain, Electric Vehicles for Smarter Cities: The Future of Energy nd Mobility. Geneva: World Economic Forum, 2018.

[5] Petroff A. These Countries Want to Ban Gas and Diesel Cars. America, Cable News Network, 2017-9-11 (Money).

[6] Lee A. China's Electric Car Market Is Growing Twice as Fast as the US. Here's why. Hong Kong: South China Morning Post, 2018-4-28.

[7] China Is Leading A Surge in Electric Vehicle Sales. World Economic Forum, 2018-5-22.

[8] Goldie-Scot L. Electric Vehicle Outlook 2018. Bloomberg, New Energy Finance, 2018.

[9] Chan C. C. The State of the Art of Electric, Hybrid, and Fuel Cell Vehicles. Proceedings of the IEEE, 2007, 95(4): 704-718.

[10] Wu G., Zhang X., Dong Z. Powertrain Architectures of Electrified Vehicles: Review, Classification and Comparison. Journal of the Franklin Institute, 2015, 352(2): 425-448.

[11] Hou R. Study on the Key Problems for the Electric Driving Automatic Mechanical Transmission System. Beijing: Beijing Institute of Technology, 2015.

[12] Ministry of Industrial Economic Research, Development Research Center of the State Council. Blue Paper on Automobile: A Report on the Development of China's Automobile Industry (2014). Beijing: Social Science Literature Publishing House, 2014.

[13] Bottiglione F., Pinto S., Mantriota G., et al. Energy Consumption of a Battery Electric

Vehicle with Infinitely Variable Transmission. Energies, 2014, 7(12): 8317-8337.

[14] He Z., Bai H. Automatic Mechanical Transmission Technique Development Actuality and Expectation. Transactions of The Chinese Society of Agricultural Machinery, 2007，38(5): 181-186.

[15] Hu J., Li K., Hu M., et al. Coordination Matching Control Method of AMT Gear Shifting for Pure Electric Car. China Journal of Highway and Transport, 2012, 25(1): 152-158.

[16] Yang Y. Study of Shift Strategy of 2 Speed Automatic Mechanical Transmission (2AMT) for Electric Vehicles. Shanghai: Shanghai Jiao Tong University, 2016.

[17] Zhang C., Wu X., Wang Z., et al. Control Strategy of Driving Motor During the AMT Shifting on Electric Vehicles. Journal of Beijing University of Technology, 2012(3): 325-329.

[18] Chen X. Study on Shifting Control Strategy for Two-Speed Automatic Mechanical Transmission of Pure Electric Vehicle. Chongqing: Chongqing University, 2013.

[19] Laitinen H., Lajunen A., Tammi K. Improving Electric Vehicle Energy Efficiency with Two-Speed Gearbox. IEEE Vehicle Power and Propulsion Conference. IEEE, 2017, 1-5.

[20] Huwood-Hudswell. Diesel Mines Locomotives. Colliery Engineering, 1948.

[21] Vulcan-Sinclair Fluidrive Makes Headway. The Commercial Motor Archive, 1946, August 16: 69.

[22] ROZSI D., Steeby J., Rocker K., et al. Control System for Low Speed Positioning and Pacing for on/off Highway Vehicles. World Intellectual Property Organization, WO2016183463A1, 2015-05-14.

[23] Glückler J., Maier A., Hunold B. Method for Controlling a Power Transmission. EU, EP2450599A3, 2010-11-09.

[24] Mo W., Walker P., Fang Y., et al. A Novel Shift Control Concept for Multi-speed Electric Vehicles. Mechanical Systems and Signal Processing, 2018, 112(2018): 171-193.

[25] Yu P., Zhang T., Guo R. The Current State and Trends of Automotive Drivetrain Torsional Vibration Active Control. Mechatronics, 2014(6): 3-10.

[26] Zheng J., Dai Y., Shi J. Electromagnetic Noise Characteristics of Permanent Magnet

Synchronous Motor Applied in Electric Vehicle. Transactions of China Electrotechnical Society, 2016, 31(a01): 53-59.

[27] Wang K. Research on Torsional Vibration of Driveline for Hybrid Electric Vehicle. Shanghai: Shanghai Jiao Tong University, 2013.

[28] Shiozaki H., Iwanaga Y., Ito H., et al. Interior Noise evaluation of Electric Vehicle: Noise Source Contribution Analysis. SAE Technical Paper, 2011, No. 2011-39-7229.

[29] Pettersson M. Driveline Modeling and Control[D]. Linkoping: Linkoping University, 1997.

[30] Han J. Active Disturbance Rejection Control Technique-the technique for Estimating and Compensating the Uncertainties. Beijing: National Defense Industry Press, 2008, 17-19.

[31] Ang K.H., Chong G.C.Y., Li,Y. PID Control System Analysis, Design, and Technology. IEEE Transactions on Control Systems Technology, 13(4): 559-576.

[32] Fu H., Tian G., Chen H., et al. A Study on the Torsional Vibration Control of Motor-Transmission Integrated Drive System. Automotive Engineering, 2010, 32(7): 596-600.

[33] Shi J. Study on the Optimization of Driving Control Strategy for Pure Electric Urban Bus. Beijing: Beijing Institute of Technology, 2016.

[34] Walker P., Fang Y., Zhang N. Dynamics and Control of Clutchless Automated Manual Transmissions for Electric Vehicles. ASME Journal of Vibration & Acoustics, 2017, 139(6): 061005-061005-13.

[35] Falcone F., Jim B., and Nelson D. Closed Loop Transaxle Synchronization Control Design. SAE Technical Paper, 2010, No. 2010-01-0817.

[36] Penta A., Gaidhani R., et al. Improvement in Shift Quality in a Multi Speed Gearbox of an Electric Vehicle through Synchronizer Location Optimization. SAE Technical Paper, 2017, No. 2017-01-1596.

[37] Lee H. D., Sul S. K., Cho H. S., et al. Advanced Gear-Shifting and Clutching Strategy for a Parallel-Hybrid Vehicle. Industry Applications Magazine IEEE, 2000, 6(6): 26-32.

[38] Yu C.H., Tseng C.Y. Research on Gear-Change Control Technology for the Clutchless Automatic–Manual Transmission of an Electric Vehicle. Proceedings of the Institution of Mechanical Engineers, Part D: Journal of Automobile Engineering, 2013,

227(10): 1446–1458.

[39] Kim S. J., Song C., Kim K. S., et al. Analysis of the Shifting Behavior of a Novel Clutchless Geared Smart Transmission. International Journal of Automotive Technology, 2014, 15(1): 125-134.

[40] He H., Liu Z., Zhu L., et al. Dynamic Coordinated Shifting Control of Automated Mechanical Transmissions Without a Clutch in a Plug-in Hybrid Electric Vehicle. Energies, 2012, 5 (8): 3094–3109.

[41] Reinholds M., Andreasson S. Dynamic Gear Shifting of an Automated Manual Transmission, Lund: Lund University, 2013.

[42] Tseng C. Y., Yu C. H. Advanced Shifting Control of Synchronizer Mechanisms for Clutchless Automatic Manual Transmission in an Electric Vehicle. Mechanism & Machine Theory, 2015, 84(2015): 37-56.

[43] Haj-Fraj A., Pfeiffer F. Optimal Control of Gear Shift Operations in Automatic Transmissions. Journal of the Franklin Institute, 2001, 338(2-3): 371-390.

[44] Lin S., Chang, S., Li, B. Improving the Gearshifts Events in Automated Manual Transmission by Using an Electromagnetic Actuator. Proceedings of the Institution of Mechanical Engineers, Part C: Journal of Mechanical Engineering Science, 2015, 229(9): 1548–1561.

[45] Zhong Y. Optimal Control, Tsinghua University Press, 2015, 104-130.

[46] Zhao X., Liu H., Chen H. Research on Synchromesh-Based AMT Shifting Process. ACTA Armamentarii, 2010, 31(5): 534-540.

[47] Lin S. Research on Gearshift Control for a Direct-drive Automated Mechanical Transmission. Nanjing: Nanjing University of Science and Technology, 2014.

[48] Xv G. Drive and Control of the Electric Vehicle. Beijing: Electronic Industry Press, 2010, 205-252.

[49] Chen H., Gao B. Nonlinear Estimation and Control of Automotive Drivetrains. Science Press, 2014, 1-30.

[50] Waschl H. Optimization and Optimal Control in Automotive Systems. Springer, 2014, 3-18.

[51] Ulsoy A.G. et al. Automotive Control Systems. CAMBRIDGE, 2012, 3-7.

[52] Powers W. F., Nicastri P. R. Automotive Vehicle Control Challenges in the 21st century. Control Engineering Practice, 2000, 8(6): 605-618.

[53] Re L. Automotive Model Predictive Control. London: Springer-Verlag, 2010, 1-30.

[54] Tao Y. New P ID control and its application, 2nd edition. Beijing: Mechanical Press, 2002, 1-26.

[55] Zeng Q. Zuo X., Chen F. Micro-Computer Control Technology. Chengdu: University of Electronic Science and Technology of China Press, 2013, 118-126.

[56] Qian X., Yan S. Electric Drive Control Technology. Beijing: Metallurgical Industry Press, 2013, 32-40.

[57] Mo J. System Modeling Analysis and Control. Shanghai: Shanghai Jiaotong University Press, 104-112.

[58] Bian L. Research and Implement on PID Controller Parameters Self-Tuning Methods. Dalian: Dalian University of Technology, 2009.

[59] Juang J., Huang M., Liu W. PID Control Using Presearched Genetic Algorithms for a MIMO System. IEEE Transactions on Systems, Man, and Cybernetics, Part C (Applications and Reviews), 2008, 38(5): 716-727.

[60] Li Y., Ang K.H., Chong G.C.Y. PID Control System Analysis and Design - Problems, Remedies, and Future Directions. IEEE Control Systems Magazine, 2006, 26 (1): 32-41.

[61] Schöner H.P. Automotive Mechatronics. Control Engineering Practice, 2004, 12(11): 1343-1351.

[62] Bertram T, Bekes F, Greul R, et al. Modelling and Simulation for Mechatronic Design in Automotive Systems. Control Engineering Practice, 2003, 11(2): 179-190.

[63] Isermann R. Mechatronic systems—Innovative Products with Embedded Control. Control Engineering Practice, 2005, 38(1): 175-191.

[64] Sun Z. Simulink Simulation and Code Generation Technology for Beginning to Proficiency, Beijing: Beihang University Press, 2015, 345-374.

[65] Schauffele J. Automotive Software Engineering: Principles, Processes, Methods, and Tools (in Chinese), Beijing: Publishing House of Electronics Industry, 2008, 107-223.

[66] Ding N. Method and Application of Parameter Estimation in Automotive Active Control System. Beijing: Beihang University Press, 2013,7-8.

[67] Wang X. System Modeling and Parameter Estimation. Harbin: Harbin Institute of Technology Press, 2003, 45-88.

[68] Wu X. System Modeling and Parameter Estimation, Theory and Algorithms. Beijing: Machinery Industry Press, 2002, 70-98.

[69] Ding F., Wang X., Chen Q., et al. Recursive Least Squares Parameter Estimation for a Class of Output Nonlinear Systems Based on the Model Decomposition. Circuits Systems & Signal Processing, 2016, 35(9): 1-16.

[70] Stefanopoulou A. Recursive Least Squares with Forgetting for Online Estimation of Vehicle Mass and Road Grade: Theory and Experiments. Vehicle System Dynamics, 2005, 43(1): 31-55.

[71] Lin N. , Zong C. , Shi S. The Method of Mass Estimation Considering System Error in Vehicle Longitudinal Dynamics. Energies, 2018, 12(1), 52.

[72] Eliseiiliescu C., Paleologu C., Tamaş R. On the Performance of Variable Forgetting Factor Recursive Least-Squares Algorithms. Advanced Topics in Optoelectronics, Microelectronics, and Nanotechnologies VIII. International Society for Optics and Photonics, 2016:1001023.

[73] Ding F., Wang Y., Ding J. Recursive Least Squares Parameter Identification Algorithms for Systems with Colored Noise Using the Filtering Technique and the Auxiliary Model [J]. Digital Signal Processing, 2015, 37(1): 100-108.

[74] Rappaport T. Wireless Communications Principles and Practice (in Chinese). Beijing: Publishing House of Electronics Industry, 1999, 239-240.

[75] Malik O. P. Some Issues on the Practical Use of Recursive Least Squares Identification in Self-Tuning Control. International Journal of Control, 1991, 53(5): 1021-1033.

[76] Yang J , Na J , Guo Y , et al. Adaptive estimation of road gradient and vehicle parameters for vehicular systems. IET Control Theory and Applications, 2015, 9(6):935-943.

[77] Bergman N. Recursive Bayesian Estimation. Linkoping: Linkoping Studies in Science and Technology, 1999, 579.

[78] Huang X., Wang Y. Kalman Filter Principle and Application: MATLAB Simulation.

Beijing: Publishing House of Electronics Industry, 2015, 1-5.

[79] Liang Y., Pan Q., Yang F., et al. The Modern Estimation Theory and Application of Complex System. Beijing: Science Press, 2009, 147-157.

[80] Gustafsson F., Hendeby G. Some Relations Between Extended and Unscented Kalman Filters. IEEE Transactions on Signal Processing, 2012, 60(2): 545-555.

[81] Yin S., Gao H., Qiu J., et al. Descriptor Reduced-Order Sliding Mode Observers Design for Switched Systems with Sensor and Actuator Faults. Automatica, 2017, 76: 282-292.

[82] Liu Z., Lu X., Gao D. A Ship Heading Control with Speed Keeping via a Nonlinear Disturbance Observer. Journal of Navigation, 2019, 72(4): 1035-1052.

[83] Biricik S., Komurcugil H. Optimized Sliding Mode Control to Maximize Existence Region for Single-Phase Dynamic Voltage Restorers. IEEE Transactions on Industrial Informatics, 2016, 12(4): 1486-1497.

[84] Liu Z. Ship Adaptive Course Keeping Control With Nonlinear Disturbance Observer. IEEE Access, 2017, 5: 17567-17575.

[85] Liu J., Vazquez S., Wu L., et al. Extended State Observer-Based Sliding-Mode Control for Three-Phase Power Converters. IEEE Transactions on Industrial Electronics, 2016, 64(1): 22-31.

[86] Qin Y., Zhao F., Wang Z., et al. Dong M. Comprehensive Analysis for Influence of Controllable Damper Time Delay on Semi-Active Suspension Control Strategies. Journal of Vibration and Acoustics, 2017, 139(3): 031006-031006-12.

[87] Qin, Y., Xiang, C., Wang, Z., et al. Road Excitation Classification for Semi-Active Suspension System Based on System Response. Journal of Vibration and Control, 2018, 24(13): 2732–2748.

[88] Xing Y., He W., Pecht M., et al. State of Charge Estimation of Lithium-ion Batteries Using the Open-circuit Voltage at Various Ambient Temperatures. Applied Energy, 2014, 113(1): 106-115.

[89] Si X. S., Wang W., Hu C. H., et al. Remaining Useful Life Estimation Based on a Nonlinear Diffusion Degradation Process. IEEE Transactions on Reliability, 2012, 61(1): 50-67.

[90] Liu J., Wu C., Wang Z., et al. Reliable Filter Design for Sensor Networks Using Type-2 Fuzzy Framework. IEEE Transactions on Industrial Informatics, 2017, 13(4): 1742-1752.

[91] Shtessel Y., Taleb M., Plestan F. A Novel Adaptive-Gain Supertwisting Sliding Mode Controller: Methodology and Application. Automatica, 2012, 48(5): 759-769.

[92] Mu C., Tang Y., He H. Improved Sliding Mode Design for Load Frequency Control of Power System Integrated an Adaptive Learning Strategy. IEEE Transactions on Industrial Electronics, 2017, 64(8): 6742-6751.

[93] Levant A. Homogeneity Approach to High-Order Sliding Mode Design. Automatica, 2005, 41(5): 823-830.

[94] Apazaperez W. A., Fridman L., Moreno J. A. Higher-order sliding-mode observers with scaled dissipative stabilizers. International Journal of Control, 2016: 1-16.

[95] Pilloni A., Pisano A., Usai E. Observer-Based Air Excess Ratio Control of a PEM Fuel Cell System via High-Order Sliding Mode. IEEE Transactions on Industrial Electronics, 2015, 62(8): 5236-5246.

[96] Xu L., Hu J., Cheng S., et al. Nonlinear Observation of Internal States of Fuel Cell Cathode Utilizing a High-Order Sliding-Mode Algorithm. Journal of Power Sources, 2017, 356: 56-71.

[97] Rath J. J., Veluvolu K. C., Defoort M., et al. Higher-Order Sliding Mode Observer for Estimation of Tyre Friction in Ground Vehicles. IET Control Theory & Applications, 2014, 8(6): 399-408.

[98] Li P. Research and Application of Traditional and Higher-Order Sliding Mode Control. Changsha: National University of Defense Technology, 2011.

[99] Moreno J. A., Osorio M. A Lyapunov Approach to Second-Order Sliding Mode Controllers and Observers. 47th IEEE Conference on Decision and Control, 2008: 2856-2861.

[100] Guzmán E., Moreno J. A. Super-Twisting Observer for Second-Order Systems with Time-Varying Coefficient. IET Control Theory & Applications, 2015, 9(4): 553-562.

[101] Levant A. Sliding Order and Sliding Accuracy in Sliding Mode Control. International Journal of Control, 1993, 58(6): 1247-1263.

[102] Dvir Y., Levant A. Accelerated Twisting Algorithm. IEEE Transactions on Automatic Control, 2015, 60(10): 2803-2807.

[103] Karthikeyan A., Rajagopal K. Chaos Control in Fractional Order Smart Grid with Adaptive Sliding Mode Control and Genetically Optimized PID Control and Its FPGA Implementation. Complexity, 2017, 3815146.

[104] Laghrouche S., Liu J., Ahmed F. S., et al. Adaptive Second-Order Sliding Mode Observer-Based Fault Reconstruction for PEM Fuel Cell Air-Feed System[J]. IEEE Transactions on Control Systems Technology, 2015, 23(3): 1098-1109.

[105] Gonzalez T., Moreno .J A., Fridman L. Variable Gain Super-Twisting Sliding Mode Control. IEEE Transactions on Automatic Control, 2012, 57(8): 2100-2105.

[106] Baratieri C. L., Pinheiro H. New Variable Gain Super-Twisting Sliding Mode Observer for Sensorless Vector Control of Nonsinusoidal Back-EMF PMSM. Control Engineering Practice, 2016, 52: 59-69.

[107] Gutman A. S. Active Damping Concept for Gravity Gradient Satellite Attitude Control. Journal of Spacecraft and Rockets, 1967, 4(7): 953-955.

[108] Clarence W.De Silva. Vibration Damping, Control, and Design (in Chinese). Beijing: Machinery Industry Press, 2013, 40.

[109] Berriri M., Chevrel P., Lefebvre D., et al. Active Damping of Automotive Powertrain Oscillations by a Partial Torque Compensator. Control Engineering Practice, 2008, 16(7): 874-883.

[110] Lu X. Moving Horizon Optimal Control for Automotive Driveline Systems. Changchun: Jilin University, 2013.

[111] Kiencke U., Nielsen L. Automotive Control Systems for Engine, Driveline, and Vehicle 2nd edition (in Chinese). Beijing: Higher Education Press, 2010, 160-247.

[112] Fredriksson J., Weiefors H., Egardt B. Powertrain Control for Active Damping of Driveline Oscillations. Vehicle System Dynamics, 2002, 37(5): 359-376.

[113] Xv G. Theoretical Basis of Long-Term Satellite Formation Flight. Shenyang: Liaoning Science and Technology Publishing House, 2015, 144-145.

[114] Richalet J., Rault A., Testud J. L., et al. Model Predictive Heuristic Control: Applications to Industrial Processes. Automatica, 1978, 14(5): 413-428.

[115] Li H., Hou T. Computer Control System. Beijing: Machinery Industry Press, 2016, 134-135.

[116] Su C., Huang Y., Li S. Process Control System. Beijing: Tsinghua University Press, 2014, 119-120.

[117] Xi Y., Li D., Lin S. Model Predictive Control – Status and Challenges. ACTA Automatica Sinica, 2013, 39(3): 222-236.

[118] Hu S. Theory and System of Optimal Control. Beijing: Science Press, 2005, 1.

[119] Fang Y. Optimal Control Theory and Applications for Stochastics Systems. Beijing: Tsinghua University Press, 2017, 137-138.

[120] Zhang S., Gao L. Modern Control Theory. Beijing: Tsinghua University Press, 2006, 292.

[121] Zhang J. Tank Armored Vehicle Adaptive Suspension System. Beijing: National Defense Industry Press, 2014, 139.

[122] Roy T., Chakraborty D. Optimal Vibration Control of Smart Fiber Reinforced Composite Shell Structures Using Improved Genetic Algorithm. Journal of Sound & Vibration, 2009, 319(1): 15-40.

[123] Zhang Y., Chen Z., Jiao Y. A Hybrid Vibration Isolator: Design, Control, and Experiments[J]. Proceedings of the Institution of Mechanical Engineers, Part C: Journal of Mechanical Engineering Science, 2016, 230(17): 2982–2995.

[124] Prabakar R. S., Sujatha C., Narayanan S. Response of A Half-Car Model with Optimal Magnetorheological Damper Parameters. Journal of Vibration and Control, 2016, 22(3): 784–798.

[125] Nagarkar M.; Vikhe G.. Optimization of the Linear Quadratic Regulator (LQR) Control Quarter Car Suspension System Using Genetic Algorithm. Ingeniería e Investigación 2016, 36(1): 23-30.

[126] Das S., Pan I., Das S. Multi-objective LQR with Optimum Weight Selection to Design FOPID Controllers for Delayed Fractional Order Processes. Isa Transactions, 2015, 58: 35-49.

[127] Ufnalski B., Kaszewski A., Grzesiak L. M. Particle Swarm Optimization of the Multioscillatory LQR for a Three-Phase Four-Wire Voltage-Source Inverter With an,

Output Filter. IEEE Transactions on Industrial Electronics, 2015, 62(1): 484-493.

[128] Lin C., Sun S., Walker P., et al. Off-Line Optimization Based Active Control of Torsional Oscillation for Electric Vehicle Drivetrain. Applied Sciences, 2017, 7(12): 1261.

[129] Dong A. Study of Complete Torque Shifting Control for Clutchless AMT of Electric Vehicles. Beijing: Beijing Institute of Technology, 2016.

[130] Yu F., Lin Y. Automobile System Dynamics. Beijing: Machinery Industry Press, 2005, 17-19.

[131] Ni Z. Vibration Mechanics. Xi'an: Xi'an Jiaotong University Press, 1989, 52-61.

[132] Eriksson L., Nielsen L. Modeling and Control of Engines and Drivelines. John Wiley & Sons, 2014, 381-412.

[133] Pettersson M. Driveline Modeling and Control. Sweden Linkoping: Linkoping University, 1997.

[134] Guignard J. C. Human sensitivity to vibration. Journal of Sound and Vibration, 1971, 15(1): 11-16.

[135] Carpenter J., Clifford P., and Fearnhead P. Improved Particle Filter for Nonlinear Problems, IEE Proceedings-Radar, Sonar and Navigation, 1999, 146, (1): pp 2-7.

[136] Arulampalam M.S., Maskell S., Gordon N., et al. A Tutorial on Particle Filters for Online Nonlinear/Non-Gaussian Bayesian Tracking, IEEE Transactions on Signal Processing, 2002, 50, (2): 174-188.

[137] Gustafsson F. Particle Filter Theory and Practice with Positioning Applications, IEEE Aerospace and Electronic Systems Magazine, 2010, 25, (7): 53-82.

[138] Marcelo G. S. Bruno. Sequential Monte Carlo Methods for Nonlinear Discrete-Time Filtering. Synthesis Lectures on Signal Processing, 2013, 99.

[139] Mao Z., Jiang B., Shi P. Fault-Tolerant Control for a Class of Nonlinear Sampled-Data Systems Via a Euler Approximate Observer. Automatica, 2010, 46, (11): 1852-1859.

[140] Nesic D. and Teel A.R. Stabilization of Sampled-Data Nonlinear Systems Via Backstepping on Their Euler Approximate Model. Automatica, 2006, 42(10): 1801-1808.

[141] Liu J. Sliding Mode Control Using MATLAB (in Chinese). Beijing: Tsinghua University Press, 2012, 1-3.

[142] Davila J., Fridman L. and Levant A. Second-order sliding-mode observer for

mechanical systems. IEEE Transactions on Automatic Control, 2005, 50(11): 1785-1789.

[143] Pettersson M., Nielsen L. Gear Shifting by Engine Control. IEEE Transactions on Control Systems Technology, 2000, 8(3): 495-507.

[144] Mousavi M.S.R., Alizadeh H.V. Boulet, B. Estimation of Synchromesh Frictional Torque and Output Torque in a Clutchless Automated Manual Transmission of a Parallel Hybrid Electric Vehicle. IEEE Transactions on Vehicular Technology, 2017, 66(7): 5531-5539.

[145] Zhu X., Meng F., Zhang H., Cui, Y. Robust Driveshaft Torque Observer Design for Stepped Ratio Transmission in Electric Vehicles. Neurocomputing, 2015, 164: 262-271.

[146] Tang X., Hu X., Yang W., et al. Novel Torsional Vibration Modeling and Assessment of a Power-Split Hybrid Electric Vehicle Equipped with a Dual-Mass Flywheel. IEEE Transactions on Vehicular Technology, 2018, 67(3): 1990-2000.

[147] Huang D. Data Warehouse and Data Mining Tutorial. Tsinghua University Press, 2016, 388-403.

[148] Qiao F., Patnaik S., Wang J. Recent Developments in Mechatronics and Intelligent Robotics: Proceedings of the International Conference on Mechatronics and Intelligent Robotics (ICMIR2017)-Volume 1. Springer, 2017, 563-564.

[149] Zhu X. Robust Control and State Estimation of E-drive System for Pure Electric Vehicles. Xi'an: Northwestern Polytechnical University, 2015.

[150] Kiencke U.; Nielsen L. Automotive control systems: For engine, driveline, and vehicle. Springer: 2005, 249-251.